Development of a Small-Animal SPECT System with a High-Purity Germanium Detector

By

Lindsay Craig Johnson

Dissertation

Submitted to the Faculty of the

Graduate School of Vanderbilt University

in partial fulfillment of the requirements

for the degree of

DOCTOR OF PHILOSOPHY

in

Biomedical Engineering

December, 2013

Nashville, Tennessee

Approved:

Professor Todd E. Peterson

Professor Mark D. Does

Professor John C. Gore

Professor William A. Grissom

Professor Thomas E. Yankeelov

ACKNOWLEDGEMENTS

There are countless people without whom I wouldn't have been able to pull this off. From my advisors, colleagues, and classmates to my family and closest friends, they all contributed in some meaningful way over the past six years.

Specifically, I would like to thank my advisor, Dr. Todd Peterson, for all of his guidance and encouragement throughout my time at Vanderbilt, and for our meetings week after week where I would leave with an even longer to-do list than when I started. My appreciation also goes out to the rest of my committee members, including Dr. Does, Dr. Gore, Dr. Grissom, and Dr. Yankeelov, for their support and insight throughout my graduate student career.

It's difficult to imagine this process without the members of my lab group: Desmond Campbell, Oleg Ovchinnikov, Dr. Sepi Shokouhi, Dr. Noor Tantawy, and George Wilson, who were always there for all of the triumphs and failures and who were so generous with their time, suggestions, software development, troubleshooting, manual labor and of course, their collegiality.

I'm very grateful for all of those at VUIIS who helped provide the resources necessary for me to focus on my degree, in particular, Nancy Hagans who makes sure that VUIIS can actually operate smoothly, and to all of those who helped to take apart or reassemble the MicroCAT II.

I wouldn't have been able to complete this project if it weren't for everyone at PHDs Co. who manufactured the HPGe detector, and who took the time to help me understand how the HPGe detector signal processing worked and always helped troubleshoot when issues arose.

Most importantly, I would like to thank my friends and family for their love, kindness, sarcasm and support: My mom who shared in my excitement on the good days, and gave encouragement on the rough days even if she didn't have the slightest idea what I was talking about; My dad, who always encouraged me to hurry up and finish already; My brothers – Eric, Scott, and Drew – for keeping me grounded; My grandparents, for instilling in me the importance of education, especially my grandfather, R.T. Robinson; Tom for being by my side the last four years and giving me unwavering love and support through the crazy road that is grad school; and lastly, Erich Bolton, Rachel Peters, and

Joanna Mazurska, my close friends that have given their encouragement, and provided much-needed sanity-breaks over the years.

Finally, I would like to acknowledge the various funding sources that have supported me and this project over the years, including: NIH 5T32CA009592, NIH/National Cancer Institute R25CA136440, US Department of Energy Office of Science (BER) DE-SC0002437, and NIH/NIBIB R01EB013677.

TABLE OF CONTENTS

LIST OF TABLES

Table Page

LIST OF FIGURES

Figure Page

LIST OF ABBREVIATIONS AND NOMENCLATURE

Abbreviation	Full Name
1. CFOV	Central Field of View
2. CT	Computed Tomography
3. DOI	Depth of Interaction
4. DSSD	Double Sided Strip Detector
5. FOV	Field of View
6. FWHM	Full Width at Half Maximum
7. FWTM	Full Width at Tenth Maximum
8. HPGe	High-Purity Germanium
9. MLEM	Maximum Likelihood Expectation Maximization
10. MRI	Magnetic Resonance Imaging
11. MRS	Magnetic Resonance Spectroscopy
12. NEMA	National Electrical Manufacturers Association
13. NMSE	Normalized Mean Square Error
14. NSD	Normalized Standard Deviation
15. OSEM	Ordered Subset Expectation Maximization
16. PET	Photon Emission Tomography
17. PMTs	Photo-multiplier Tubes
18. PSF	Point Spread Function
19. p4HM	Four-pinhole, high-multiplexing collimator
20. p4LM	Four-pinhole, low-multiplexing collimator
21. p7	Seven-pinhole, high-multiplexing collimator
22. ROR	Radius of Rotation
23. SNR	Signal to Noise Ratio

24. SPECT	Single Photon Emission Computed Tomography
25. UFOV	Useful Field of View

CHAPTER I

INTRODUCTION

The Society of Nuclear Medicine and the Molecular Imaging Center of Excellence define molecular imaging as "the visualization, characterization and measurement of biological processes at the molecular and cellular levels in humans and other systems" which "typically includes two- or three-dimensional imaging as well as quantification over time" (Mankoff 2007). A variety of techniques are commonly used to obtain molecular images of small animals including nuclear imaging (positron emission tomography (PET) or single-photon emission tomography (SPECT)), magnetic resonance imaging (MRI), magnetic resonance spectroscopy (MRS), optical imaging (fluorescence or bioluminescence), ultrasound, and in some cases computed tomography (CT). An overview of some of these imaging modalities, including their mechanisms, is discussed in (Levin 2005), which also includes a comparison of relevant system properties.

MRS and MRI have excellent spatial resolution in both clinical and small-animal applications but have low sensitivity to contrast agents. Bioluminescence and fluorescence allow for reasonable sensitivity but have depth-dependent resolution due to the scattering of photons as they exit the subject and therefore the tissue depth of the contrast agent being imaged is limited to approximately 1 to 2 cm. PET and SPECT have the benefit of good spatial resolution (0.5 to 5 mm) and high molecular sensitivity (10^{-10} – 10^{-12} mol/l). In small-animal systems, SPECT generally has better spatial resolution while PET has a higher sensitivity, but both require the use of a radioactive contrast agent which can be expensive and also exposes the subject to radiation (Levin 2005). SPECT is chosen over PET for applications where a longer uptake period is required, as SPECT radiotracers can have half-lives that last days, and therefore allow the radiotracer to clear from non-target organs and tissue before imaging which reduces background noise. SPECT is also used when new tracers are being developed as longer-lived isotopes give chemists more time to synthesize the new radiotracers. In addition, SPECT allows imaging of multiple molecular pathways simultaneously when radiotracers that emit at different energies are used through multi-isotope imaging (Meikle, Kench et al. 2005; Franc, Acton et al. 2008).

Properties such as spatial resolution, temporal resolution, molecular sensitivity, penetration depth in tissue, and associated cost help to determine which modality is most appropriate for a specific task. These properties are in turn determined by the chosen imaging modality's strengths and weaknesses, and can vary depending on the configuration of the specific system. Improving any of these system properties is challenging and requires investigation of the system components, acquisition methods, contrast agents used, and/or reconstruction methods. In order to achieve better spatial resolution, temporal resolution, lower radiation dose, or shorter scan times, it is necessary to consider using alternate system designs or components. Although there are a wide variety of imaging techniques and processes which could use refinement at both the clinical and small-animal scales, this dissertation focuses on improvement to small-animal SPECT systems by replacing the industry-standard sodium-iodide (NaI(Tl)) scintillator detector, also known as an Anger camera, with a high-purity germanium (HPGe) double-sided strip semiconductor detector.

I.1 Specific Aims

This project utilizes a specially-designed HPGe double-sided strip detector (DSSD) that was characterized and integrated into a small-animal imaging system. HPGe detectors are known for their excellent energy resolution and are capable of good spatial resolution when DSSDs or pixelated detectors are used. One group is currently using this type of detector for biomedical applications but they are focusing on PET and Compton imaging (Cooper, Boston et al. 2009; Harkness, Boston et al. 2009). To the author's knowledge, no other groups are currently investigating HPGe for small-animal SPECT applications. The system used in the project is mechanically-cooled to approximately 60 K and is 90 mm in diameter and 10 mm thick with two sets of 16 orthogonal strips that have a width of 4.75 mm with a 5 mm pitch. The system software includes algorithms that estimate photon interaction positions and give a pixel size of 0.53 x 0.53 mm in-plane with 1 mm depth bins. This dissertation will describe initial system characterization, its development into a small-animal SPECT-CT system, and show results of simulations that investigated potential improvements to system configuration.

I.1.1 AIM 1: Characterize the Imaging Capabilities of the HPGe Detector

The first aim of this project was to characterize the properties of this detector system that are relevant to small-animal imaging. Properties measured included: energy resolution, detection efficiency at relevant energies, intrinsic spatial resolution, scatter rejection, detector uniformity, and depth of interaction (DOI) estimation capabilities. These results are then compared to other detectors used in small-animal systems. A discussion of detector properties that could be improved upon and potential methods of implementation are presented.

I.1.2 AIM 2: Develop an HPGe-SPECT/CT System

The second aim of this project was to create an HPGe-SPECT/CT imaging system. A single-pinhole collimator was designed and manufactured that can be secured to the detector face. After the initial system characterization in Aim 1 was completed, the detector was mounted onto a MicroCAT II (Siemens Preclinical Solution, Knoxville, TN) gantry to allow for sequential SPECT-CT acquisitions. A method for system calibration was implemented and an analytically-determined system matrix was used with an MLEM reconstruction algorithm for image generation. To increase flexibility, helical SPECT scanning was implemented to allow for an extended axial field of view (FOV) and for better image quality. Quality assurance phantom studies were performed with the HPGe-SPECT/CT to characterize imaging performance. A multi-isotope phantom scan was acquired on both the HPGe-SPECT/CT system and a NanoSPECT-CT (Bioscan Inc.) which has a standard NaI(Tl) detector. Projections and reconstructed images were compared to demonstrate the difference in image quality between the two detectors. Phantom results compare quantitative image quality metric to results of other small-animal system and discuss current challenges and potential for future improvement.

I.1.3 AIM 3: Simulate Multi-Pinhole Si-HPGe SPECT and Investigate Multiplexing Effects

The sensitivity of Aim 2's HPGe-SPECT system is limited compared to most commercial small-animal SPECT systems due to only utilizing a single-pinhole aperture and a single camera head. Using multiple pinholes increases system sensitivity but when detector space is limited, such as with the HPGe detector used in Aim 1 and 2, overlapping

pinhole projections, known as multiplexing, is common. Too much multiplexing in projections leads to artifacts in reconstructed images. A stacked, dual-detector system may help to mitigate these effects.

A system was simulated that includes a multi-pinhole collimator with a Si detector (Shokouhi, McDonald et al. 2009) that has minimal multiplexing and an HPGe detector placed behind it with a large amount of multiplexing. This allows for better utilization of the HPGe detector area while utilizing non-multiplexed data from the Si detector in the reconstruction. The goal of this aim was to determine the usefulness of the additional Si projection data, and to determine a potential design for building the system in the future. First, four reconstruction algorithms that differed in how they combine the two projection sets were evaluated. Next, varying Si detector binning and pinhole sizes were simulated to evaluate the sensitivity versus noise tradeoff in order to determine the configuration of the Si system components. Finally, three pinhole configurations that resulted in differing amounts of multiplexing were compared in reconstructions with and without the minimally-multiplexed Si projections for four different object types to evaluate the influence of the additional Si data.

I.2 Dissertation Overview

This dissertation begins with an introduction to small-animal SPECT imaging, including an explanation of the process of SPECT image generation, and an overview of radiotracers, collimation, and image reconstruction methods. To give perspective to the novel HPGe detector used, a description of commonly-used detectors, including scintillators and semiconductors, is described in Chapter II. The following chapters expand upon the aforementioned specific aims of the project. Chapter III describes the methods and results of the characterization of the HPGe detectors. Chapter IV describes the detector being mounted onto a CT gantry, the development of software to acquire the raw image data, the software to process the data and perform image reconstruction, and shows example phantom images. In Chapter V, simulations of a novel stacked-detector design that increases sensitivity while minimizing the effects of multiplexing are described and results are presented. Finally, Chapter VI presents the overall conclusions of the work and suggests future areas of investigation.

CHAPTER II

BACKGROUND

To give perspective to the potential impact of this project, this chapter will first discuss SPECT's common applications and desired system properties. An overview of SPECT imaging and its applications is introduced. The process of image generation is presented, which details available radiotracers, collimator types, and an explanation of commonly used reconstruction methods. Subsequently, a discussion of standard scintillator detectors and an overview of newer semiconductor detector types are given. The progress of HPGe as a detector is discussed, along with current applications and signal processing techniques. The potential benefits of HPGe detectors used with SPECT are then explained.

II.1 SPECT Imaging Overview

SPECT is an imaging modality commonly used for both clinical and small-animal research applications. The fundamental basis of nuclear imaging is described by the tracer principle, first introduced in (Chiewitz and Hevesy 1935), and involves choosing a radioactive biological substrate that will, through its temporal and spatial distribution in the subject, reflect a particular body function or metabolism. Only trace amounts are administered to the subject in order to study the distribution without altering the investigated system itself (Deconinck 2003). A wide variety of methods have been developed to detect, and subsequently localize, where within a subject the radiotracer has accumulated. In SPECT, 3D images are acquired by pairing a collimator with a detector, or having multiple collimator-detector pairs, that either surround or rotate around the subject. The collimator allows for the origin of the photon to be estimated by stopping photons that do not originate from specific locations and angles within the subject. After photons pass through the collimator, signals are collected using a detector to estimate 2D projection images. These projection images are typically reconstructed with iterative algorithms, such as Maximum Likelihood-Expectation Maximization (MLEM) (Bruyant 2002), to create the image, or estimate of the 3D activity distribution. A variety of collimators are used depending on the application, desired image resolution, and needed signal to noise ratio (SNR), some of which include: parallel hole

(Weinmann, Hruska et al. 2009), slant hole (either converging or diverging) (Gullberg, Zeng et al. 1992), slit-slat (Walrand, Jamar et al. 2005), coded aperture (Meikle, Fulton et al. 2001), single-pinhole (Jaszczak, Li et al. 1994; Weber, Ivanovic et al. 1994), and multiple pinhole (Schramm, Ebel et al. 2003). Currently, parallel-hole collimators are common in clinical imaging due to their large FOV capabilities, while single and multi-pinhole apertures are more common in small-animal systems as they allow for higher resolution despite their lower sensitivity.

Some common clinical applications of SPECT are: imaging myocardial perfusion, neuroimaging including seizure localization and imaging dementia, bone metabolism, imaging of white blood cells to evaluate infection and inflammation, and a variety of oncology studies including detecting metastasis and monitoring changes in tumor size during treatment (Bybel, Brunken et al. 2008). Similar applications are commonly used in small-animal studies, including drug discovery or drug evaluation, as well as basic science investigations about a wide variety of disease states. These small-animal applications require, to different degrees, good spatial resolution, high sensitivity, good reproducibility, and quantifiable images. These qualities are influenced by all aspects of the imaging system, from the detector and collimator configuration to the reconstruction algorithm. To better understand these influences, an in-depth description of image generation is described in the following section.

II.2 SPECT Image Generation

II.2.1 SPECT Radiotracers

The first required component to SPECT image generation is the radionuclide. SPECT radionuclides typically have half-lives between 6 hours and several days, although some used in small-animal applications have half-lives of 2 months (^{125}I). A half-life should be long enough to allow for labeling chemistry and transportation to the subject yet not too long such that radiation dose to the subject and potential contamination issues from tracer disposal are minimized. The energy of the gamma ray released should be high enough not to scatter or strongly attenuate within the subject but low enough to have a large portion of photons interact within the detector being used. The energy should also be low enough to be stopped by a collimator of reasonable thickness. ^{99m}Tc is one of the more commonly used SPECT

radionuclides and emits photons with an energy of 140 keV and has a 6 hour half-life. ^{125}I has a lower emission energy (27-32 keV), which is predominantly absorbed by the photoelectric effect in the subject, and has a longer half-life of 59 days which can be used for some specifically-designed SPECT systems. ^{123}I is more commonly used as it has an emission energy of 159 keV in addition to 27-35 keV, with a more useful half-life of 13 hours. ^{111}In has a half-life of 2.8 days and energy peaks at 171 and 245 keV. The 245 keV peak of ^{111}In is the upper limit of energy typically used in SPECT imaging as bulkier collimators would be required to stop the higher-energy photons. In addition to half-life and emission energy, it is important that the isotope's chemical properties allow for it to be easily linked to a molecule of interest to make the desired radiotracer.

The radiotracer must be able to reach its biological target, which may require a small size or the ability to cross the blood-brain-barrier depending on the application. It needs to remain stable and not degrade after injection, and have suitable pharmacokinetics, which would allow the radiotracer to uptake in the desired tissue in a reasonable amount of time compared to both the radionuclide's half-life and the washout from non-targeted regions. Finally, the radiotracer must also be specific and limit its interaction to the process of interest. There is a wide variety of radionuclides that are used to make a variety of radiotracers, and some common options are listed in Table 1.

Table 1: SPECT applications

Radionuclide	Radiotracer	Targets	Source
^{99m}Tc	MDP	Bone metabolism	(Cowey, Szafran et al. 2007)
	HMPAO	blood perfusion in brain	(Alptekin, Degirmenci et al. 2001)
	Mag3	Kidney function	(Tantawy, Jiang et al. 2012)
	Sestamibi	myocardial perfusion, breast cancer	(Hachamovitch, Berman et al. 1998) (Taillefer 1999)
	Pertechnetate	Cardiac imaging: labeled red blood cells Thyroid imaging	(Ficaro, Fessler et al. 1996) (McBiles, Lambert et al. 1995)
^{123}I	Iomazenil	cerebral blood flow	(Lamusuo, Ruottinen et al. 1997)
	FP-CIT	Dopamine transporter imaging	(Lavalaye, Linszen et al. 2001)
	MIBG	Myocardial imaging	(Dobrucki and Sinusas 2010)
^{111}In	DTPA	Tumor or extra-vascular imaging	(Collins, Hogenkamp et al. 1999)

II.2.2 SPECT Collimation

After the radiotracer of interest has been injected into the subject and the appropriate uptake time has passed, subjects are placed into the SPECT system. The SPECT system design can vary significantly depending on the imaging task, but typically involves either pinhole or parallel hole collimators that help to determine the origin of the photon decay within the subject being imaged. Given the scope of this dissertation, this background will focus on single and multi-pinhole collimators as they are most commonly applied to small-animal imaging.

II.2.2.1 Single Pinhole Collimators

For small-animal applications where a smaller FOV and higher resolution is required, pinhole collimation is typically used. Either single or multi-pinhole collimators can be used, each having their benefits and limitations. Pinhole collimators suffer from a tradeoff between spatial resolution and sensitivity. The geometric resolution (R_g), total system resolution (R_{TOT}) and sensitivity (η) of a knife-edge single-pinhole collimator are:

$$R_g = d\left(1 + \frac{1}{M}\right)$$

Equation 1

$$R_{TOT} = \sqrt{{R_g}^2 + \left(\frac{R_d}{M}\right)^2}$$

Equation 2

$$\eta = \frac{d^2}{16a^2} cos^3\,\theta$$

Equation 3

R_g is dependent on the pinhole diameter (*d*), and the system magnification (*M*), which is determined by the ratio of the focal length to the radius of rotation (ROR), while the total resolution is a function of R_g in addition to the detector's intrinsic resolution R_d. Figure 1 shows a typical system configuration labeling some of these variables. The sensitivity is also dependent on the pinhole diameter (*d*), in addition to θ, which is the angle between the collimator and

the origin of the photon and *a* as the distance from object to pinhole. The larger the angle θ, the further that position is from the pinhole's center of the FOV, and because of the cubic fall-off, the sensitivity to photons off-axis decreases rapidly in single-pinhole systems. The tradeoff between resolution and sensitivity is dependent on the pinhole diameter; an increase in the pinhole diameter linearly increases the sensitivity, but decreases the resolution by a factor of the effective pinhole diameter squared.

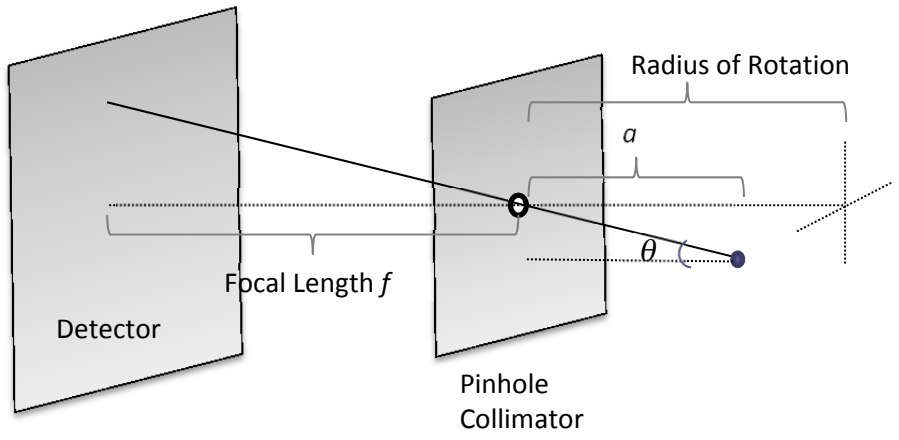

Figure 1: Schematic of typical pinhole-detector configuration showing the incident angle of photon origin (θ) and its distance from the collimator *a*, the system's focal length *f*, and radius of rotation.

The pinhole diameter (*d)* in this case is for an ideal pinhole, where no penetration or scatter occurs in the collimator and all photons are stopped by the collimator material unless they pass through the pinhole itself. In reality, photons can pass through the collimator material and still reach the detector. The probability of this occurring depends on the density of the collimator material and the radionuclide emission energy being detected. Using higher-energy radionuclides and/or a lower density collimator material causes an increase in collimator penetration, which affects both the sensitivity and the resolution of the system. To account for these changes, equations that determine the effective pinhole, for either sensitivity or resolution, have been derived by (Metzler, Bowsher et al. 2002; Accorsi and Metzler 2004), and are discussed and utilized in section IV.2.

II.2.2.2 Multi-Pinhole Collimators

One way to help overcome the sensitivity-resolution tradeoff is to design a collimator with multiple pinholes. The overall sensitivity increases by a factor of the number of pinholes (assuming the same pinhole configuration and no

projection overlap) while keeping the system resolution the same as the single-pinhole configuration. If the locations of the additional pinholes are spaced along the axial direction, it can greatly increase the axial FOV of the system, which is typically limited in a single-pinhole system due to the $\cos^3$ falloff of sensitivity shown in Equation 3. To demonstrate this difference, a defrise phantom similar to the one shown in Figure 2 (a) was simulated and reconstructed with both a single-pinhole (Figure 2 (b)) and a 4-pinhole (Figure 2 (c)) collimator. The distortion in the single-pinhole reconstruction is quite obvious near the ends of the axial FOV; the increase in sampling completeness when a 4-pinhole collimator is used clearly eliminates the artifact. Another alternative to increasing the axial FOV is to use a helical acquisition, which is described in more detail in section IV.4.2.

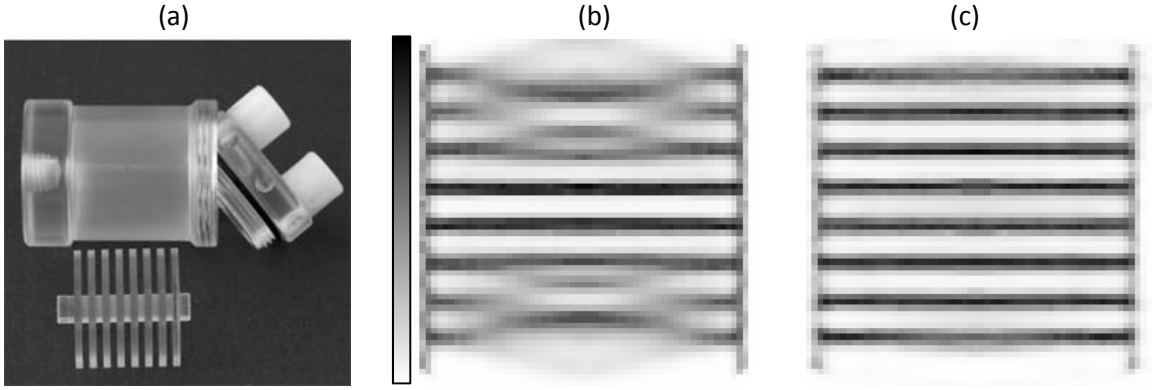

Figure 2: A photograph (a) of a typical small-animal defrise phantom (Data Spectrum Corp, Hillsborough NC USA) and simulations of a defrise phantom: (b) shows the results of a simulated defrise phantom with a single-pinhole acquisition. (c) is a slice through the reconstruction of the same simulated phantom in (b), except a 4-pinhole collimator was modeled. Note the significant reduction of artifacts in the axial FOV with the additional pinholes.

Although there are numerous benefits to using multiple pinholes, they also present several key challenges. The number of pinholes that can be used is limited by the surface area of the detector on which the pinholes are projecting. The detector size is limited by the overall system size and manufacturing limitations. Additionally, the focal length of the system and its magnification play a role – if pinholes are spaced too close together, or if the system's magnification is high, the projections may overlap, or multiplex on the detector, as seen in Figure 3. Multiplexing occurs when, due to the system configuration, photons from differing locations in the object can pass through different pinholes and end up interacting in the same location on the detector. Because of this, reconstruction algorithms cannot identify which pinhole a photon from the multiplexed region of the projection traversed through, and therefore leads to an increased

uncertainty in reconstruction. The overall system performance when multiplexing is present is no longer directly related to collection efficiency, even though the sensitivity is still linearly increased based on the number of additional pinholes (Kupinski and Barrett 2005). Systems that first utilized multi-pinhole collimators avoided multiplexing on the detectors (Vogel, Kirch et al. 1978; LeFree, Vogel et al. 1981), while those that utilized multiplexing followed later (Meikle, Kench et al. 2001; Wilson, Barrett et al. 2001; Schramm, Ebel et al. 2003).

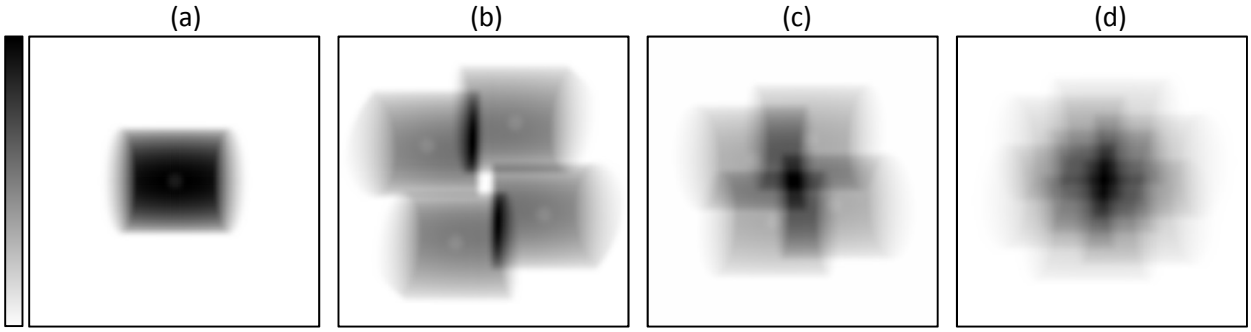

Figure 3: Projection images with varying multiplexing of a cold-spot phantom from (a) one pinhole, (b) 4 pinholes on a 10-mm diameter circle, (c) 4 pinholes on a 7-mm diameter circle, and (d) 7 pinholes on a 7-mm diameter circle. The amount of multiplexing increases as the pinhole spacing decreases and the number of pinholes increases, with 28.62%, 72.78%, and 94.35% overlap for (b), (c), and (d), respectively.

The tradeoff between the increased sensitivity of multiple pinholes and the ambiguity of photon origin due to multiplexing has been widely studied with no clear conclusion. For instance, (Mok, Yuchuan et al. 2009) simulated a variety of pinhole configurations that either (1) fixed the magnification and sensitivity, (2) fixed the sensitivity and varied the magnification, or (3) fixed the magnification and varied the sensitivity. This study design allowed for a quantitative comparison of the influences of all three factors of interest: system sensitivity, magnification, and by proxy the degree of multiplexing. The overall conclusions of this study were that some degree of multiplexing increases overall image quality up to a point and then after that point the benefit is decreased due to image artifacts. The point at which this switch occurs varies depending on the pinhole configuration, system magnification, and the activity distribution of the object being imaged. Further investigations into the effect of an object's activity distribution on multiplexing artifacts was studied in (Mok, Tsui et al. 2011), and demonstrated that certain object distributions such as a cool sphere inside of a hot background region have increased artifacts compared to a hot-rod and cold-rod phantom. These results are also

dependent on the system design, making the clear 'answer' to the optimal amount of pinhole multiplexing elusive. One way to determine an optimal number of pinholes is to choose a specific imaging task and, through simulation, determine the number and arrangement of pinholes for the task, such as Cao et al. performed for mouse brain imaging applications (Cao, Bal et al. 2005).

One alternative to the problem of multiplexing is to use a multi-pinhole collimator that has additional shielding between the pinholes and the detector that stops projections from overlapping. Vunckx et al. investigated this idea in simulation by comparing reconstructions of pinhole designs with varying degrees of multiplexing with and without a second shielding collimator that removes projection overlap. Their results agree with Mok et al. that smaller amounts of multiplexing do not adversely affect image quality, but when too much overlap was present reconstructions had severe ghosting artifacts. These artifacts were eliminated and image quality improved when the overlapping was removed from the projections by using the second shielding collimator (Vunckx, Suetens et al. 2008). They conclude that once the complete detector area has been used, the extra sensitivity due to multiplexing is only able to compensate for loss of information if a particular position in object-space has low sensitivity to other pinholes. The U-SPECT system, a high-resolution small-animal system (both version I and II), uses lead shielding between the multi-pinhole collimator and the detector to eliminate multiplexing in its projections (Beekman, van der Have et al. 2005; van der Have, Vastenhouw et al. 2009). The system was designed such that the projections span the majority of the detector's surface area to maximize the system's sensitivity as well.

II.2.2.3 Synthetic Collimation

Synthetic collimation was first suggested to mitigate multiplexing artifacts from multi-pinhole systems yet still give increased sensitivity and maintain good spatial resolution. Synthetic collimation uses a multi-pinhole collimator, but projections are collected at varying focal lengths such that the magnification and degree of multiplexing are varied. When data from a short and longer focal length are acquired and used in reconstruction it allows a combination of low-multiplexing, low-resolution data and high-multiplexing, high-resolution data to be combined for a higher-resolution image with less multiplexing artifacts (Wilson, Barrett et al. 2000). The initial simulation study showed improvements in

2D and 3D reconstructions with the synthetic collimation design over the more standard parallel hole collimators. Their group later built a physical system to experimentally investigate potential multiplexing effects and synthetic collimator options. The system incorporated 4 detectors around the imaging space with inter-changeable collimators that could be placed in a variety of distances from the detector, allowing independent, variable magnification for each detector head. Results showed pairing some multiplexing data with non-multiplexed data may lead to better performance in certain tasks (Hesterman, Kupinski et al. 2007; Hesterman, Kupinski et al. 2007). A more direct implementation of this idea was used for the SiliSPECT system, which utilizes two sets of stacked, stationary silicon detectors where the stacked configuration to acquire projections at different magnifications (McDonald 2010).

II.2.2.4 Coded Apertures

Another less common collimation method is to use coded apertures. Parallel hole collimators are often limited in resolution and while pinhole collimators can increase this resolution, they limit the sensitivity. Coded aperture imaging attempts to mitigate this tradeoff using a technique developed for X-ray and gamma-ray astronomy tasks. The coded aperture collimator is composed of a carefully designed pattern of many holes (on the order of hundreds) (Miller, Barrett et al. 2007), with an example pattern shown in Figure 4. Varying amounts of multiplexing are present in each of the hole's projections, and when projections are reconstructed using a method that deconvolves the coded (or highly-multiplexed) projections from the aperture mask, the original object distribution can be estimated in both 2D and 3D (Zhiping and Yi-Hwa 2006). A variety of reconstruction techniques have been used in attempts to apply these collimators to small-animal imaging (Meikle, Fulton et al. 2001), but they are often limited in image quality when there is a moderate amount of background activity and as of yet have not been widely applied.

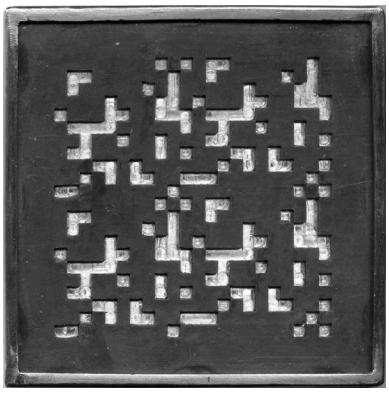

Figure 4: Photograph of an example coded aperture collimator, retrieved from: http://en.wikipedia.org/wiki/File:Coded_aperture_mask_%28for_gamma_camera%29.jpg

II.2.3 Image Reconstruction

An important part of a small-animal SPECT system is the reconstruction algorithm used to estimate 3D images from the acquired projection data. There are a wide variety of reconstruction methods available for use with SPECT systems, including both iterative and non-iterative methods. The most basic, non-iterative reconstruction scheme is filtered back projection (FBP), but this algorithm is not commonly used for small-animal SPECT systems (Webb 2003). This work will focus on iterative methods as they allow for the reconstruction to incorporate more physics-based effects such as blurring from the collimator, detector response, attenuation, and noise associated with photon counting. The down-side to using iterative methods is that reconstruction times are longer and implementation is more complex. Most of these types of reconstructions are based on the following formulation:

$$\boldsymbol{g} = \mathbf{H}\boldsymbol{f} \quad .$$

Equation 4

In this equation, **g** is the discrete projection data that is acquired, containing every detector element (*i*) for each projection image of the rotating camera system, ***H*** is the system matrix where h_{ij} represents the probability that a photon emitted in voxel *j* of image space is detected in bin *i* of the detector, and ***f*** is the object's activity concentration in the image-space, also known as the object function.

II.2.3.1 System Matrix Determination

The system matrix, *H,* can be obtained in a variety of ways, including experimentally-acquired, analytically derived, ray-tracing, simulated, or a combined method.

II.2.3.1.1 Experimentally-Acquired System Matrix

Experimentally-acquired system matrices are frequently used in stationary systems and avoid complex modeling estimations that other methods require. One of the benefits of this method is that effects such as depth of interaction (DOI), scatter in the collimator, spatial variations in the detector efficiency, and the relative locations (tilts/twists) of the pinhole and detector are built into the acquisition. These effects must be estimated or modeled in order to be included in the other methods of determining a system matrix. With rotational systems, this matrix is generally acquired at one angle and then subsequent responses for varying the angle of acquisition are calculated using geometry. Because of this, this type of system matrix may be less robust in non-stationary systems as errors from systematic orbit deviations are not included. This effect was studied with a system that used an analytical system matrix in conjunction with a geometrical calibration to determine orbit deviations and demonstrated that even small deviations between the actual orbit and the assumed circular orbit of the camera may introduce non-negligible bias on the estimated geometric calibration parameters that reduces reconstructed image quality (Lin, Vunckx et al. 2011).

To create the system matrix, a point source is traversed through image space and the point spread function (PSF) for each position in image space is recorded and stored (Furenlid, Wilson et al. 2004). The acquired data files tend to be extremely large and are usually required to be stored on disk, which potentially makes the reconstruction time very long. One method to reduce the matrix size and speed up reconstructions is to store the data as a sparse matrix, in which each PSF is stored as the location coordinates of positions that have counts and the number of counts that occurred at that location, instead of a matrix of every position where most values are zero. Another method used to help reduce the system matrix size is to estimate a Gaussian fit for each PSF and store the parameters needed to re-create the Gaussian shape: x center, x width, y center, y width, angle, and magnitude. These parameters can then be used on the fly to re-create the desired h_{ij} relation when needed in the reconstruction algorithm.

When the system matrix is acquired, the collection time at each position must be decay-corrected such that it matches the same number of total decays as the first position. Typically the voxel size of the reconstructed image is equal to the dimensions and size of the sampled system matrix. This implies that smaller step sizes will give better resolution, assuming the voxel size/system matrix step size has not reached the lower limit of the combined effect of the system's geometric resolution and detector's intrinsic resolution (Equation 2). But smaller step sizes require extended time for the system matrix itself to be acquired. Generally the isotope used for system matrix acquisitions is the same that will be used for imaging, with one common example being ^{99m}Tc (140 keV, $\tau^{1/2}$ = 6.02 hrs). This limits the total time one can acquire data before the source decays below the threshold needed to match the original position's total number of decays. Starting with a high activity point source (on the order of 111 to 185 MBq) allows for very short original collection times, but can still cause limitations if a finely-sampled image space is desired. One method to help alleviate this issue is to use the parameterized, Gaussian-fit data to interpolate the system matrix to a finer grid (Roney 1989). Two methods to perform this interpolation are described and compared in (Chen 2006), with the end result being that one can typically down-sample the system matrix by a factor of two (1 mm resolution to 0.5 mm resolution) with good results. Additionally, it was shown that an acquisition with a 4-mm step size can be interpolated to a 0.5 mm grid with equivalent results to a system matrix acquired with a 1-mm step size interpolated to 0.5 mm. Using this interpolation, the collection time at the first position (and all subsequent positions) can be increased which allows for a reduction in the noise of the measurement while still allowing for reasonable image resolution.

II.2.3.1.2 Analytically-Derived System Matrix

A second common way to determine a system matrix in SPECT is to do an analytical derivation. This involves first determining calibration parameters and second using analytical methods to estimate the sensitivity of each point in image space to each pixel in the detector. A geometrical calibration determines the relationship between the different axes/coordinate systems of interest such as the pinhole, detector, and object/image space. To quantify this in a single-pinhole system, seven parameters must be determined for cameras rotating on a circular orbit (Rizo, Grangeat et al. 1994; Noo, Clackdoyle et al. 2000).

There are two types of parameters, intrinsic and extrinsic. The intrinsic pinhole parameters are independent of the detector-pinhole location relative to the object-space and include the focal length, *f*, the distance from the center of the pinhole aperture to the detector plane, and the electrical shifts e_u and e_v, which relate the origin of the detector pixel grid to its position in the projection image caused by the detector hardware. The extrinsic parameters depend on the position of the detector with respect to the axis of rotation and can be described by their relationship to the central ray, which is a ray from the pinhole that orthogonally intersects the detector pixel grid. The mechanical offset, *m,* measures the offset of the central ray from the axis of rotation, and *d* measures the distance between the center of the pinhole and the axis of rotation along the central ray, determining the circular radius of rotation of the detector about the center of object-space. The tilt, φ, describes the angle between the detector and the axis of rotation, while the twist (ψ) angle describes the orientation of the detector's pixel grid around the axis of rotation (Beque, Nuyts et al. 2003). These parameters are shown in Figure 5.

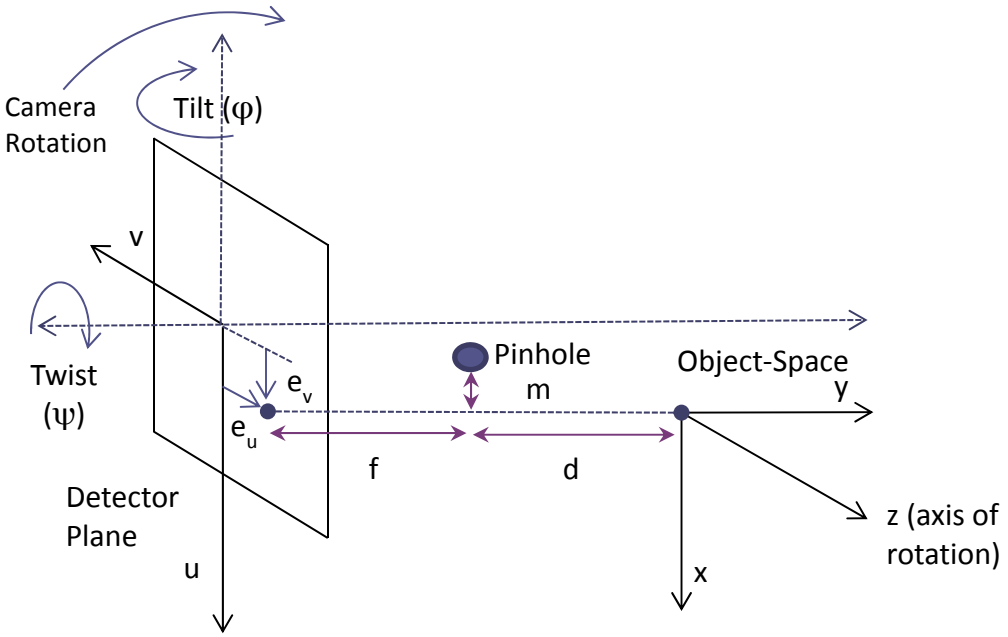

Figure 5: Schematic showing the relationship between the detector plane, pinhole and object-space, including the seven calibration parameters required to relate the three.

The general approach described by Noo et al. is divided into the following three major steps (Noo, Clackdoyle et al. 2000)

1. Measure the response of one or more point sources at N projection angles.
2. Determine analytic expressions that define a geometrical model that calculates the projections obtained in (1) from the set of calibration parameters. Use these projections to determine centroid positions.
3. Using an iterative, least-squares method, find the solution that minimizes the difference between the measured centroids determined in (1) with their estimates in (2) in order to estimate calibration parameters.

After the intrinsic and extrinsic calibration parameters are determined, the system matrix can be derived from the geometric relationship between the detector, collimator, and location in image space. Starting from the location in object-space, a ray is traced through the pinhole and subsequently to a position on the detector. Once the ray is known, the sensitivity of the position in object-space relative to the position on the detector can be calculated using Equation 3, and the pinhole diameter, focal length, and distance from the pinhole to the object-space are then used to estimate the Gaussian spread of the PSF from the ray position. This is done for every position in object-space and results in the system matrix estimation. A typical analytically-derived system matrix is calculated on the fly in order to avoid storing the entire system matrix in memory. If a system rotates about a gantry, the object-space can be transformed to the current angle of rotation to ensure the ray is projecting to the appropriate location on the detector. If a system rotating around a gantry has gravitational effects that cause changes in either detector angle or position relative to object-space at varying angles, then these need to be quantified and incorporated into the system matrix to ensure accurate reconstructions (Metzler, Jaszczak et al. 2007). Additional corrections can be added into the analytically determined system matrix to allow for better reconstructed image quality, such as modeling of pinhole penetration and adding resolution recovery, which corrects for the position-dependent blurring effect of the pinhole aperture that varies depending on the object-space voxel and the detector interaction location (Vanhove, Andreyev et al. 2007).

II.2.3.1.3 Ray Tracing Based System Matrix

Another method similar to the analytically-derived system method is to utilize ray-tracing techniques to determine the system matrix. This technique requires the same geometric calibration as described in the analytically-derived method, but implements the determination of the matrix slightly differently. Instead of using a single, central ray from the object voxel to a point on the detector and estimating its Gaussian spread, the ray-tracing method uses a number of rays that extend from the object voxel through the pinhole, some of which have a path through the pinhole and others through the collimator material surrounding the pinhole itself, and finally onto the detector.

For each ray, the PSF of each point in object-space is determined by calculating the probability of transmission through the aperture and the probability of absorption in the detector. The probability of transmission through the aperture is determined by the energy of the photon, the aperture material, and the length of the path the photon travels through the aperture material. The probability of absorption in the detector is also determined by the detector's material properties, the length of the path through the detector, and the energy of the photon. The rays chosen are uniformly spaced to pass through a slightly extended region of the pinhole itself. Then number of rays used can vary, but one small-animal SPECT system that utilized this method chose to use 100 (Schramm, Ebel et al. 2003). This allows for an estimation of the amount of penetration in the collimator. The contributions from all of the rays are then summed, and then this response is typically altered to include the detector's intrinsic resolution to form the PSF for that position in object-space. This process is then repeated for every voxel in object-space to determine the system matrix (Nuyts, Vunckx et al. 2009). The benefit of this system matrix is that it allows for proper modeling of more unique pinhole shapes, such as those tilted toward a central object region, and it inherently includes pinhole penetration.

II.2.3.1.4 Simulated System Matrix

Another method of determining a system matrix is through simulation. If the geometric calibration parameters are known, instead of analytically determining the resulting system matrix, Monte Carol simulations can be performed that incorporate many of the physical responses such as detector spatial resolution, detector energy resolution, and pinhole penetration (Vandenberghe, Staelens et al. 2006). The system design, which includes the pre-determined

calibration parameters, is used as an input into simulation software such as MCNP5 (Forster, Cox et al. 2004), a Monte Carlo simulation program for nuclear physics or GATE (Jan, Santin et al. 2004), a front-end package for GEANT (Agostinelli, Allison et al. 2003), for use in PET and SPECT simulations. A point source is then simulated with a certain amount of activity and moved through image space as in the acquired system matrix method. The benefit to this method is that the simulated point source will be precisely the exact size and activity chosen and will always be in a known location relative to the detector and collimator. The downside to this method is that it is biased to the accuracy of the calibration factors and requires long computational time. Also, this system matrix is generally computed once prior to reconstruction, and therefore requires storing and reading in of the large file during reconstruction.

II.2.3.2 MLEM Reconstruction

Once the system matrix has been estimated, reconstruction algorithms are then used to find the solution of the object function that best fits the data in *g* in Equation 4. In general, this is done iteratively by evaluating how well the current estimate of *f* matches the projection data, and then altering each subsequent estimate to obtain a better match (Bruyant 2002). The specific method of how the estimate is altered and what is considered to be a better match differs depending on the algorithm being used. This dissertation focuses on maximum-likelihood expectation-maximization (MLEM) and ordered subset expectation-maximization (OSEM) algorithms, although there are other iterative methods such as the algebraic reconstruction technique (ART) and maximum *a posteriori* (MAP) that can be used. An in-depth review of different iterative reconstruction techniques for emission tomography and their strengths and weaknesses can be found in (Qi and Leahy 2006).

The first step in determining an estimate of *f* is to define the criteria for judging which image is the best estimate of the true distribution. In this case we will focus on the ML criterion, which picks the object function with the highest likelihood of creating the data *g*. In order to determine ML criteria it is first necessary to determine the likelihood of a given object function guess. If *m* is the number of voxels in image space and *n* is the number of elements in the projection data, then the mean number of events in the detector bin *i* is:

$$\bar{g}_i = \sum_{j=1}^{m} h_{ij} f_j \ .$$

Equation 5

As the number of photons emitted from an image voxel *j* and subsequently detected by detector bin *i* is a Poisson variable, then the Poisson distribution can be used to determine the probability of detecting a given number of events in the detector bin *i*:

$$P(g_i) = \frac{\bar{g}_i^{g_i}}{g_i!} e^{-\bar{g}_i} \ .$$

Equation 6

The maximum of this probability occurs when $g_i = \bar{g}_i$, which starts the framework of the desired likelihood function. The likelihood function is defined as the probability of the projection data *g* given the object function *f*, which is the product of the probability of each detector bin location:

$$L(\boldsymbol{f}) = Pr(g|\boldsymbol{f}) = P(g_1)P(g_2)\dots P(g_n) = \prod_{i=1}^{n} \frac{\bar{g}_i^{g_i}}{g_i!} e^{-\bar{g}_i} \ .$$

Equation 7

This equation can then be re-written in terms of the natural-log likelihood, denoted $l(\boldsymbol{f})$, and when substituting the definition of $\bar{g}_i$ can be written as:

$$l(\boldsymbol{f}) = \ln\big(L(\boldsymbol{f})\big) = \sum_{i=1}^{n} \left(-\sum_{j=1}^{m} h_{ij} f_j + g_i \, ln \left(\sum_{j=1}^{m} h_{ij} f_j \right) - \ln(g_i!) \right) .$$

Equation 8

This more commonly used form of the likelihood equation allows one to calculate the probability of observing a data set for a given object function. It was shown in (Kaufman 1987) that there is exactly one maximum in this function, giving rise to a single, unique solution. Because of this, we can apply basic calculus to determine the maximum by setting the derivative of the function equal to zero:

$$\frac{\partial l(\boldsymbol{f})}{\partial f_j} = -\sum_{i=1}^{n} h_{ij} + \sum_{i=1}^{n} \frac{g_i}{\sum_{j'=1}^{m} h_{ij'} f_{j'}} h_{ij} = 0 \ ,$$

Equation 9

and this equation can then be solved for the object function and arranged into an iterative form:

$$\hat{f}_j^{(k+1)} = \frac{\hat{f}_j^{(k)}}{\sum_{i'=1}^{n} h_{i'j}} \sum_{i=1}^{n} h_{ij} \frac{g_i}{\sum_{j'=1}^{m} h_{ij'} \hat{f}_{j'}^{(k)}} \ .$$

Equation 10

Using the iterative form of Equation 10, one can now implement the MLEM algorithm. In order to begin the iterative method a first estimate is needed, and is typically chosen as a uniform value over the entire image space. The initial values must not be negative or zero, as the multiplicative method of this algorithm would cause negative or zero values in all subsequent estimates; a common value chosen to start with is one. To implement this function, the current guess or estimate of the object function $\hat{f}_j^{(k)}$ is forward projected to determine its estimated projection data ($\sum_{j'=1}^{m} h_{ij'} \hat{f}_{j'}^{(k)}$). The experimental data is then divided by the estimated projection at each element in the data vector. This ratio is then back-projected into image space ($\sum_{i=1}^{n} h_{ij} \frac{g_i}{\sum_{j'=1}^{m} h_{ij'} \hat{f}_{j'}^{(k)}}$) where it is multiplied by the previous iteration's object function estimate ($\hat{f}_j^{(k)}$) and then normalized by a sensitivity factor ($\sum_{i'=1}^{n} h_{i'j}$) to obtain the newest object function estimate ($\hat{f}_j^{(k+1)}$). This derivation was based on the work of (Shepp and Vardi 1982; Lange and Carson 1984; Bruyant 2002).

This method is repeated for a number of iterations, but is usually stopped before full convergence. As all experimental data sets have some amount of noise present, if the maximum likelihood algorithm is allowed to run to convergence, its final solution of the algorithm will be matched to noisy projection data. This implies that the MLEM solution is not necessarily the optimal reconstructed image, because stopping before convergence may lead to less noisy images. This leads to an uncertainty in the number of iterations that should be completed before stopping the reconstruction, as too few or too many can lead to images that do not accurately represent the true object function. Additionally, as each iteration requires multiple accesses to various system matrix elements in addition to forward and

back projection calculations, this method is computationally expensive and more iterations can lead to lengthy reconstruction times.

II.2.3.3 OSEM Reconstruction

To lower computation time, OSEM, an alternative version of MLEM, was developed that uses the concept of ordered subsets. This speed-up is accomplished by dividing the projection data into groups, or subsets, and then performing the MLEM reconstruction update as in Equation 10 sequentially on each subset of data, with the object function estimate ($\hat{f}_j^{(k)}$), being updated after every subset instead of after all data as in MLEM.

First, the number of subsets is chosen, which is a tradeoff between the convergence speed, where more subsets converge faster, and accuracy, where final reconstructions may not converge to the optimal reconstruction if too many subsets are used. The number of projections per subset is then determined by dividing the total number of projections acquired during acquisition by the number of subsets. Ideally subsets should contain projections with angles that are spaced out evenly over the typical 360° acquisition range to give good spatial sampling of the object within each subset. For example if 16 camera angles were acquired over 360° and 4 subsets were desired, then each data subset should consist of 4 projection angles that are 90° apart. Systems with more than one detector allow for subsets to consist of projections obtained from all detectors to ensure even spacing.

After defining which projections are included in each subset, implementing the algorithm is similar to that of MLEM. A complete iteration is defined as performing an MLEM update for all subsets, or four in the example above. The MLEM algorithm is performed sequentially for each subset with the estimate of $\hat{f}_j^{(k)}$ being updated after each subset. The OSEM implementation, with S_i being each subset of projections, is as follows:

$$\hat{f}_j^{(k+1)} = \frac{\hat{f}_j^{(k)}}{\sum_{i' \in S_{i'}} h_{i'j}} \sum_{i \in S_i} h_{ij} \frac{g_i}{\sum_{j'=1}^{m} h_{ij'} \hat{f}_{j'}^{(k)}} \ .$$

Equation 11

This allows for all of the data to be incorporated into each iteration as with the MLEM algorithm, but because each iteration is divided into a number of subsets, it leads to faster converge than MLEM. The main caveat to this

method is that there is no theoretical proof that the reconstruction moves toward the maximum likelihood solution as MLEM does, but as most reconstructions are stopped before convergence, this is usually not a major concern (Hudson and Larkin 1994).

II.3 SPECT Detectors

As previously discussed, SPECT image acquisition requires a detector or multiple detectors paired with a collimator, acquisition protocol, and reconstruction algorithm in order to produce 3D images. The general overview of image formation using collimators and typical reconstruction algorithms were previously overviewed in section II.2. This section will focus on introducing various detector types and their properties, and a discussion of their strengths and weaknesses.

II.3.1 Scintillator Detectors

When a gamma ray interacts within a scintillator-type material, the gamma ray creates an inner shell vacancy and an excited primary electron. These electron-hole pairs stay together as loosely bound pseudoparticles known as excitons. They diffuse in the bulk of the detector material until they reach luminescent sites, which are areas of the detector lattice that have discontinuities due to the presence of dopant material, and then the electron-hole pairs recombine and emit secondary scintillation light with wavelengths that are dependent on the specific scintillator material. This light is subsequently detected and transferred into an electric charge by photomultiplier tubes (PMTs) or photodiodes, which is then used to determine an estimate of the photon's deposited energy and interaction position (Kupinski and Barrett 2005; Peterson and Furenlid 2011). A wide variety of scintillator materials exist, but NaI(Tl) is most commonly used for nuclear imaging applications and was first demonstrated as a detector in 1948 (Hofstadter 1948). It is still in use today due to several key factors. First, it can achieve good detection efficiency with a relatively thin crystal at 140 keV (from ^{99m}Tc), having a linear attention coefficient of 3.12 cm^{-1}. Also, when photons interact in the detector and energy is absorbed, it emits a large number of optical photons, 38 photons per keV, which is required in order to achieve good spatial and energy resolution. Additionally, the detector crystals can be grown up to ~80 cm in diameter

which allows for single crystals to be used for applications requiring large detector areas (Peterson and Furenlid 2011). Systems using scintillators require methods to turn the output of PMTs into appropriate position estimates, which is most commonly accomplished by using Anger Logic (Anger 1958), although maximum-likelihood estimation methods have been more recently developed and implemented (Barrett, Hunter et al. 2009).

When using NaI(Tl) scintillator detectors in conjunction with ^{99m}Tc at 140 keV these systems typically have an energy resolution of ~10% (Hwang, Franc et al. 2008) and an intrinsic spatial resolution of ~3 mm full width at half maximum (FWHM) (Knoll 2000). Scintillators typically require approximately 100 eV of deposited energy to create a single photoelectron. This results in only a few thousand photoelectrons being produced for a single interaction and creates photo-emission totals that are dominated by Poisson statistics. Because of this, NaI(Tl)based scintillator detectors are limited to having energy resolution in the range of 10% at 140 keV or 6% at 0.662 MeV (Knoll 2000). Other types of scintillator materials that have been developed can provide better energy resolution, such as LaBr which has been shown to have 5% energy resolution at 511 keV (Kuhn, Surti et al. 2006), but there are usually trade-offs associated with their ability to attenuate gamma rays, light yield (eV per photoelectron), emitted light wavelength, or the decay time.

Several commercial small-animal SPECT systems utilize scintillator detectors including: Bioscan NanoSPECT-CT (Forrer, Valkema et al. 2006), MILabs U SPECT II (van der Have, Vastenhouw et al. 2009), and Siemens Inveon SPECT (Magota, Kubo et al. 2011). These systems have large magnification factors to obtain reasonable spatial resolution, multi-pinhole collimators to increase system sensitivity, and a variety of reconstruction correction factors, such as attenuation and scatter to allow for more accurate quantitative images.

II.3.2 Semiconductor Detectors

Although scintillator detectors have been the workhorse for nuclear medicine since the 1950s, the use of semiconductor detectors is being investigated and is slowly growing in popularity. The main advantages over scintillators are that they have better energy resolution and there is a direct conversion from photon interaction to electric charge – no PMT is necessary to turn light output into an electrical current. Some semiconductor systems need to be cooled while

others operate at room temperature. There are several semiconductors being investigated for nuclear imaging detectors such as: cadmium telluride (CdTe), cadmium zinc telluride (CZT), silicon (Si), and HPGe. This section will briefly address the physics of how semiconductor detectors function and then discuss some of the relative strengths and weaknesses of each type.

II.3.2.1 Physics of Semiconductors

Semiconductors are able to conduct electricity under specific conditions. When a gamma ray deposits energy into the bulk of the detector, whether from Compton or photoelectric interactions, it produces a high-energy electron which subsequently dissipates its energy by a cascade of interactions. There are two main parts of this cascade; the first involves the high-energy electron dissipating energy by generating phonons, or lattice vibrations, and the second produces electron-hole pairs by exciting electrons across the band gap. In the case of semiconductor detectors, the creation of electron-hole pairs in this cascade is what is used to sense the charge deposited by the gamma ray, while the phonons lead to a loss in energy collection (Kupinski and Barrett 2005).

In the absence of an external bias voltage, these electron-hole pairs diffuse away from their point of origin via random thermal motion. This diffusion leads to a broadening distribution of the charges as a function of time. But semiconductor detectors operate under a bias voltage that creates an electric field in the bulk of the detector, and therefore the motion of the electron-hole pairs is determined by the combined effect of random thermal velocity and a net drift velocity parallel to the direction of the applied field. As electrons move in the direction opposite to the applied electric field, holes 'move' in the direction of the electric field by disappearing and reappearing in the locations that the electrons move to and from, respectively. Holes act as a positive charge as they represent the absence of a negatively charged electron (Knoll 2000). This concept is illustrated in Figure 6.

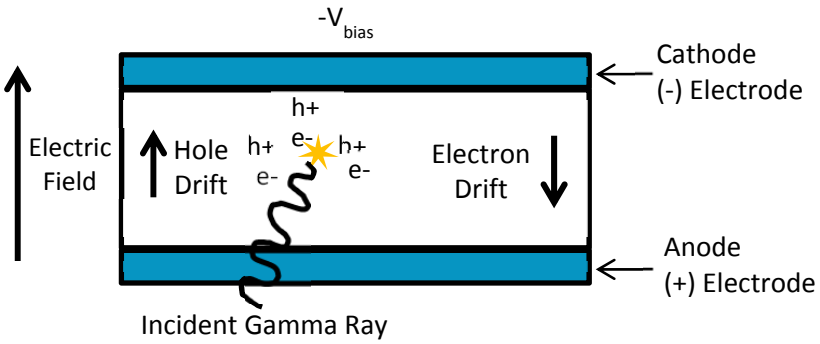

Figure 6: Basic semiconductor detector interaction showing the direction of the bias voltage that causes the electron-hole pairs to propagate through the detector material.

The movement of holes and electrons through the bulk of the detector induces a time-varying charge on the readout electrodes, which produces a measureable current in the external circuit. This current is then used to estimate position and energy. The magnitude of the induced charges gives an estimate of the energy deposited, while the position estimate is dependent on the configuration of the detector's collecting electrodes. Two detector configuration types are shown in Figure 7. The first, Figure 7 (a) is a double-sided strip detector (DSSD), where charge is collected and read out at a strip level from the front and back of the detector, which allows for the determination of the position in the x (back) and y (front) direction. Figure 7 (b) is a pixelated detector, where readout occurs on one side of the detector at each pixel. The pixelated readout requires significantly more readout electronics than the double-sided strip configuration.

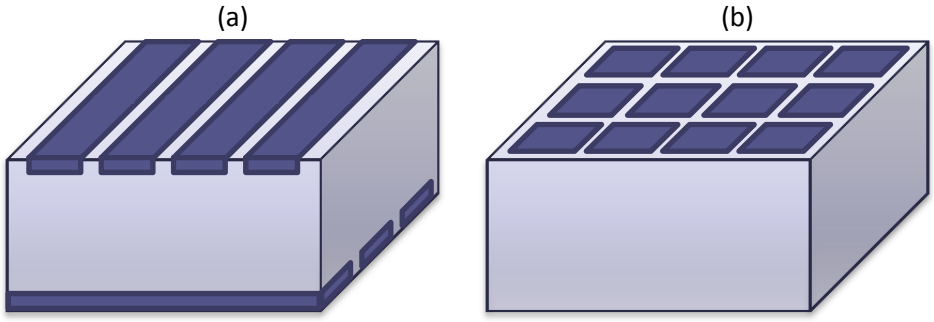

Figure 7: (a) shows a typical schematic of a double-sided strip detector while (b) shows the configuration of a pixelated detector. In the former case, readout electronics are placed on every strip, while the latter requires significantly more readouts, one at each pixel.

II.3.2.2 Properties of Semiconductor Detectors

II.3.2.2.1 Bandgap

The bandgap is the energy required to excite an electron from the valence band to the conduction band, which creates an electron-hole pair. In the case of semiconductors used as detectors, the bandgap influences two major detector properties: the amount of random noise due to thermal excitations (leakage current) and the number of electron/hole pairs that are generated per amount of deposited energy.

The number of random thermal excitations that contribute to noise in detector is dependent on both the operating temperature and the bandgap of the detector. The higher the bandgap and the lower the operating temperature, the more energy is required for the electrons and holes to move within the material, which makes the probability of random thermal excitations that cause leakage current and subsequently noise in projection data less likely. If a bandgap is extremely low (< 1 eV), the detector must be cooled to cryogenic temperatures in order to reduce these thermal excitations and the subsequent associated noise. The benefit of lower bandgap energy is that more electron/hole pairs are generated per eV of deposited energy, which gives rise to a larger signal and subsequently an improved estimate of the energy deposited in the detector (Knoll 2000).

II.3.2.2.2 Electron and Hole Mobility and Mobility-Lifetimes

Another set of semiconductor properties that affect image quality is the electron/hole mobilities and mobility-lifetimes. The electron (μ_e) and hole (μ_h) mobility are the constants of proportionality that relate the net drift velocity to the electric field magnitude. This proportionality constant corrects for the loss of speed due to interactions with phonons and impurities. When the electrons and holes are free, or in the conductance or valence bands, respectively, they move at their drift velocity, but can become trapped at sites of impurities or lattice defects.

The lifetime (τ) is the mean time that an electron or hole travels before becoming trapped, with increased lifetimes allowing for the average hole or elector to travel longer, and therefore creating more charge collection and subsequently more signal per interaction. Frequent charge trapping, or a small lifetime, causes worsening of the detector's energy resolution as not all of the energy deposited from the gamma ray is detected, causing a distinct tailing

on the lower-energy side of a photopeak. The mobility-lifetime product combines the mobility and lifetime of a specific charge carrier in a specific detector type and indicates how large of an effect charge-trapping has on overall mobility (Kupinski and Barrett 2005).

II.3.2.2.3 Other Properties

The bias voltage across a detector, which creates the electric field, also plays a role in how fast the holes and electrons propagate to the readout strips of the detector, with a higher bias voltage leading to faster propagation speeds. As with scintillator detectors, the efficiency of the detector is related to the atomic weight and material density, and is commonly characterized through the linear attenuation coefficient at a specific energy (Knoll 2000). A summary of the properties of commonly used semiconductor detectors is shown in Table 2, adapted from (Barber and Woolfenden 1996), and the benefits and challenges of each detector type are discussed in detail in the following sections.

Table 2: Semiconductor detector properties

Property	CdTe	CZT	Si	HPGe
Attenuation Coefficient 140 keV (cm^{-1})	3.22	3.07	0.02	0.72
Bandgap (eV)	1.6	1.6	1.12	0.74
Energy per electron-hole pair (eV)	4.43	4.4	3.61	2.98
Electron mobility ($cm^2V^{-1}s^{-1}$)	1100	1000	1350	36,000
Hole mobility ($cm^2V^{-1}s^{-1}$)	100	100	480	42,000
Electron mobility-lifetime (cm^2V^{-1})	3×10^{-3}	3×10^{-3}	0.42	0.72
Hole mobility-lifetime (cm^2V^{-1})	5×10^{-4}	5×10^{-4}	0.22	0.48

II.3.2.3 Cadmium Telluride and Cadmium Zinc Telluride

Cadmium telluride (CdTe) and cadmium zinc telluride (CZT) are some of the more widely used semiconductor materials for nuclear medicine detectors. They both have a high density, 5.85 and 5.82 g cm^{-3} for CdTe and CZT, respectively, giving good attenuation at 140 keV (3.22 and 3.07 cm^{-1} for CdTe and CZT, respectively). They have bandgaps of 1.6 eV, allowing them to operate at room temperature. They have lower hole mobility than electron mobility, 100 and 1100 $cm^2V^{-1}s^{-1}$ for CdTe electrons and holes, respectively, and also have lower mobility-lifetime products than Si or Ge, 3×10^{-3} cm^2V^{-1} for CdTe and CZT electrons, while Si and Ge electrons have 0.042 and 0.72 cm^2V^{-1}, respectively (Barber and Woolfenden 1996).

The lower mobility-lifetime products cause a very visible tailing effect, demonstrated in Figure 8, which includes a measured pulse-height spectrum of a ^{99m}Tc point source acquired on a CZT detector in a molecular breast imaging system (Hruska and O'Connor 2008). In SPECT, tailing either leads to the counts in the 'tailing' region being rejected, lowering system sensitivity, or requires an increased energy window that will include more of the tailed events, but will also increase the number of scattered photons included, which will add noise into the reconstructed images.

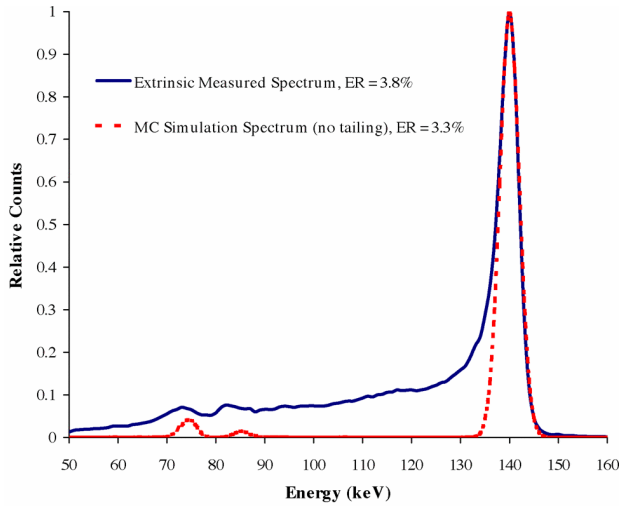

Figure 8: A flood acquisition from a ^{99m}Tc point source on CZT-based LumaGem system published by (Hruska and O'Connor 2008), © 2008 IEEE. The wide 'tail' to the left of the energy peak is due to the incomplete charge collection due to lower charger mobility-lifetime. The dotted red line is the results of a simulation showing what the peak would look like without the charge trapping.

The amount of trapping is dependent on the DOI when there is a difference in the hole and electron mobility-lifetime products, as in the case of CdTe and CZT. If an interaction occurs near the cathode, holes have a short distance to travel to the cathode-side collecting electrode and are more likely to have their induced charge increase the output current signal. An interaction near the anode side would have the opposite effect, with holes contributing to the signal collected at the anode side as they move toward the cathode and not the cathode side as they become trapped before reaching the cathode-charge collecting strip's electric field.

In a pixel-type detector, this effect can be mitigated by utilizing the small-pixel effect (Barrett, Eskin et al. 1995). To ensure collection of the holes' signal, the pixel readout is placed on the cathode side of the detector and the pixel dimensions are made to be several times smaller than the detector thickness. When the dimension of the pixel is much

smaller than the thickness of the detector, the collecting electrode's electric field weighting only extends into the detector to approximately the width of the pixel itself. This makes the pixel only sensitive to charge carriers that move to a depth of the pixel width or less. The electrons, which have less trapping than the holes, add to the collective signal as they move away from the cathode to the anode, while the holes, which only have to travel a short distance in order to be collected, have a smaller probability of being trapped before reaching the cathode. This reduces the tailing effect that is influenced by the different mobility-lifetime products between the holes and electrons. While this method depends on the thickness of the detector and does increase the spatial resolution, it can lead to charge being distributed across multiple pixels resulting in a more complicated signal read-out being required (Peterson and Furenlid 2011).

As CZT and CdTe are most commonly-investigated semiconductor detectors for use with small-animal imaging, there are a variety of systems in which they are used. The University of Arizona developed the SemiSPECT system, which uses eight CZT detector arrays positioned around a rotating object (Kim, Furenlid et al. 2006). One small-animal tri-modality commercial system was developed by Gamma Medica-Ideas that can acquire SPECT, PET, and CT images on the same animal bed. This system uses CZT detectors for the SPECT acquisitions, which have a helical acquisition and multi-pinhole apertures (Parnham, Chowdhury et al. 2006).

II.3.2.4 Silicon

Silicon has good charge mobility (0.42 and 0.22 $cm^2V^{-1}s^{-1}$ for electrons and holes, respectively) and mobility-lifetimes. It has a bandgap of 1.12 eV which allows it to be operated at room temperature. Silicon has a low atomic number (14) and a lower density (2.33 g/cm^3) relative to CZT, which contributes to its low linear attenuation coefficient of 0.02 cm^{-1} at 140 keV. The majority of photon interactions with energies above 55 keV Compton scatter (Barber and Woolfenden 1996). Although it is not commonly used in imaging due to this low efficiency at higher energies, it has been used in a high-resolution system, SiliSPECT, for use with detecting ^{125}I-labeled tracers, as the vast majority of its emission energies are between 27 and 35.5 keV, where the system has a reasonable intrinsic efficiency of around 36% (Shokouhi, McDonald et al. 2009). It also gives good energy resolution, with the SiliSPECT system having a resolution of 5 keV at 28 keV (McDonald 2010). Similar detectors are also being used in a cross-slit collimator system (Durko, Barrett et al. 2012).

Another group also proposed a small-animal imaging system for ^{125}I imaging using a lithium-drifted silicon detector that has an increased detection efficiency, where the additional lithium drifting allows for manufacturing of thicker detectors (up to 1 cm) and to have larger active areas (10 cm × 10 cm) (Choong, Moses et al. 2005).

II.3.2.5 Germanium

Germanium has a narrow bandgap energy of 0.74 eV, and is therefore required to operate at cryogenic temperatures to minimize leakage current. It has a density of 5.23 g cm^{-3}, an atomic number of 32, and a linear attenuation coefficient of 0.72 cm^{-1} at 140 keV. HPGe requires a thicker detector than CdTe or CZT to achieve equivalent absorption for higher energy photons due to HPGe's lower attenuation coefficient. It has very high charge mobility and mobility-lifetime (0.72 and 0.48 cm^{2}V^{-1} s^{-1} for electrons and holes, respectively) and therefore does not suffer from charge trapping and subsequently does not have the tailing effect problems of CZT (Barber and Woolfenden 1996). Because of these properties it has potential for use in medical imaging applications and will be discussed more in depth in the following section.

II.4 Germanium Imaging Systems

II.4.1 Introduction

Attempts to apply segmented germanium planar detectors to nuclear medicine imaging extend back at least forty years, with one of the earliest used for imaging having a DSSD design (McCready, Parker et al. 1971). This group used a germanium detector that was 44 mm × 44 mm and 10 mm thick with a square bore collimator. It had 3 mm spatial resolution which was limited by the distance between the electrical contacts used for readout of signal. Both a rat and human thyroid image using ^{99m}Tc – pertechnetate were acquired with this detector and with a standard gamma camera system, with results showing significantly better localization of the thyroid in the germanium system. Although these first results showed promise, these early efforts were hindered by difficulties with detector fabrication, cumbersome electronics, and limited computing power, in addition to the need for a bulky liquid nitrogen dewar to achieve required operating temperatures (Rusinek, Reich et al. 1980; Hasegawa, Stebler et al. 1991).

II.4.2 Recent Progress Using Germanium

Advances in electronics in addition to compact mechanical cooling systems have made HPGe systems much more feasible for biomedical applications. Common recent applications have focused on environmental remediation (Phlips, Johnson et al. 2002), astrophysics (Kurfess, Johnson et al. 2000; Wulf, Phlips et al. 2003; Bellm, Boggs et al. 2009), and homeland security (Perez-Andujar and Pibida 2004) but the latest generation of position-sensitive HPGe detectors have not been widely investigated for biomedical imaging.

II.4.2.1 Recent Biomedical HPGe Studies

The only other group as of the time of writing that has recently investigated HPGe for biomedical imaging is the Liverpool group, who have focused on applications for PET and Compton imaging (Cooper, Boston et al. 2007). They developed the SmartPET system, which consists of a dual-headed HPGe system having detectors with 60 mm × 60 mm x 20 mm active volume with 12 × 12 orthogonal strips with a 5 mm strip pitch. This system has an absolute efficiency for coincident detection of approximately 1% at 511 keV and a spatial resolution of approximately 3 mm. It also requires liquid nitrogen dewars to maintain detector operating temperature (Cooper, Boston et al. 2009). The benefit of HPGe's energy resolution in PET is that it can potentially allow some events that are Compton scattered within the detector to be recovered in order to help increase efficiency. In SmartPET, this recovery is important due to the limited stopping power of the 20 mm thick detectors at 511 keV. These detectors are also being investigated for Compton imaging of lower-energy radiotracers such as ^{99m}Tc and ^{123}I. A simulation study was discussed in (Harkness, Boston et al. 2009) and pulse shape analysis improvements were presented in (Cooper, Boston et al. 2007; Cooper, Boston et al. 2009).

While one group has published results of germanium strip detector performance (Gros, Hammond et al. 2009), their testing focused on characterizing the degree of charge sharing between strips, charge loss, and the influence of detector design on these problems. This investigation compared several different commercially available planar detectors that had a combination of different strip patterns, bias voltages, crystal dimensions, and readout contact types (lithium diffused/boron implanted or amorphous-Ge). This paper concludes with recommendations on detector testing

that identify issues with guard ring size, passivation of detector edges, grounding and impedance matching, cross-talk effects, capacitive coupling, and charge losses within strips or due to inter-strip gaps.

II.4.2.2 Sub-Strip Position Estimation

Another important area of work that led to germanium systems having potential applications in medical imaging is the ability to estimate position at a sub-strip level. Although DSSDs can be manufactured in a wide range of strip pitches, there is a tradeoff when choosing the strip size. Assuming the gap size is kept constant, if a narrow strip size is chosen then the active surface area of the detector decreases due to the presence of more gaps, decreasing the efficiency of the system. This also increases the chance that charge will be collected on multiple strips, which will lower efficiency if additional signal processing is not performed. On the other hand, if the strip width is too large it limits the spatial resolution of the system. More strips present on a detector also require additional readout electronics for the extra channels, causing an increase in the overall cost of the system. In order to circumvent this tradeoff, a method was developed to overcome spatial resolution limits without decreasing the strip pitch. This method uses the induced charges from neighboring strips to estimate position at a finer resolution than the strip pitch.

Using induced charges from neighboring strips was first investigated for use in germanium systems designed for Compton imaging. Figure 9 shows an example of normalized signals of both the charge-collecting strip and its two adjacent neighbors for the front (positive amplitudes) and back (negative amplitudes) of the detector. A difference-ratio of the maximum amplitude of the induced transient signals on the neighboring strips can be calculated to determine an estimate of interaction position within a strip. This is calculated by using:

$$Strip\ Position \propto \frac{(A_R - A_L)}{A_R + A_L} \ ,$$

Equation 12

where A_R and A_L are the maximum amplitudes of the nearest right and left neighbors, respectively. This method is applied in both the X and Y dimensions to achieve sub-strip resolution in both dimensions (Vetter, Burks et al. 2004). This benefit of sub-strip interpolation can be seen in Figure 10, where a simple 12 mm diameter pinhole projection is shown with the original image and with an 8 × 8 interpolation grid. The interpolated image has a much more clearly

defined pinhole outline than the original image, although there is some pile up of charges on edges near the gaps (Burks, Jordan et al. 2004).

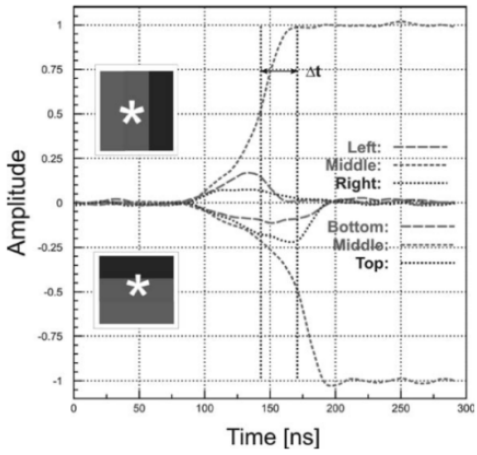

Figure 9: Example of normalized signals on the back and front of a detector for both the charge-collecting strip and the induced charge on the right and left neighbors, reprinted from (Vetter, Burks et al. 2004), with permission from Elsevier.

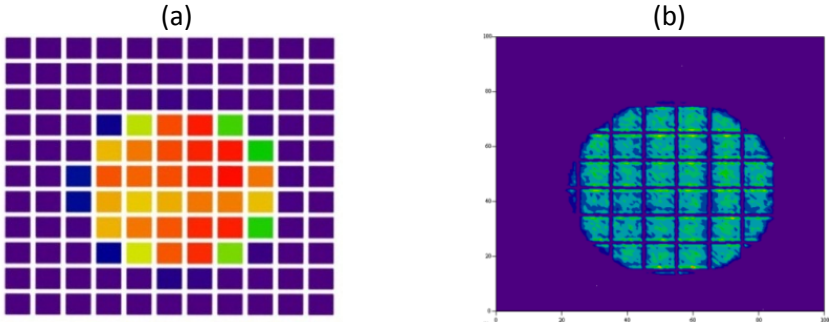

Figure 10: Shows a pinhole projection of a point source without (a) and with (b) sub-strip position estimation, with (b) showing the dramatic resolution increase (Burks, Jordan et al. 2004).

The same group also simulated a model of the electric field of the detector and determined the trajectory of the drifting charges in the detector. They measured the induced charge on the neighboring strips for a given interaction with the final signal including the superposition of the induced signals from both the drifting holes and electrons. Using the simulation results, the difference between the area under the curve of the right and left induced signals were calculated as a function of depth to create a calibration table. The different slopes of these depth-specific calibrations can be seen

in Figure 11, where Z = 2 mm is clearly the least sensitive as its induced signals were very bipolar (Burks, Jordan et al. 2004).

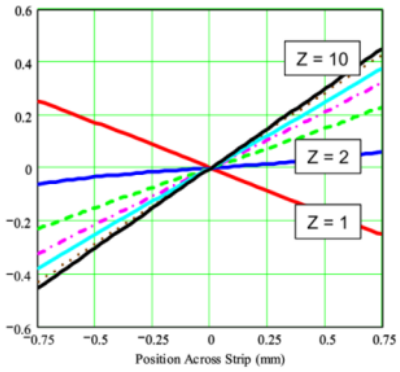

Figure 11: Shows the difference between the area under the curve of the induced charge on strips on the right and left of the charge-collecting strip. The effects of the bipolar nature of some of the depths can be seen (Z = 2 mm) as their slope is relatively closer to zero than at other depths (Burks, Jordan et al. 2004).

Although there are an equal number of electrons and holes created at each simulated depth, the amount of signal they induce individually on neighboring strips is dependent on the original photon's depth of interaction due to their differing lengths of travel to the appropriate electrodes and the amount of charge trapping that occurs during the movement. For interactions near the cathode, the holes travel a very short distance while the electrons travel the length of the detector, making the induced signal on neighboring strips dependently mainly on the electron travel. The opposite is true for interactions near the anode. Depending on the material properties and the applied bias voltage, the movement of electrons and holes combine to produce very little induced charge due to their bipolar nature, such as depth Z = 2 mm in Figure 11.

II.5 Potential Benefits of HPGe-SPECT

II.5.1 Benefits of Excellent Energy Resolution

One of the most obvious benefits to using HPGe for SPECT imaging is its excellent energy resolution. One main impact of this in SPECT is the ease at which multi-isotope acquisitions can be acquired. Figure 12 shows a simulated dual-isotope (^{99m}Tc at 140 keV, ^{123}I at 159 keV) pulse-height spectrum for a system with 10% energy resolution (red) and

1% energy resolution (blue). It is clear from this figure that the 1% energy resolution allows for easier separation of the different photopeaks than that of the 10% as there is no overlap in the 1% system. Although methods have been developed to estimate what portion of photons originate from which radiotracer in the overlapping region of the 10% energy resolution case (Kacperski, Erlandsson et al. 2011), it is still beneficial to avoid an additional correction estimation. Another benefit to having a more narrow energy window is the ability to exclude down-scattered photons. A photon emitted at the higher emission energy can scatter (either in the object, collimator, or detector), lose energy, and subsequently fall into the energy window of the lower emission energy, which causes noise in the projections and subsequent reconstructions. When the energy window is narrowed, the probability that these down-scattered photons will fall within the lower energy window is decreased, and therefore lowers noise in the reconstructed image.

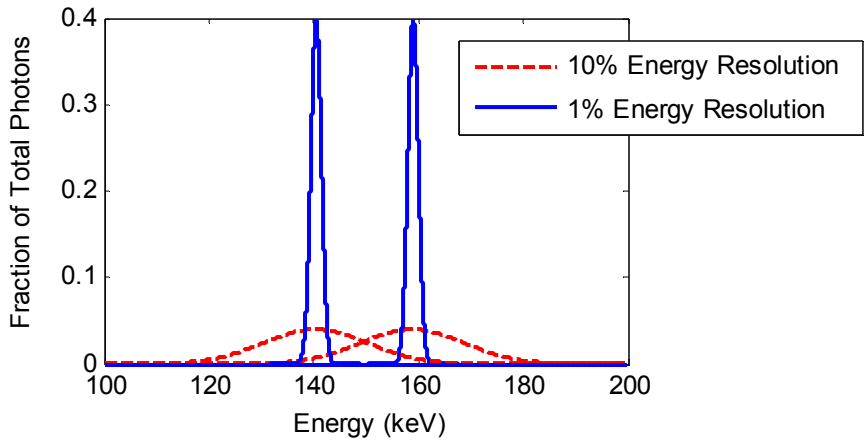

Figure 12: Simulation of a dual-isotope pulse-height spectrum for a system with 10% (red) and one with 1% (blue) energy resolution. It clearly shows that energy windows in the 1% system can be used to easily separate the two photopeaks, while the 10% system would require more a more complicated separation scheme.

Additionally, in single-isotope acquisitions, the number of scattered photons that are included in the image reconstruction can be reduced by again choosing a narrower energy window. Although the energy window can be narrowed in all detector types, only systems with good energy resolution can do this without eliminating a large portion of true counts in conjunction with the noise-inducing scattered counts. While scatter may not be as much of a problem for small-animal SPECT as it is for human studies, it still can affect the quantitative accuracy of the resulting images. Both Hwang and Vanhove found that the scatter-to-primary ratio was on the order of 10% for rat-sized objects with ^{99m}Tc

imaging using a NaI(Tl) detector (Hwang, Franc et al. 2008; Vanhove, Defrise et al. 2009). Chen et al. found that failure to compensate for scatter led to an over-estimation of 9.1% in a SPECT reconstruction of the activity of a small source inside of a rat-sized cylinder of water (Chen, Wang et al. 2009). While a number of scatter-correction techniques have been developed (Hutton, Buvat et al. 2011), it is undoubtedly beneficial to minimize the amount of scatter included in the data in the first place.

II.5.2 Benefits of Depth of Interaction

When imaging with pinhole collimators, photons can pass through the pinhole at a variety of angles; the more oblique the angle at which the photon enters the pinhole and subsequently the detector, the more uncertainty there is in the position of interaction of the gamma ray in the detector. This effect, known as parallax error or DOI effect, leads to the blurring of images near the edge of the pinhole's FOV and is demonstrated in Figure 13. The photon may interact in the detector anywhere along the line of response, which at oblique angles as seen in Figure 13 (c), causes counts to be smeared across the detector and blur the point source projection. The visualization of this effect is seen in Figure 13 (b) and (d), with (b) showing an on-axis projection that has no DOI effects present and (d) showing a smeared projection of an off-axis source due to DOI effects.

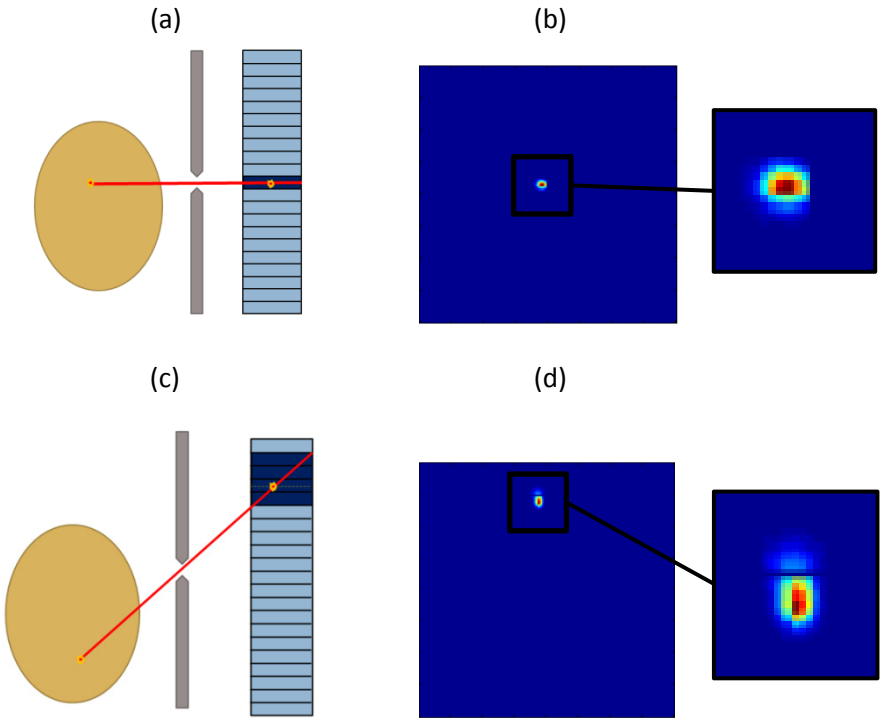

Figure 13: Demonstration of DOI effects where (a) shows how a photon emitted at a 0°angle of incidence to the pinhole has no uncertainty as to which detector element the photon could interact in, with (b) showing a corresponding pinhole projection image collected with a point source on-axis. Next, (c) shows that when a photon with a larger angle of incidence interacts in the detector there are multiple detector positions (dark blue) in which the gamma ray could deposit its energy and (d) is a projection image collected with a point source off-axis. The DOI effect can be seen in (d) as the smearing of the projection data is obvious.

Although different groups have investigated methods to overcome DOI effects in PET by including additional depth-positioning information (Miyaoka, Lewellen et al. 1998; Dokhale, Silverman et al. 2006), less work has been done with SPECT as standard detectors do not easily allow for depth information to be determined. If a SPECT detector had a mechanism to allow for estimation of the depth at which a photon interacted, then a better estimation of the trajectory of the incident photon, and subsequently its origin in object-space would be possible. This potential improvement is illustrated in Figure 14.

Some research groups have investigated how much of an effect implementing DOI estimation schemes would have on overall SPECT image quality in small-animal SPECT, but these have been limited to simulation studies. One group used an analytical model of DOI to create projection data that simulated the acquisition of point sources at different viewpoints relative to a pinhole (Hwang, Iwata et al. 2001). The resulting projections were reconstructed and FWHM

values of the point sources were extracted to determine the impact of the DOI effect on spatial resolution. These simulations were performed for 140 keV photons and two different detector configurations: a 6 mm thick cesium iodide (CsI) scintillator and a 10 mm thick HPGe. This simulation found that the image reconstruction algorithm contributed to a resolution loss of 0.32 – 0.63 mm FWHM in plane (normal to axis of rotation) and 0.21 – 0.42 mm FWHM out of plane of the detector (along the axis of rotation). For the scintillator detector, DOI effects contributed to a maximum resolution loss of 0.5 mm FHWM in plane and 0.3 mm FHWM out of plane. The HPGe detector had a resolution loss of 0.6 mm FWHM in plane and 0.5 mm FWHM out of plane due to the DOI effect. As expected due to HPGe's lower linear attenuation coefficient, and in this case a thicker detector, DOI effects are worse in HPGe than in the CsI scintillator. Although this study was only a simulation and did not investigate how including more depth information from a detector would impact the final image, it does suggest that there is some amount of spatial resolution improvement possible if the DOI effect was not present in images. As there are currently, to our knowledge, no studies that investigate DOI effects of pinhole SPECT that are not simulations, the HPGe SPECT system will allow for further investigation of the additional depth information.

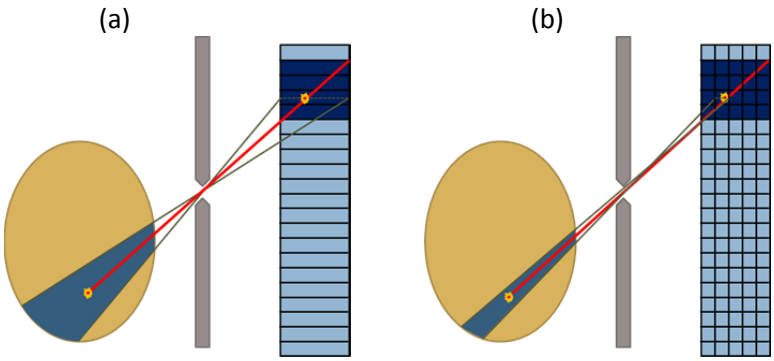

Figure 14: Benefit of DOI information: (a) shows the uncertainty in the back-projected position of the photon origin when no DOI information is present while (b) shows how this uncertainty is narrowed when the DOI information is applied to the back projection.

CHAPTER III

HPGE DETECTOR CHARACTERIZATION

III.1 Other System Configurations

Original germanium detectors required liquid nitrogen coolers that limited the ability to develop compact systems. An example of one germanium detector connected to a tank of liquid nitrogen can be seen in Figure 15(a). The bulk of the system's volume is clearly the tank for the liquid nitrogen. When the liquid nitrogen tank is replaced with a mechanical cooler, such as in Figure 15(b), the detectors become small enough to mount on rotating gantries typically used for SPECT imaging. The small size also allows for multiple detectors to be placed around the subject being imaged, increasing the overall system's sensitivity.

This project first investigated the feasibility of using HPGe for SPECT imaging by characterizing properties relevant to small-animal imaging on the NP3 system (PHDs Co), as seen in Figure 15(c). This system's design closely followed older system models as the mechanical cooler was placed directly below the detector, which was where the liquid nitrogen tank previously connected to the detector. The results of this work have been published (Johnson, Campbell et al. 2011), and as the main system used for this project, MI4.1 (Figure 15(d)), has several key differences from this original system, a characterization of the MI4.1 was performed and those results are discussed in the following sections of this chapter. It can be seen from the system photos that the physical space the systems require has decreased; additionally most of the system controls are now integrated into software. PHDs Co. has recently developed a next-generation detector that may be useful in future work, and can be seen in Figure 15(e). The cooler and processing electronics have been concealed inside a case, and an apparatus at the font of the system allows for attaching a pinhole or parallel-hole collimator.

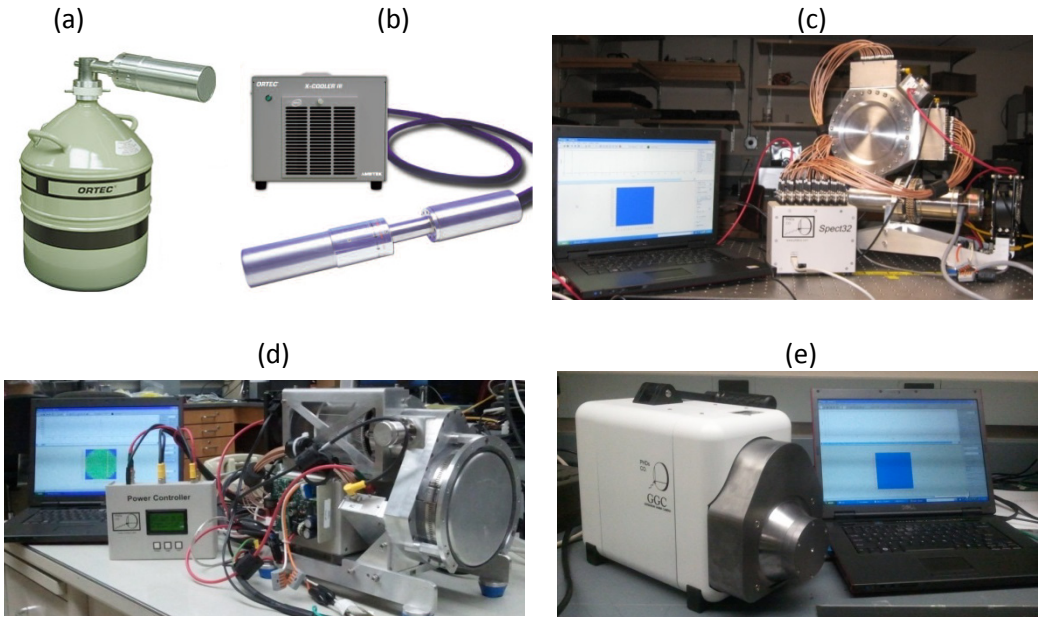

Figure 15: Photographs of various HPGe systems: (a) shows a detector connected to a liquid nitrogen dewar for cooling, (b) shows a similar system with the dewar replaced with a mechanical cooler, (c) shows the NP3 system which was used to first characterize properties relevant to small-animal imaging, (d) shows MI4.1 which is the system used for this project and (e) shows PHDs Co.'s newest system, the GGC.

III.2 Current System Configuration

This project utilizes MI4.1, a mechanically-cooled HPGe detector manufactured by PHDs Co. (Knoxville, TN, USA). This specially-designed DSSD was fabricated from a germanium crystal 90 mm in diameter and 10 mm thick and consists of orthogonal sets of 16 strips on each side that are 4.75-mm wide with a 5-mm strip pitch and has a total active area of 55.1 cm^2. The system is similar to the NP3 system characterized in (Johnson, Campbell et al. 2011) with the exception of three changes: the gap between strips has been reduced from 0.5 mm to 0.25 mm to help increase detection efficiency, the mechanical cooler and signal processing electronics have been reconfigured and relocated to facilitate easier mounting of the system on a rotating gantry, and the face of the detector has been moved to be ~6 mm away from the entrance window (as opposed to 2.9 cm) to allow for additional magnification options when a pinhole is utilized. Figure 16 shows the MI4.1 detector system and the germanium detector inside of the system.

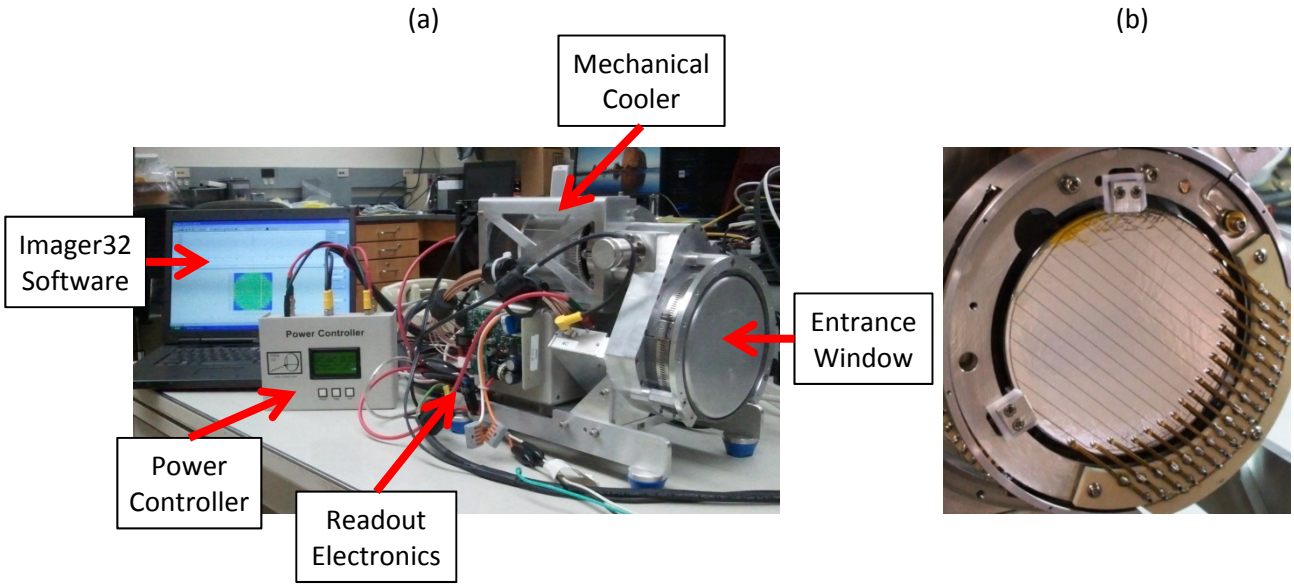

Figure 16: Photographs of the HPGe DSSD system MI4.1, showing (a) laptop with Imager32 software, power controller, readout electronics, the mechanical cooler and the DSSD itself, and (b) a close-up image of the DSSD inside the system with the entrance window cover removed.

The system is mechanically cooled to approximately 60 K and uses FPGA-based filtering and signal processing capable of recording approximately 450,000 cps. The Imager32 software included with the system provides sub-strip position estimation that is based on the transient signals induced on both neighboring strips to the charge-collecting strip. To do this, a flood illumination is acquired and for each interaction the difference between the neighboring transient signals is normalized by the signal amplitude on the charge collecting strip, giving a difference-ratio. A histogram of these difference-ratios is made for each strip and divided into nine groups containing an equal number of counts. The boundaries of these nine groups are subsequently used for assigning new events into 0.53 mm × 0.53 mm pixels. Similar methods have been used previously with other germanium strip detectors (Burks, Jordan et al. 2004). This system also provides an estimate of the depth of interaction based on the difference between the measured rise times of the signals collected on the anode and cathode (Wulf, Ampe et al. 2002).

Although a wide variety of detector properties could be investigated, this chapter presents detector properties that are of interest for a small-animal SPECT system, including: energy resolution, detection efficiency, spatial resolution, scatter rejection, detector uniformity, and depth of interaction capabilities.

III.3 Energy Resolution

To demonstrate this system's energy resolution, we acquired a flood image with four different radionuclides present: ^{99m}Tc, ^{123}I, ^{111}In, and ^{57}Co. Sources were placed in front of the detector until each radionuclide's main photopeak reached at least 400,000 counts. A Gaussian fit was used to determine the FWHM of each radionuclide's photopeak. Also, to avoid the potentially confounding effect of background due to down-scattering of higher energy photons, a separate acquisition with only ^{99m}Tc was performed. The energy spectrum resulting from the multi-radionuclide scan is shown in Figure 17. FWHM values for 122, 140, 159, 171, and 245 keV photopeaks were determined to be 1.07%, 0.93%, 0.85%, 0.81%, and 0.60%, respectively. The flood scan with only ^{99m}Tc was found to have a FWHM of 0.92% at 140 keV. This excellent energy resolution is clearly demonstrated by the ability to distinguish between the 136 keV ^{57}Co secondary peak and the 140 keV ^{99m}Tc peak. The detector does exhibit some energy resolution variation across the detector as well as across pixels within an individual strip-intersection region, ranging between 0.64% and 1.33% FWHM at 140 keV for the ^{99m}Tc only acquisition.

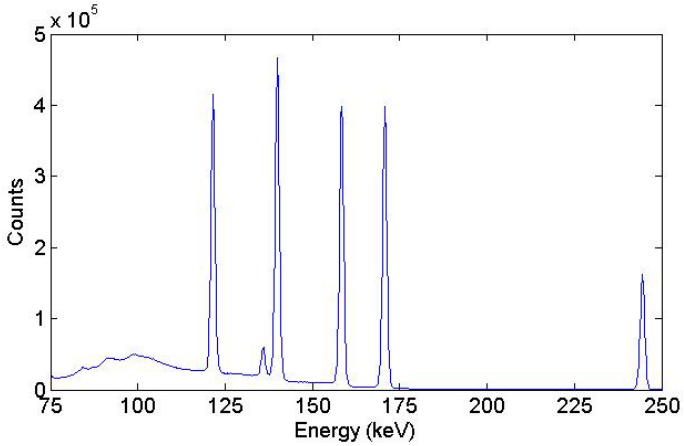

Figure 17: A multi-radionuclide energy spectrum including ^{57}Co (122 and 136 keV), ^{99m}Tc (140 keV), ^{123}I (159 kev), and ^{111}In (171 and 245 keV) is shown. The excellent energy resolution allows one to clearly distinguish between even the closest (136 and 140 keV) photopeaks.

III.4 Detection Efficiency

An ideal system would detect all photons emitted from a source that fall within the solid angle of the detector. But in reality there are limitations to the percentage of photons incident on the detector that interact and are

subsequently recorded. One such limitation arises from the emission energy of the radionuclide being imaged, which determines the probability of whether a full photoelectric absorption or a partial energy deposition from Compton scattering occurs. Additional losses can occur due to incomplete charge collection, charge sharing between strips, or inefficiencies in the signal processing.

To determine the detection efficiency experimentally, the detector was flood-illuminated with a 2.33 MBq ^{57}Co source positioned 40 cm from the detector's entrance window for one hour. Intrinsic efficiency was calculated using:

$$\varepsilon = \frac{N4\pi}{S\Omega},$$

Equation 13

where *N* is the number of counts recorded within a ±3 keV window about 122 keV, *S* is the number of emitted photons, and Ω is the solid angle, defined as:

$$\Omega = \frac{A}{d^2},$$

Equation 14

where *A* is the active area of the detector and *d* is the distance from the source to the detector.

Simulations of photon absorption were performed by fellow student Desmond Campbell to estimate the upper limit for the detector's efficiency. Monte Carlo N-Particle version 5 (MCNP5) was used to simulate the same flood-illumination scan described above. A monolithic slab of germanium with the same area as the actual detector was illuminated by a 122 keV point source 50 cm from the detector surface. 10^6 simulated photons were emitted within a cone that matched the solid angle subtended by the detector to minimize computation time. The simulation did not model detector effects such as energy resolution or spatial response. The upper limit of detection efficiency was estimated by summing the number of fully absorbed 122 keV photons as determined from the event histories, and dividing by the total number of incident photons on the detector.

Using Equation 13 and Equation 14 detection efficiency at 122 keV was measured to be 55.4%. The simulated efficiency for the monolithic germanium was 66.1%. Because a monolithic detector was simulated, it is expected that

the main difference between the simulated and measured values arise primarily due to charge sharing between strips and displaced energy deposition from Compton scattering. If it is assumed that no events are recorded for photons that interact within the gaps between strips, then the expected efficiency is reduced to 59.7%. The simulation also indicated that up to 30.6% of events that deposit their full 122 keV energy in the detector volume Compton scatter at least once, and at least some of these events would be expected to deposit energy in locations with sufficient separation as to be collected on more than one strip on at least one side of the detector. As current event processing registers only events in which charge is collected on a single strip on each detector side, such displaced Compton scatter events would not be included in the measured efficiency. Given these differences, the simulation and experimental results are in reasonable agreement.

III.5 Spatial Resolution

To estimate the intrinsic spatial resolution of this system we used a 2.54 cm x 2.54 cm x 2.54 cm tungsten collimator with a 200-µm square opening to create a finely collimated beam source. An ostalloy 2.54 cm x 2.54 cm x 6.35 cm block with a long bore was manufactured to hold a capillary tube flush to the key-hole aperture. Approximately 2035 MBq of ^{99m}Tc was drawn into a 75-mm long capillary (1.1-mm inner diameter) tube and placed into the ostalloy block. The source assembly was then placed flush with the detector entrance window and translated in both the x and y dimension until the projection was centered over a single detector pixel. Data were acquired for 2 hours and line profiles through the resulting distribution were fitted to Gaussian curves in both the x and y dimensions to determine the FWHM.

The resulting point source projection and the corresponding Gaussian fit in both the x and y directions are shown in Figure 18. FWHM values for the x and y directions were estimated to be 1.45 mm and 0.99 mm, respectively. One potential possibility for the discrepancy between the x-axis and y-axis resolution is that the point source was centered evenly over a pixel in the y direction but was not centered well over the pixels in the x-direction, as physically moving the collimated source less than half of one mm is problematic. Another potential for the difference is that this

discrepancy is related to the double-sided strip nature of the detector. The signals collected on the front side of the detector determine the sub-strip interpolation estimation for the y-axis, while the signals on the back side of the detector determine the x-direction sub-strip estimation. Photons that interact in the front of the detector, which is majority of counts in this case, create electron-hole pairs toward the front of the detector, where there is subsequently little travel-distance to the front side of the detector. But the charge-cloud traveling to the back-side of the detector, where the X position is estimated, generally has a longer path, giving time for the charge cloud to have more lateral diffusion than when traveling to the front-side of the detector. This additional diffusion could lead to differences in ability estimate the sub-strip position from the front (y-axis) and back (x-axis) of the detector, and subsequently the spatial resolution.

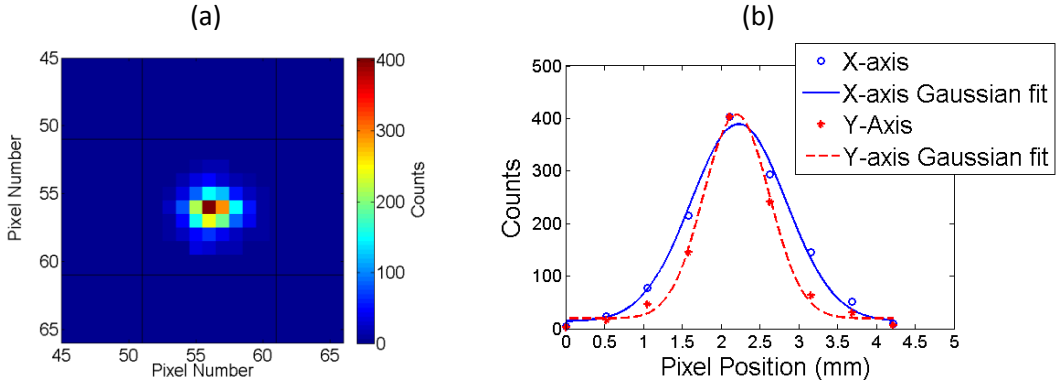

Figure 18: Spatial resolution estimation results showing the projection image of a collimated beam centered over a single pixel (a) with black lines indicating the location of gaps. Line profiles in the x and y direction through the highest intensity pixel can be seen in (b) along with the Gaussian fits, which yielded FWHM estimates of 1.45 mm and 0.99 mm for the x and y dimensions, respectively.

III.6 Scatter Rejection

Image resolution can be degraded by scattered photons that fall within the designated energy window. The excellent energy resolution of this system allows for a narrow energy window to be used, lessening the deleterious effects of scatter. To investigate this, we acquired two separate pinhole projection images with a 3.7 MBq ^{57}Co source placed 10 cm from the entrance window and 4 cm from a 1-mm-diameter pinhole with a 70-degree opening angle. Each scan was acquired for 1.5 hours, one with and one without a water phantom present. The configuration of the scan with the water phantom is illustrated in Figure 19. The energy window for inclusion in the image was ±3 keV about 122 keV.

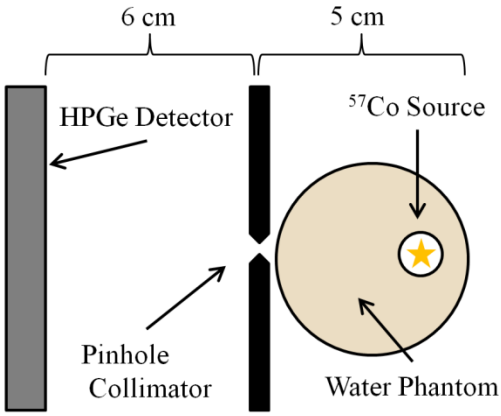

Figure 19: The scatter rejection experimental setup showing the detector, pinhole and water phantom arrangement. Data were acquired with and without the water phantom present, with the source remaining in the same location for both scans.

Figure 20 shows the (a) pulse-height spectra of the source in air (red line) and the source in the water phantom (blue line). The source in water clearly shows an increase in scatter slightly below the 122 keV emission energy. The chosen energy window (black lines in Figure 20 (a)), clearly limit the number of scattered photons present in the projection image. Direct assessment of line profiles taken from the projections with and without the water phantom present show no discernible visual differences, as can be seen in Figure 20 (b). Line profiles were subsequently fitted with Gaussians to probe for differences in width. These fits gave a FWHM and a full width tenth maximum (FWTM) of the source in air of 2.416 mm (4.403 mm) and the source with water phantom of 2.429 mm (4.428 mm). There was essentially no change in either the FWHM or FWTM even though there was a 35% decrease in counts due to the attenuation with the water phantom present.

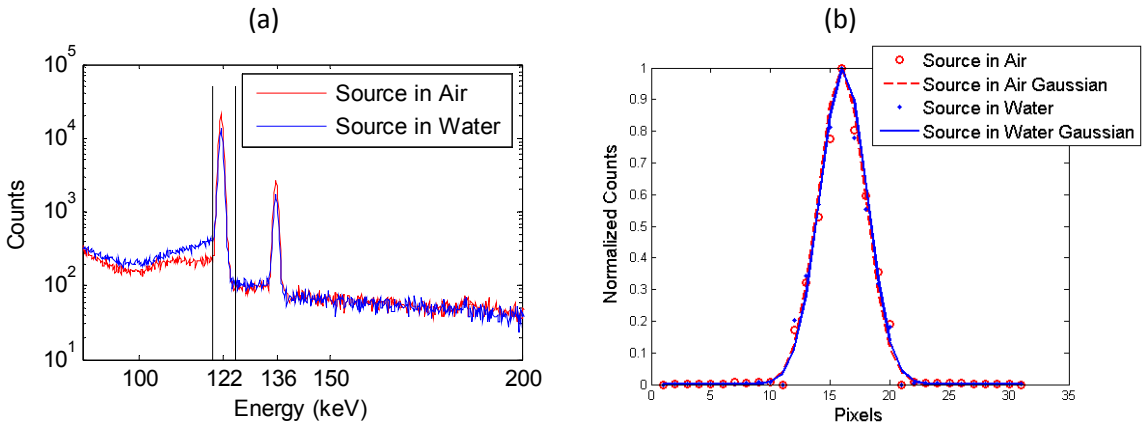

Figure 20: Results of the scatter rejection experiment with (a) showing log-scale pulse-height spectra for both the source in air and the source inside the water phantom acquisition. The black lines indicate the accepted energy window. (b) shows the normalized line profiles from the projection data of the source in air and in the water phantom, along with their respective Gaussian fits. There is no significant degradation of the FWHM or FWTM of the point source projection with scattering medium relative to without the scatter medium present.

III.7 Detector Uniformity

The detector uniformity was determined by following the NEMA 2007 standards for gamma cameras (NEMA 2007) as closely as possible as to allow for a standard comparison to other commercially available systems. Two 12-hour flood scans were acquired with a 3.7 MBq ^{57}Co source placed approximately 30 cm from the face of the detector. An energy window of 122 keV ± 3 keV was used. One flood image was used to create a normalization file that was subsequently applied to the second image. Gaps were removed from the images and integral and differential uniformities were calculated according to (NEMA 2007) for both scans for the useful field of view (UFOV) and the central field of view (CFOV). The integral and differential uniformity are both determined by the same formula,

$$Uniformity = 100 \times \frac{(max - min)}{(max + min)}$$

Equation 15

but they vary over the region of the data on which they are applied. The Integral Uniformity is applied over the entire FOV, while the Differential Uniformity is determined in both row and column directions and uses the *max* and *min* values between any five contiguous pixels. NEMA defines the UFOV as the area of the detector that is used for imaging gamma rays and x-rays that will be supplied by the manufacturer.

As the MI4.1 system is unique and the first of its kind from the manufacturer, its UFOV was not specifically defined. Therefore, we defined the UFOV to only include regions in which both charge-collecting strips (front and back) had neighboring strips on both sides, as the sub-strip position estimation scheme is not as reliable when only a single neighbor is present. The CFOV was defined by the NEMA standard as the central 75% of the UFOV. Determining both uniformities then gives perspective on artifacts from the edge of the FOV, which are potentially present in the CFOV, but likely excluded in the UFOV values. Additionally, when possible the subject being imaged is placed in the center of the FOV, and therefore having a quantifiable value in the central region gives perspective into how non-uniformities may influence image quality.

Uniformity was calculated at both the level of intersecting strips (strip data) and the level of the 0.53 mm × 0.53 mm pixels to which sub-strip interaction positions are estimated (pixel data). Acquisitions consisted of an average of approximately 5,300 counts per pixel and 435,000 counts per strip intersection. NEMA standards require a minimum of 10,000 counts to be collected in the center pixel of the image, and that pixels have a linear dimensions of 6.4 mm ± 30%. As these standards are intended for clinical systems, and therefore have much larger pixel dimensions than the MI4.1 system, the standard pixel for the MI4.1 system was used with a lower number of counts than suggested to limit the total scan time for the pixel-data, but have significantly more counts than suggested for the strip data with the 4.75 mm × 4.75 mm pixel size.

Uniformity was calculated for the corrected and uncorrected flood scans at both the pixel level and strip level for UFOV and CFOV, and the results are shown in Table 3. For the corrected flood, the results at strip level are well below 1%, while the results at pixel level are between 2% and 3%. The values of the UFOV and CFOV at strip level are identical because the regions are identical. The flood-corrected flood, with gaps and the entire FOV shown, can be seen in Figure 21.

Table 3: Uniformity measurement results

	Uncorrected Flood				Corrected Flood			
	Pixel Data		Strip Data		Pixel Data		Strip Data	
	UFOV	CFOV	UFOV	CFOV	UFOV	CFOV	UFOV	CFOV
Integral	45.54%	43.41%	2.19%	2.19%	3.16%	2.98%	0.20%	0.20%
Differential Row	31.73%	31.66%	1.43%	1.43%	2.60%	1.99%	0.18%	0.18%
Differential Column	30.37%	29.11%	1.77%	1.77%	2.31%	2.15%	0.15%	0.15%

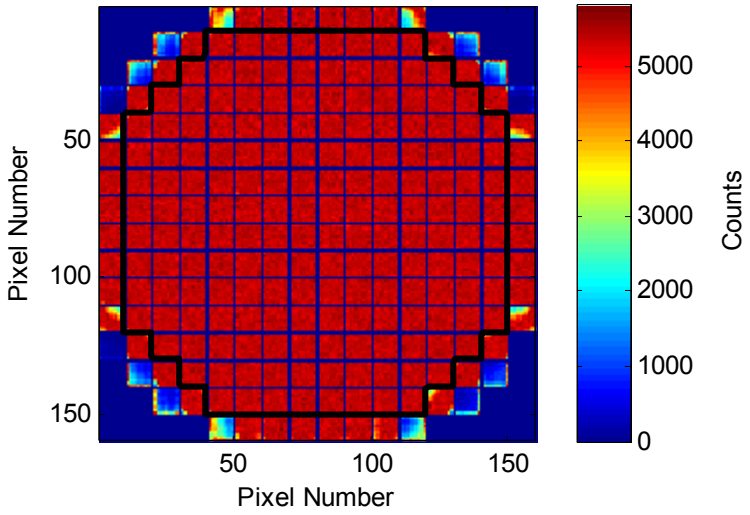

Figure 21: The ^{57}Co flood-corrected flood projection used to determine the system uniformity is shown. This projection shows the entire FOV of the detector, with the UFOV outlined in black. The lines with zero counts indicate the position of the gaps between strips.

III.8 Depth of Interaction

The Imager32 software provides estimates of the depth of interaction by dividing interactions into 1-mm-thick depth bins based on the 50% CFD time differences between the collecting strips on the front and back of the detector. We attached a 1-mm-diameter knife-edge pinhole collimator 6 cm from the detector's entrance window and a 3.7 MBq ^{57}Co source was placed directly in front of the pinhole approximately 7.25 cm away. A one-hour projection image was acquired, and the source then was moved laterally 3.5 cm off-axis (approximately 26 degrees) from the pinhole where a second projection image was acquired for 3 hours. Projection images, shown in Figure 22, are presented as a sum of all depths showing x and y position as well as depth versus lateral position to illustrate depth-of-interaction estimation capabilities.

The on-axis depth projection is vertical as expected, while the maximum intensity of each off-axis depth is shifted. In both the on- and off-axis cases, increasing depth results in an exponential decrease in counts (except for the transition from the first to second depth). Depth assignment is based on a linear model of the variation in charge-collection times with depth. This model can lead to some events being assigned to incorrect depths for interactions occurring close to one electrode, as seen in change of the number of counts between the first and second depths.

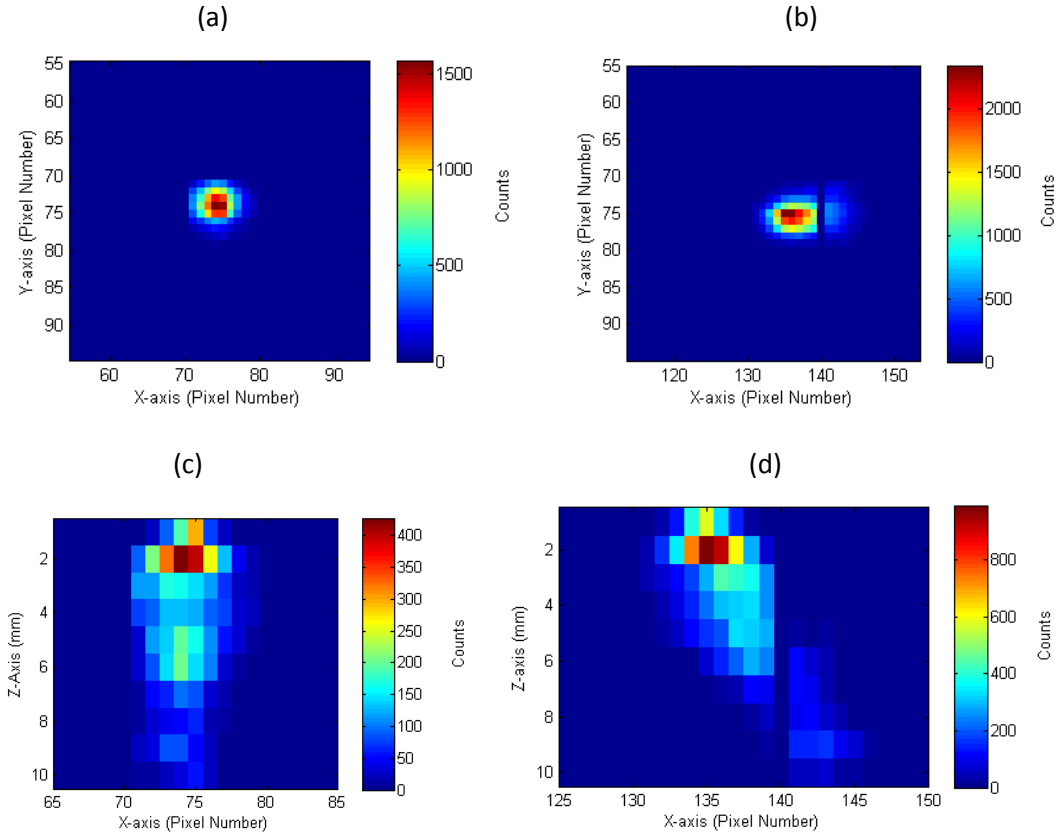

Figure 22: Demonstration of depth-of-interaction estimation capabilities. (a) and (b) show the projection images of the on-axis and off-axis projections, respectively. The off-axis projection is blurred due to parallax error. (c) and (d) show depth versus lateral position for the off-axis and on-axis projections, respectively.

III.9 Discussion

This study investigates our system's performance on several detector properties relevant to biomedical imaging. A comparison of the system properties of the system described above (MI4.1) and the previously characterized system (NP3) is shown in Table 4. The excellent energy resolution of our system is on par with other similar HPGe systems,

including our previously characterized system (Johnson, Campbell et al. 2011), which had 0.96% compared to this system's 0.92% at 140 keV.

Table 4: NP3 and MI4.2 system properties

Detector Property	HPGe NP3	HPGe MI4.1
Gap Size	0.5 mm	0.25 mm
Detector to Entrance Window Distance	6 mm	2.9 cm
Energy Resolution	0.96% at 140 keV	0.92% at 140 keV
Intrinsic Efficiency	43.3% at 122 keV	55.4% at 122 keV
Spatial Resolution	~1.5 mm	~1.5 mm
DOI Estimation	1 mm depths	1 mm depths
Scatter Rejection	Minimal SR degradation	Minimal SR degradation
Detector Uniformity	<1% with correction at strip level	<1% with correction at strip level

We estimate the intrinsic spatial resolution of this system to be 1.45 mm and 0.99 mm in the x and y directions, respectively. Given the difference in resolution between the x and y directions, in addition to the presence of the gaps in the detector, additional investigation into the spatial dependence of the spatial resolution may be warranted in future work. Spatial resolution has the potential to be improved upon in the future by implementing a more robust sub-strip positioning algorithm. The current method is based on the difference in the fast transient signals induced on nearest neighbor strips, but this binning method is based on flood data with an assumed uniform distribution. Other methods of signal processing involving maximum-likelihood estimation (Barrett, Hunter et al. 2009) or pulse-shape analysis (Blair, Beckedahl et al. 1999) may yield improvements in the spatial resolution in all three dimensions. A typical NaI(Tl) scintillator used as a SPECT detector has an intrinsic spatial resolution of ~3 mm (Kupinski and Barrett 2005), but because these detectors can be made with a large surface area, higher-resolution systems are achieved by having a larger magnification factor. CZT and CdTe detectors range in their intrinsic spatial resolution that is dependent on the physical pixel readout structure that the detector is manufactured with. A better comparison of spatial resolution capabilities is at a system-level, as this determined in small-animal SPECT by the system configuration, including radius of rotation, focal length, and pinhole diameter. A system-level comparison is discussed in IV.7.1.

Although uniformity at a pixel level is slightly better in this system than in the NP3 system (Johnson, Campbell et al. 2011), further work still needs to be done to determine if better uniformity is possible. Uniformity requirements are

dependent on both the system being used and the imaging task. One clinical system, the Siemens MultiSPECT 3, an older scintillator-based system, requires integral uniformity in the CFOV to be lower than 3.5% or recalibration must be done (Kuikka, Tenhunen-Eskelinen et al. 1993). A newer CZT system, intended for use in clinical scintimammography, reported an integral uniformity in the UFOV to be 2-3% (Mueller, O'Connor et al. 2003). On the other hand, a newly developed preclinical SPECT system using a CdTe detector was found to have integral and differential uniformities of 28.5% and 26.3%, respectively (Ogawa, Ohmura et al. 2009). While the present system exhibits uniformity on par with these systems, further improvements in pixel-level uniformity are potentially possible if the previously discussed more robust signal processing method for sub-strip position estimation are implemented.

The intrinsic efficiency of this system (55.4%) is an improvement over the 44.3% efficiency measured with the NP3 system (Johnson, Campbell et al. 2011). This increase in efficiency is attributable to the size of the gap between strips being half that of the previous detector. Although decreasing the gap size is one way to increase the efficiency, other possible ways to improve this in the future include recovering events that occur in the gaps and, consequently, suffer from incomplete charge collection and/or charge sharing, and to process and include events that Compton scatter and subsequently deposit energy on multiple strips on the same detector side. Another group has investigated incomplete charge collection and subsequently developed a method to correct for it, leading to an increase in photopeak counts by 15% on the anode and 5% on the cathode side for a similar HPGe DSSD system (Hayward and Wehe 2008; Hayward and Wehe 2008). Additional improvements in detection efficiency could be made by including Compton scatter events in which charge is collected on multiple strips on one detector side. This type of processing and event reconstruction has already been implemented in an HPGe system used as a Compton camera using pulse-shape analysis (Vetter, Burks et al. 2004). Although there are some potential methods for improvement, to give perspective, a 2-mm thick CZT detector that is used in the small-animal SemiSPECT system has an efficiency of approximately 40% at 140 keV (Kim, Furenlid et al. 2006).

The most noteworthy feature of this detector is its outstanding energy resolution, which is less than 1% at 140 keV, especially when compared to other detectors used for small-animal SPECT such as NaI(Tl) with ~10% at 140 keV,

and CZT with ~6% at 140 keV (Kupinski and Barrett 2005). It is clear from the multi-radionuclide spectrum shown in Figure 17 that this energy resolution will enable easy separation of photopeaks in a multi-radionuclide SPECT acquisition. The ability to set a narrow energy window about the desired photopeak will limit the number of down-scattered photons of higher energy in the image. Also, for single radionuclide acquisitions, a narrow energy window limits the number of photons scattered from the primary photopeak that still manage to fall within the set energy window. The demonstrated depth-of-interaction estimation capabilities will also mitigate blurring from parallax when pinhole collimation is utilized when depth information is incorporated into reconstruction.

CHAPTER IV

DEVELOPMENT AND INITIAL TESTING OF A SMALL-ANIMAL HPGE SPECT-CT SYSTEM

IV.1 Introduction

Initial work in characterizing the HPGe detector, as discussed in Chapter III, demonstrated its potential for use in small-animal imaging applications. This chapter will describe the steps taken to integrate the detector into a SPECT-CT system. Initial system design and specifications will be presented, followed by the description of the mounting process onto a small-animal CT system. Next, the system calibration, system matrix determination, and reconstruction methods are discussed. Phantom images, including a dual isotope example, are shown to demonstrate the system's image quality. Finally the effects of the detector gaps on image quality are addressed.

IV.2 Collimator Design

The HPGe detector enclosure was designed with a steel mounting ring around the entrance window to allow for placement of a pinhole aperture. As this system is intended to be used in a variety of small-animal imaging applications, the collimator should allow for imaging at varying magnification, which gives the flexibility to acquire images with different fields-of-view and at different resolutions. The collimator design should minimize the size of the pinhole plate to reduce material costs and also allow for additional pinhole plates with different numbers of pinholes or different pinhole diameters to be used in the future. Although the majority of small-animal imaging systems utilize multi-pinhole collimators to increase system sensitivity, we chose to first utilize a single-pinhole collimator to demonstrate proof-of-concept.

To begin the system design, first the desired image field of view (FOV_{OBJ}) was chosen to be 3.5 cm, so that mouse-sized objects would fit in the FOV. Given the limiting factor of the surface area of our detector (8 cm diameter), this limited the magnification factor (M) of the system to 2. This subsequently determined the magnified FOV on the detector (FOV_M) as 7 cm. The intrinsic spatial resolution (R_d) of the HPGe detector was determined in section III.5 to be

~1.5 mm, and the overall desired system resolution (R_{TOT}) was chosen to be 1.5 mm. With these parameters fixed, the tradeoff between the system sensitivity, the pinhole size, and the pinhole opening angle can then be explored and set to an appropriate value.

Calculating system sensitivity or resolution using only the pinhole diameter can lead to inaccurate estimates as penetration through the pinhole is not included. More accurate calculations utilize the resolution-equivalent or sensitivity-equivalent pinhole diameters, which are defined as the diameter of an ideal pinhole (one with no penetration) with the same resolution (or sensitivity) as the actual pinhole (Accorsi and Metzler 2004). With this in mind, an estimate of the resolution-equivalent diameter of the pinhole (d_{re}) was determined using a modified version of Equation 2, where the intermediate R_g is the geometric resolution:

$$R_g = \sqrt{{R_{TOT}}^2 - \left(\frac{R_d}{M}\right)^2}$$

Equation 16

and from Equation 1:

$$d_{re} = \frac{R_g}{1 + \frac{1}{M}} \quad .$$

Equation 17

When the above parameters are used, R_g is 1.3 mm, giving a desired d_{re} of 0.87 mm. Because d_{re} is dependent on the location of the object in image space, the on-axis form of the equation was used (Equation 18) in order to minimize the number of unknown variables, but an off-axis version of the d_{re} equation is derived in (Accorsi and Metzler 2004). The resolution-equivalent pinhole diameter can then be used in conjunction with the pinhole material density (μ = 1.876 cm^2/g for tungsten) and the full-opening angle α to estimate the actual pinhole diameter:

$$d = \frac{d_{re}}{1 + \frac{ln(2)}{\mu} tan\left(\frac{\propto}{2}\right)} \quad .$$

Equation 18

As there are now two unknown pinhole properties in this equation, a simple solution is not available unless one of the two values is fixed; therefore, the physical pinhole diameter was fixed at 1 mm, as it is a commonly used sized for small-animal systems with modest resolution. Next, the effect of pinhole diameter and opening angle on sensitivity is determined, where the resolution-derived actual pinhole diameter (*d*) is used to determine the sensitivity-equivalent diameter (d_{se}):

$$d_{se} = d\sqrt{1 + \frac{2}{d}\cdot\frac{tan\left(\frac{\propto}{2}\right)}{\mu} + \frac{2}{d^2}\left(\frac{tan\left(\frac{\propto}{2}\right)}{\mu}\right)^2} \quad .$$

Equation 19

Finally, the sensitivity at a given location in image space (S_{Point}) is calculated using d_{se} in place of *d,* with *a* as the distance from the point in space to the pinhole, and with φ as the angle off-axis from pinhole. The highest sensitivity occurs when φ is 0, or directly on-axis with the pinhole, and as the object being imaged moves off-axis the $\cos^3$ falloff factor induces a loss in the sensitivity (Accorsi and Metzler 2004):

$$S_{Point} = \frac{{d_{se}}^2}{16a^2}cos^3(\varphi) \quad .$$

Equation 20

For a given opening angle, the sensitivity-equivalent diameter was calculated and used to determine the total sensitivity, while the resolution-equivalent diameter was calculated and then used to determine the total resolution using Equation 2. Results for a variety of opening angles are shown in Table 5. After considering the trade-off between on-axis sensitivity and total resolution, a 70^o full opening angle was chosen, which gives an approximate on-axis sensitivity of 2.44×10^{-3} at 3 cm from the pinhole.

Table 5: For d = 1 mm, calculated system resolution and sensitivity

Opening Angle (α)	R_{TOT} from d_{re} (cm)	S_{Point} from d_{se}
40°	0.1875	2.962E-04
50°	0.1898	6.681E-04
60°	0.1924	1.332E-03
70°	0.1953	2.439E-03
80°	0.1986	4.213E-03
90°	0.2026	6.989E-03
100°	0.2074	1.131E-02

After the pinhole parameters were chosen, the rest of the collimator design was developed. A cone-shaped aperture that extends outward is used to attach the collimator to the detector and allows a varied number of extenders to be attached to it, which provides magnification options. The chosen pinhole plate is then connected to the end of the extenders. This design allows for a single-pinhole HPGe-SPECT system to be used presently, and also allows for easy attachment of multi-pinhole plates for future projects. The design includes three extenders that are 1.5 cm thick to give magnifications of 1.5, 2, 2.5, and 3 (focal length of: 4.5, 6, 7.5, 9 cm). Models of the pinhole, cone-aperture mount and extenders were created using SolidWorks (Dassault Systèmes SolidWorks Corp, Waltham, MA), with the final configuration shown in Figure 23. Tungsten was chosen for the aperture material as it has a relatively high density (19.3 g/cm^3), which gives it a reasonable attenuation coefficient at relevant SPECT energies. The thickness of the aperture assembly is designed to image isotopes of up to 245 keV. This design was then given to Tungsten Heavy Powder, Inc. (San Diego, CA), who subsequently manufactured the part using a molded tungsten process. The final manufactured collimator is shown attached to the germanium system with one extender present in Figure 24.

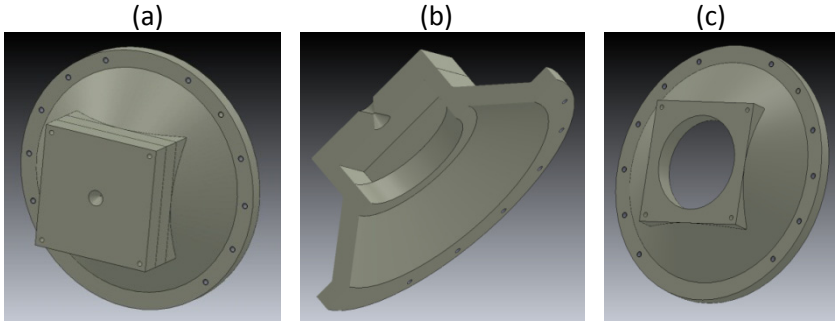

Figure 23: SolidWorks model of the system aperture showing the pinhole and one extender connected to the cone mounting plate (a, b) and a view of just the cone aperture (c).

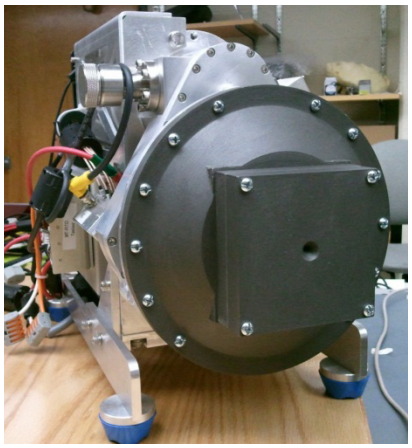

Figure 24: Final pinhole aperture mounted to the HPGe detector, showing the cone-aperture, one extender and the pinhole collimator.

IV.3 Mounting HPGe Camera to CT Gantry

In the planning phase of the SPECT-CT system, it was decided that the detector would be mounted onto a translation stage which would then be mounted to the microCAT II gantry. This translation stage allows for the detector to have a variable radius of rotation in addition to being able to move the SPECT camera out of the FOV of the CT. A 404XR Parker translation stage with an Animatics SmartMotor was chosen as the same stage type and motor are used in the MicroCAT II animal bed stages, which allowed for easier programming and stage control. A SmartMotor program was developed and uploaded to the motor, and MATLAB software was developed to communicate with it. A photograph of the un-mounted translation stage is shown in Figure 25. PHDs, the company that manufactured the detector also designed and built the support system to mount the detector and translation stage to the gantry, and came to Vanderbilt to help mount the detector on the gantry. Photographs of the MicroCAT II system before and after the HPGe system was mounted to the gantry are shown in Figure 26.

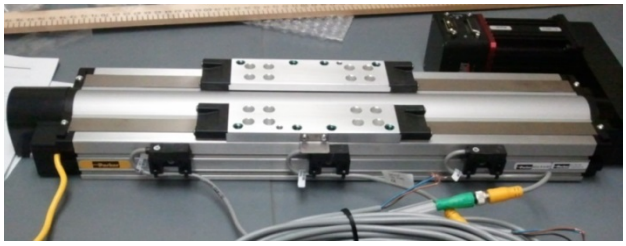

Figure 25: Photograph of the translation stage used to change the detector's ROR. The three black slides are limit switches used to control repeated stage positioning.

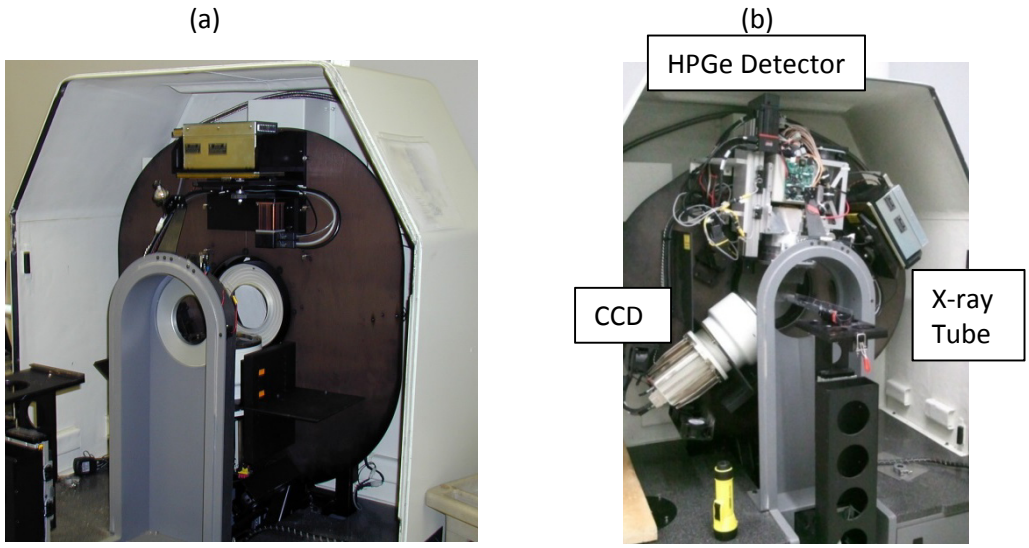

Figure 26: Photographs of before (a) and after (b) the HPGe system was mounted to the gantry of the microCAT II system.

After the system was mounted to the gantry, software was developed (with the help of fellow student Oleg Ovchinnikov) to control stage movement and data acquisition. For data acquisition, the Imager32 software included with the detector creates a named pipe and ports event data (x position, y position, z position and energy) across the pipe to which a MATLAB script is connected. The MATLAB program sends commands through the pipe to control the start and stop of data collection, and also saves the event data in a specified folder. The MATLAB program also connects to the MicroCAT II stages that move the animal bed height, animal bed depth, and rotate the gantry. The software requires an input file of the desired image collection sequence that includes the bed height, bed depth, gantry angle, and HPGe stage position at each collection point, and a collection time. A screenshot of this software interface is shown in Figure 27.

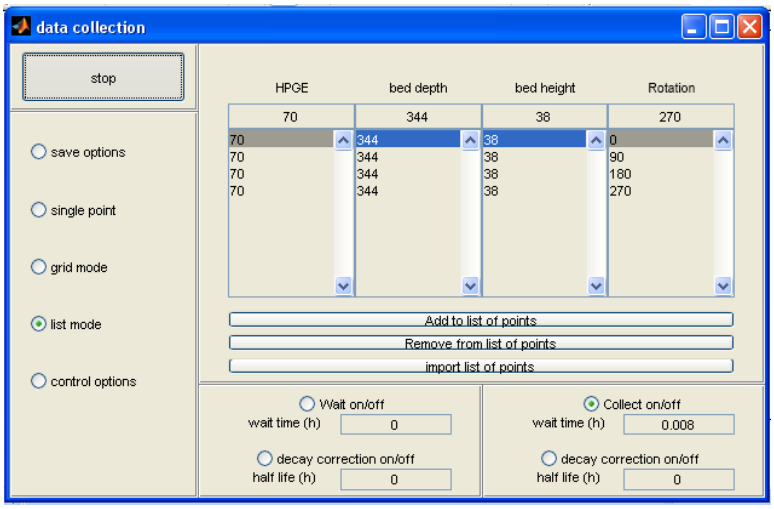

Figure 27: Screenshot of the MATLAB control panel of the image acquisition software that has input areas for the HPGe stage position (determines ROR), bed height, bed position, gantry angle, and acquisition time per projection.

IV.4 System Matrix and Image Reconstruction Methods

IV.4.1 General Methods

The system matrix to reconstruct images was determined using the analytically-derived method because it is better suited than the experimentally-determined system for detectors that move on a gantry. The method described in section II.2.3.1.2 by Beque et al. (Beque, Nuyts et al. 2005) was implemented in MATLAB. First, fellow student Oleg Ovchinnikov manufactured a 5-point calibration phantom, as described in the schematic in Figure 28. The dots in the figure represent small divots drilled into a piece of acrylic that can be filled with a radionuclide for imaging. Although it has been shown that for a single-pinhole system 3 points with known distances between them are sufficient to determine the calibration parameters (Beque, Nuyts et al. 2003), additional points were included in the phantom to give the opportunity to use the extra points for validation. The locations of the points in the phantom were based on (Beque, Nuyts et al. 2005), in which different positions of point sources relative to the axis of rotation were investigated, and they determined that for three point sources, results are more robust when the sources are distributed over the entire FOV. The geometric calibration procedure should be performed every time the pinhole collimator has been moved, if a

new radius of rotation is going to be used for imaging, or if a new pinhole collimator configuration (e.g. a different number of extenders or new pinhole collimator) is being used.

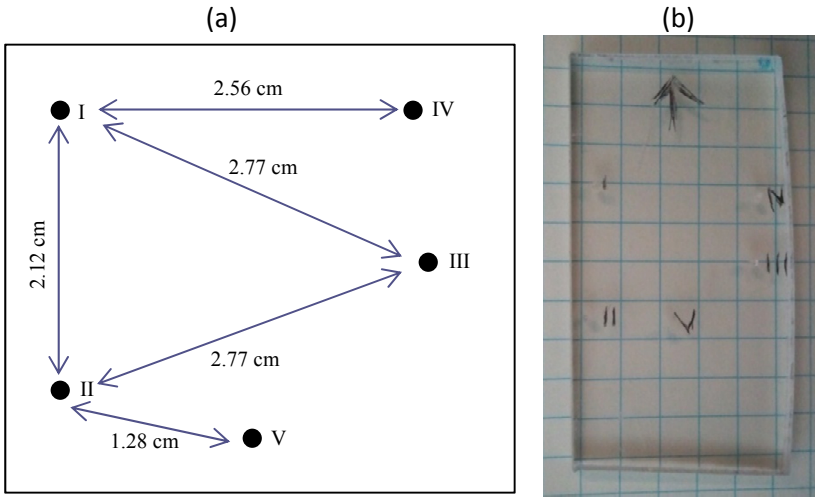

Figure 28: Schematic (a) and photograph (b) of the co-planar 5-point phantom used for calibration. Coordinates of the points (in cm) are (0,0), (0, 2.12), (2.56, 1.06), (2.56,0), and (1.28, 2.22), for I, II, III, IV, and V respectively.

The seven geometric parameters determined in a geometric calibration were described in detail in section II.2.3.1.2 and include the focal length f, the distance from the pinhole to axis of rotation d, the electronic shifts e_u and e_v, the mechanical offset m, the detector tilt φ, and the detector twist ψ. To determine these calibration parameters, the holes in the calibration phantom are filled with ^{99m}Tc and the phantom is placed on the animal bed and subsequently centered in the FOV of the HPGe detector face. The phantom is then imaged for a given period of time (generally between 30 seconds to several minutes depending on the activity in the phantom) at 64 projections spaced evenly over 360°. This results in projections with a maximum of five PSFs, one for each of the point sources in the phantom, but may have less PSFs included in subsequent processing as the point sources which overlap or fall outside or near the UFOV boundary of the detector are excluded. Each projection is masked for values above a threshold and the MATLAB strel function is used to determine a disk-shaped ROI for each non-overlapping PSF, which is subsequently used to determine the centroid position of the PSF. The centroid coordinates, the projection angle they were acquired at, and the known physical distances between the points in the phantom are then used as inputs into a least-squares fitting algorithm written in MATLAB to estimate the seven calibration parameters.

To test the calibration code and its repeatability, this procedure was repeated twice with the bed and the HPGe stage moved home and back to imaging position between scans. This protocol tests the repeatability of the HPGe translation stage positioning in addition to testing that geometric calibration results are being reasonably estimated compared to the parameters known from the system manufacturer and collimator design.

An example of a projection image of the five-point phantom is shown in Figure 29. The centroids of the five points in the phantom trace out ellipses in detector space as the detector is rotated around the phantom, and the ellipses for the first calibration measurements are shown in Figure 30, along with the resulting estimates of the centroid locations using the calibration parameters from the fit.

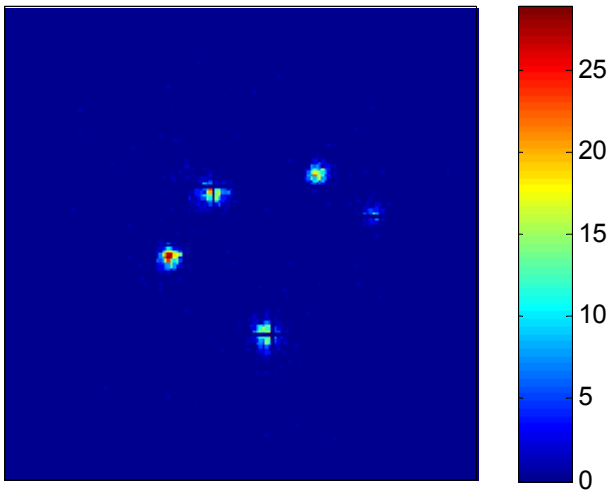

Figure 29: Example projection image of the 5-point calibration phantom.

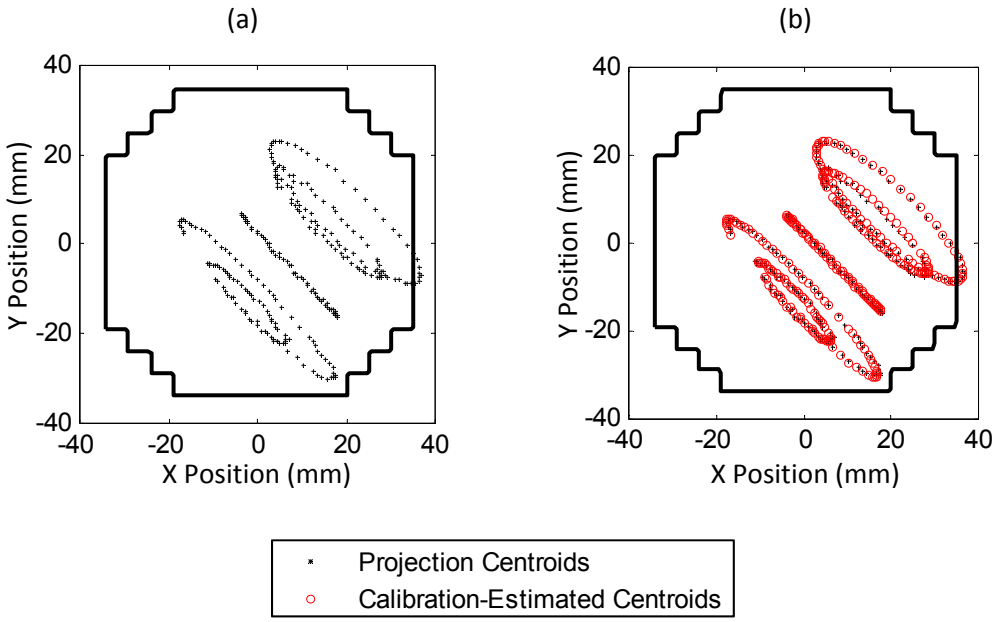

Figure 30: The centroids of the first calibration acquisition (a), and the estimated centroids (b) based on the distances between the calibration phantom, its location in image space, and the determined calibration parameters. The black outline indicates the UFOV of the detector as defined by the uniformity calculation in section II.7.

The results of these scans are shown in Table 6. The residual value provides a measure of the goodness of fit, and is the sum of the squared difference between the experimental input data and the resulting estimated data determined by the calibration parameters. The twist of the detector is approximately 314°, which is as expected due to the negative 45° orientation of the detector's strips relative to the imaging space.

The original system specifications from the manufacturer stated that there was a 6 mm gap between the detector entrance window and the front of the detector, and this value was used to determine the length of the aperture and extenders to give the desired focal length of 6 cm with one extender. As can be seen from the results, the focal length is slightly larger than anticipated, which may be due to the inaccurate estimate of the distance from the detector face to the entrance window or due to the ambiguity of the starting point of the focal length in the 1-cm thick detector.

Table 6: Geometric calibration results

	f (mm)	*m (mm)*	ψ (*rad*)	φ (*rad*)	e_u *(mm)*	e_v *(mm)*	*d (mm)*	Residual
Cal 1	67.71	6.26	5.49	6.26	-4.49	3.94	56.88	48.05
Cal 2	67.71	6.30	5.49	6.26	-4.47	4.11	56.92	75.76

Four of the five points on the phantom were used to determine the calibration, leaving one point to independently assess the error of the predicted centroid location to the experimentally determined centroid. In Figure 30, the fifth point that was not included in the calibration function is the smaller ellipse in the lower-left corner. The average position error, determined by the mean distance and standard deviation between the estimated and actual centroid was 0.68 ± 0.34 mm, with the maximum and minimum errors of the individual points being 1.15 and 0.023, respectively. This error is due to the error in determining the centroid of the point source projection, which is then propagated into the error of the calibration parameters themselves. Given that the detector's pixel size is 0.53 mm and that the spatial resolution of the detector is approximately 1 to 1.5 mm (SECTION II.5), these errors are within an acceptable range as the average error is only slightly larger than one pixel.

One concern with these results is the large value of *m*, or the offset of the pinhole axis from the center of image space. This parameter indicates that the detector and pinhole are not aimed at the center of object-space, which creates a much smaller FOV. Although the ROR was large in this example, the original ROR of the system was planned to be ∼3 cm, in preliminary studies (not shown) the phantoms imaged were too large to fit in the FOV and truncation artifacts severely degraded image quality. Because of this, a ROR of ∼4 cm was required in order to ensure that all phantom activity in experimental images (section IV.5) were in the detector's FOV. Future work with this system may require the system position to be altered such that the detector is better aimed toward the center of rotation.

An MLEM reconstruction algorithm was written in C++ based on code from Dr. Sepideh Shokouhi that was originally written for use with the SiliSPECT system. The reconstruction code uses the geometric calibration and an analytically derived system matrix that uses a central-ray method and is calculated on-the-fly. OSEM versions of the

reconstruction were also developed in order to decrease reconstruction time, but all reconstructions utilize the MLEM algorithm.

IV.4.2 Helical Acquisition Methods

Helical acquisitions involve moving the subject in the axial direction a small distance between each projection acquisition. The distance moved by the bed per full rotation of the camera, or the helical pitch, must be small enough to ensure that the object is fully sampled in order to avoid image artifacts. For most systems this is a matter of ensuring that a voxel in object-space remains in the FOV of the detector for a full orbit of the detector (Metzler, Greer et al. 2003). For the HPGe detector system, helical acquisition allows for more complete sampling in two different ways. The first common reason is to help extend the axial FOV that is limited with a single-pinhole collimator. The second benefit is to help compensate for lack of collected data in the gap regions of the detector. During stationary acquisitions, the gap regions of the detector are rotated around the object and are sensitive to the same regions of object-space, which leads to regular regions of object-space that are under-sampled. When helical sampling is implemented, the gaps are sensitive to different regions of object-space, essentially increasing the object sampling, which helps to increase image quality. A more thorough discussion of the effects of gaps on image quality is described in section IV.6. Due to the limited axial coverage of the single-pinhole aperture and due to the effects stemming from lack of data collected in the gaps of the detector, a helical acquisition and reconstruction method was implemented.

Before image acquisition, an additional geometric calibration was determined to account for the direction of the bed movement with respect to object-space. The original geometric calibration described in section IV.4.1 determines the relationship between object-space, detector space, and the pinhole location, but in helical acquisitions the bed translates a small step in the z-direction of its own coordinate plane, which may differ from the object-space coordinate system. In order to accurately correct for this movement in the reconstruction, the exact relationship between the bed's axis of movement and the object-space must be determined. To do this, the geometric parameter estimation method in the stationary acquisition is expanded. The same phantom acquisition is performed, except that instead of only acquiring at a single bed position, 64 projections at four separate bed positions are collected. The same calibration

estimate is performed on the four data sets, except that in this case the six nuisance parameters that describe the position of the calibration phantom in detector space are saved: t_x, t_y, t_z, ρ_1, ρ_2, ρ_3, where t and ρ represent the translations and rotations, respectively, of the calibration phantom with respect to the object-space origin. The results of the four data sets give very similar calibration parameters, as they are independent of the phantom position in object-space (assuming that enough points are in the FOV to give a reasonable amount of data for the least-squares algorithm to fit). The rotation nuisance parameters (ρ_1, ρ_2, ρ_3) should also be similar as the orientation of the phantom is not changed during acquisition. On the other hand, the translation values change depending on the phantom positioning and can be used to determine how the bed moves relative to object-space.

A MATLAB function was written that first uses the determined geometric calibration parameters to transform the bed movement coordinates, which in this case is simply the distance in millimeters the linear translation stages were directed to move between each phantom acquisition, into object-space for each of the four bed positions. Next, a rigid affine transformation matrix is estimated using a MATLAB function written by fellow student Thomas Pheiffer, which uses the method described by (Horn, Hilden et al. 1988). The function takes an input of the source positions (nuisance parameters), the translation stage positions, and the target positions, the object-space transformed positions and returns a transformation matrix that can then be used to transform the bed position into object-space coordinates.

The individual geometrical calibration results for each of the four bed positions in a typical helical calibration are shown in Table 7. Unlike the example calibration in section IV.4.1, all five points were used in the least-squares fitting process as different points move in and out of the FOV of the detector at different bed positions. The results show a good match between the different positions, but a single set was chosen based on the average of the middle two positions, as they contained the most PSFs in the FOV. The calibration code was then re-run for each bed position with the same standard 7 geometric calibration parameters in order to obtain the nuisance parameters at each bed position. These nuisance parameters, shown for each bed position in Table 8, are then used to determine the rigid affine transformation, which in this case gave a rotation vector for the z dimension of [0.0544, -0.0597, -0.9967], which is used

to transform the bed position into object-space position. This transformation matrix indicates that there is 6.84° between the object z-axis and the z-axis on which the bed moves.

Table 7: Results of a typical helical calibration scan at four bed positions

Bed Position (mm)	0	3.33	6.67	10.0
f (mm)	68.24	69.21	67.01	66.33
m (mm)	5.22	3.90	4.48	5.06
ψ (rad)	5.48	5.48	5.49	5.49
φ (rad)	6.27	6.26	6.28	6.28
e_u(mm)	-2.45	-0.20	-0.39	-1.61
e_v(mm)	2.78	-0.22	1.81	2.81
d (mm)	39.77	40.50	39.65	39.26
t_x (mm)	12.32	12.85	12.95	12.92
t_y (mm)	10.83	10.21	10.05	10.18
t_z (mm)	-6.06	-9.69	-12.41	-15.85
ρ_x (rad)	1.52	1.53	1.51	1.51
ρ_y (rad)	2.22	2.17	2.19	2.19
ρ_z (rad)	1.54	1.53	1.54	1.54
residual	67.05	94.81	110.74	88.18

Table 8: Results of the re-fitted nuisance parameters for four bed positions

Bed Position (mm)	0	3.33	6.67	10.0
t_x (mm)	12.46	12.66	12.91	12.99
t_y (mm)	10.63	10.44	10.11	10.06
t_z (mm)	-5.91	-9.28	-12.72	-16.06
ρ_x (rad)	1.53	1.53	1.51	1.52
ρ_y (rad)	2.21	2.19	2.19	2.18
ρ_z (rad)	1.54	1.53	1.54	1.54
residual	76.02	99.91	116.93	98.69

The MLEM reconstruction software was then altered to have an additional input file that provides information about each projection's acquisition angle and bed position, and the input geometric calibration file was altered to include the determined transformation matrix. The reconstruction software then automatically shifts the position in the reconstructed object-space according to the transformed bed position and the current rotation angle.

IV.5.1 Hot Rod Phantom

The hot rod phantom, also referred to as a Jaszczak phantom, that was used in this study was the Ultra-Micro Hot Spot Phantom (Data Spectrum Corp, Durham NC USA). A photograph and the schematic of an axial slice of the phantom are shown in Figure 31. The rods have diameters of 2.4, 2.0, 1.7, 1.35, 1.0, and 0.75 mm, and have a center-to-center distance of twice their diameter. This phantom was chosen as the rod diameters will fall within the expected range of the HPGe system's resolution (~1.5 mm). Prior to image collection, the previously described helical calibration method was performed using the 5-point phantom, where all five points were included in the process of determining the geometric calibration parameters. To correct for the previously discussed center of rotation error in section IV.4.1, the radius of rotation was set to be 39.8 mm to have a larger FOV in order to limit activity falling outside of the FOV. One collimator extender was used, giving the acquisition a focal length of 67.7 mm.

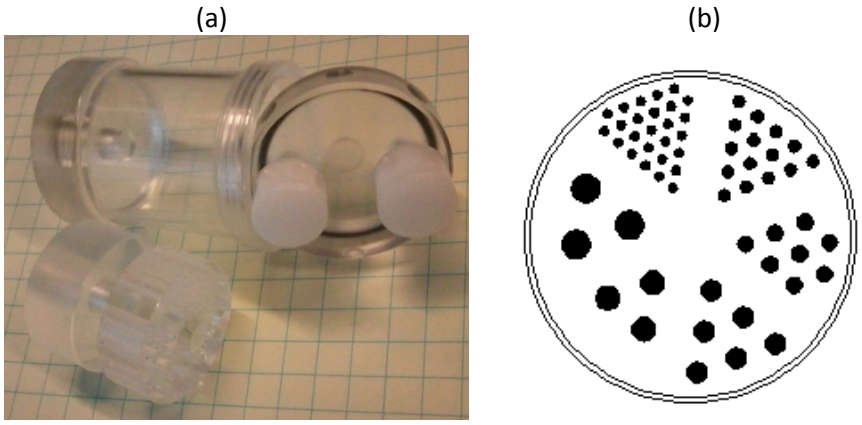

Figure 31: A photograph (a) and schematic (b) of the Ultra-Micro Hot Spot Phantom (Data Spectrum Corp, Durham NC USA). The rod diameters are 2.4, 2.0, 1.7, 1.35, 1.0, and 0.75 mm, with the center-to-center distance between rods being twice their diameter.

As the hot rod phantom fits within the axial FOV of the system, a stationary (non-helical) acquisition was performed. The phantom was filled with 49.58 MBq of ^{99m}Tc. 64 projections were acquired over 360° with 1.2 minutes collection time per projection. Detector non-uniformities were corrected for by multiplying the projection images by a normalization matrix determined by a flood scan. The gap pixels in the projections, which have zero counts, were

estimated in order to facilitate proper reconstruction. The gap values were estimated based on an area-weighted average of either its closest two neighbors for edge gaps or four diagonal neighbors for corner gaps. Images were reconstructed using the previously described MLEM algorithm. Reconstructed images have a 0.5 × 0.5 × 0.5 mm^3 voxel size and overall dimensions of 120 × 120 × 160 voxels. After reconstruction, the image was cropped to 80 × 80 × 90 voxels to eliminate edge of FOV artifacts from affecting the color-scale. Slices from the resulting reconstructed image at 25 iterations are shown in Figure 32. The axial phantom slice shows the spatial resolution of the system, with the 2.4, 2.0, and 1.7 mm rods being visible, while the smaller rods (1.35, 1.0, and 0.75 mm) are blurred together. This shows that the system resolution is in the expected range of ~1.5 mm.

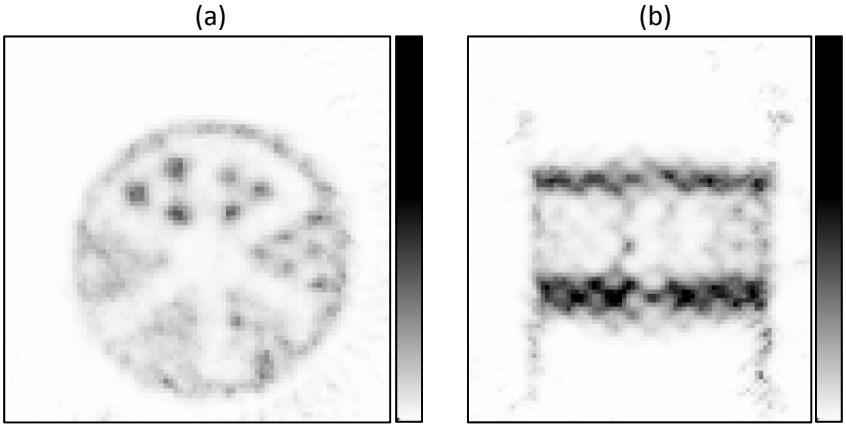

Figure 32: Image slices from the reconstructed stationary acquisition of the hot rod phantom at 25 iterations. (a) shows a single axial slice where rods as small as 1.7 mm are discernible. (b) shows a transaxial slice that highlights the gap artifacts in what should be regions of uniform activity above and below the hot rods.

Although the single axial slice in Figure 32 (a), appears to have reasonable resolution, the transaxial slice in (b) shows a checker-board-like grid artifact in what should be uniform regions of activity. The cause of this artifact is attributed to incorrect estimation of gap values, and is discussed in detail in section IV.6. One way to mitigate these effects is to use a helical acquisition, which is done in section IV.5.2 for the NEMA phantom.

To give perspective, the same phantom was imaged in the Bioscan NanoSPECT-CT system. The system has 4 camera heads, each with a 9-pinhole collimator. The rat collimators were used for this acquisition, with each of the four cameras having a 9-pinhole collimator with 2.5 mm diameters. The hot rod phantom was filled with filled with 62.53

MBq of ^{99m}Tc and imaged with a helical acquisition for a total imaging time of approximately 18 minutes. Image reconstruction was performed using the 'phantom' setting, which indicated low smoothing (25%), high resolution (150%), and high iterations (3 * 8). This resulted in an image with a 0.4 × 0.4 × 0.4 mm^3 voxel size and overall dimensions of 170 × 170 × 184 voxels. Resulting images are shown in Figure 33. In the resulting image the 2.4, 2.0, and 1.7 mm rods are clearly visible.

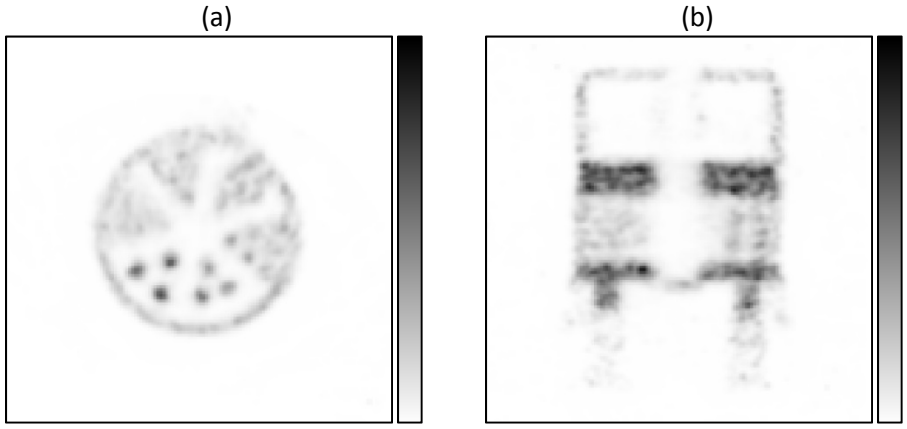

Figure 33: Reconstructed image from Bioscan NanoSPECT-CT system; (a) shows a single axial slice where rods as small as 1.7 mm are discernible, while (b) shows a transaxial slice.

IV.5.2 NEMA Phantom

The National Electrical Manufacturers Association (NEMA) published standards for the performance measurements of small-animal PET systems, NU-2008, part of which included the design of a phantom that can be used to measure image quality (NEMA 2008). Although this phantom was developed for small-animal PET systems, its size also makes it suitable to small-animal SPECT systems, and other groups have used the phantom, or slightly altered versions of it, to measure image quality (Harteveld, Meeuwis et al. 2011; Magota, Kubo et al. 2011; Visser, Harteveld et al. 2011). The phantom has three different sections: a section with two cold cylinders with a hot background, a larger uniform cylinder filled with radiotracer, and a hot rod section with five different rod diameters (1, 2, 3, 4 and 5 mm). A photograph of the phantom and three digital axial slices are shown in Figure 34.

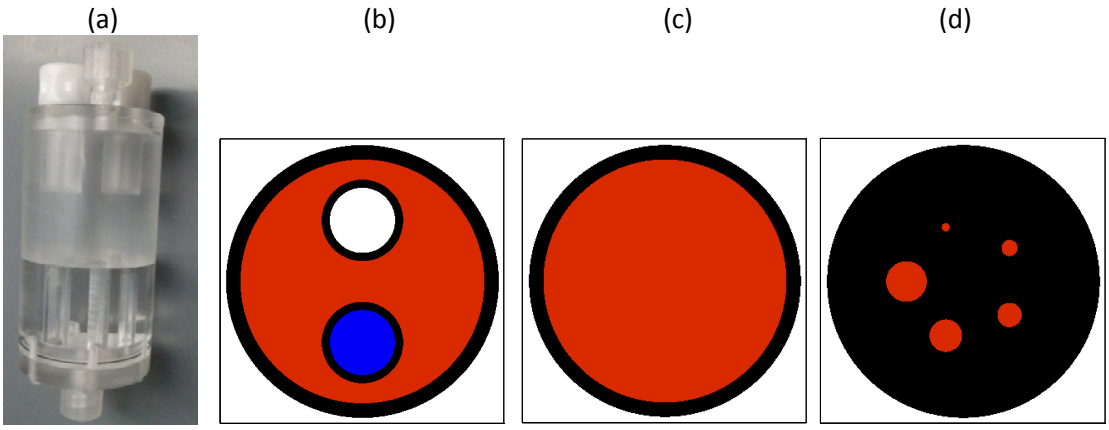

Figure 34: A photograph of the NEMA NU-2008 phantom (a) and slices of the three sections, including: cold-cylinder (b), uniform hot region (c), and hot rods (d) with 1, 2, 3, 4 and 5 mm diameters, where black indicates solid phantom material, red indicates regions filled with the radiotracer, and the white and blue in (b) represent the cold compartments generally filled with air and water, respectively.

IV.5.2.1 Acquisition Methods and Images

Imaging was performed on the same day as the previously described hot rod phantom, and therefore the same system configuration and geometric calibration results were used. The focal length was 67.7 mm and the radius of rotation was 39.8 mm. The NEMA phantom was filled with 106.9 MBq of ^{99m}Tc, giving a concentration of 5.17 MBq/mL. Four full camera rotations with 64 projections per 360° rotation were acquired at a pitch of 1.7 cm per rotation. Each projection had a 1.2 min collection time. The same projection processing was performed as with the hot rod phantom; a correction for non-uniformity was applied followed by the area-weighted averaging of nearest neighbors to estimate the number of counts in the gaps. The same MLEM reconstruction was used, with a resulting 0.5 × 0.5 × 0.5 mm^3 voxel size and overall dimensions of 120 × 120 × 160 voxels. Slices from the reconstructed image at 25 iterations are shown in Figure 35.

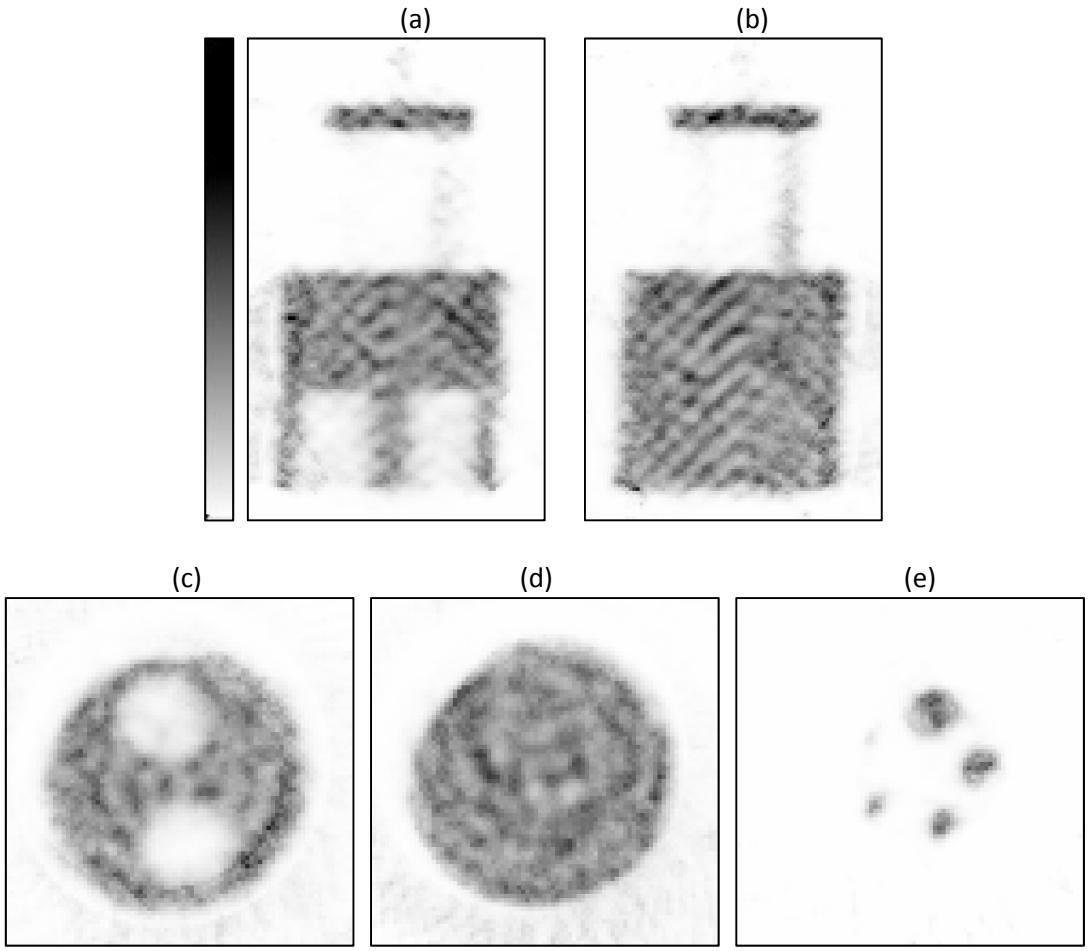

Figure 35: Transaxial (a) (b) and axial (c – e) slices of the reconstructed NEMA phantom, with axial slices showing the cold region (c), uniform region (d) and hot rods (e).

IV.5.2.2 Quantitative Analysis

The NEMA guidelines (NEMA 2008) clearly state the standard methods for quantitative assessment of image quality using the NEMA NU-2008 phantom. The three separate regions of the phantom allow for determination of the uniformity or image noise, rod recovery coefficients (RC), and spillover ratios for air (SOR_{air}) and water (SOR_{water}). The uniformity is defined as the percent standard deviation ($\%STD_{unif}$) of the activity concentration inside a volume of interest (VOI) drawn centered in the uniform region of the phantom. This VOI is 75% of the diameter and two-thirds of the height of the uniform cylindrical region.

To determine the rod recovery coefficients, first the central 10 mm of the rods are averaged to reduce noise, and the maximum value for each rod is divided by the mean phantom concentration to determine the RC. The coordinates of these maximum values are then used to create a line profile in the axial direction to obtain the standard deviation of the RC:

$$\%STD_{RC} = 100 * \sqrt{\left(\frac{STD_{lineprofile}}{Mean_{lineprofile}}\right)^2 + \left(\frac{STD_{background}}{Mean_{Background}}\right)^2}$$

Equation 21

The SOR_{air} and SOR_{water} are defined as the mean activity concentration measured in the air and water compartments, respectively, divided by the mean phantom concentration and determined from a cylindrical VOI centered in the region of half of the diameter and half of the height of the compartments. The standard deviations are determined in the same manner as $\%STD_{RC}$, as follows:

$$\%STD_{SOR} = 100 * \sqrt{\left(\frac{STD_{ROI}}{Mean_{ROI}}\right)^2 + \left(\frac{STD_{Unif}}{Mean_{Unif}}\right)^2}$$

Equation 22

For the reconstructed image in Figure 35, the calculated uniformity, $\%STD_{unif}$, was 20.3%. Each rod's RC and $\%STD_{SOR}$ are shown in Table 9. The spillover ratios were 0.101 and 0.113 for SOR_{air} and SOR_{water}, respectively, with $\%STD_{air}$ and $\%STD_{water}$ being 32.01 and 49.39, respectively.

Table 9: HPGe-SPECT NEMA rod RC results

	1 mm	2 mm	3 mm	4 mm	5 mm
RC	0.133	0.611	0.986	1.128	1.210
$\%STD_{RC}$	78.50	71.72	71.71	70.05	68.34

IV.5.2.3 Bioscan NanoSPECT NEMA Phantom

To give perspective to the results presented in the previous section, the same phantom was imaged in the Bioscan NanoSPECT-CT system. The same configuration was used for the NEMA phantom as for the hot rod phantom previously discussed, using the collimators with 9 pinholes with 2.5 mm pinhole diameters for each of the 4 camera heads. The NEMA phantom was filled with 52.91 MBq of ^{99m}Tc and imaged with a helical acquisition for a total imaging

time of approximately 24 minutes. The same reconstruction protocol as the hot rod phantom was used, giving a reconstructed image with a 0.4 × 0.4 × 0.4 mm^3 voxel size and overall dimensions of 170 × 170 × 246 voxels. Resulting image slices are shown in Figure 36. The same quantitative metrics were used in this data set as in the HPGe NEMA image. The $\%STD_{unif}$ was 25.18 and the RC for each rod and the $\%STD_{SOR}$ are shown in Table 10. The spillover ratios were 0.130 and 0.045 for SOR_{air} and SOR_{water}, respectively, with $\%STD_{air}$ and $\%STD_{water}$ being 44.50 and 45.85, respectively.

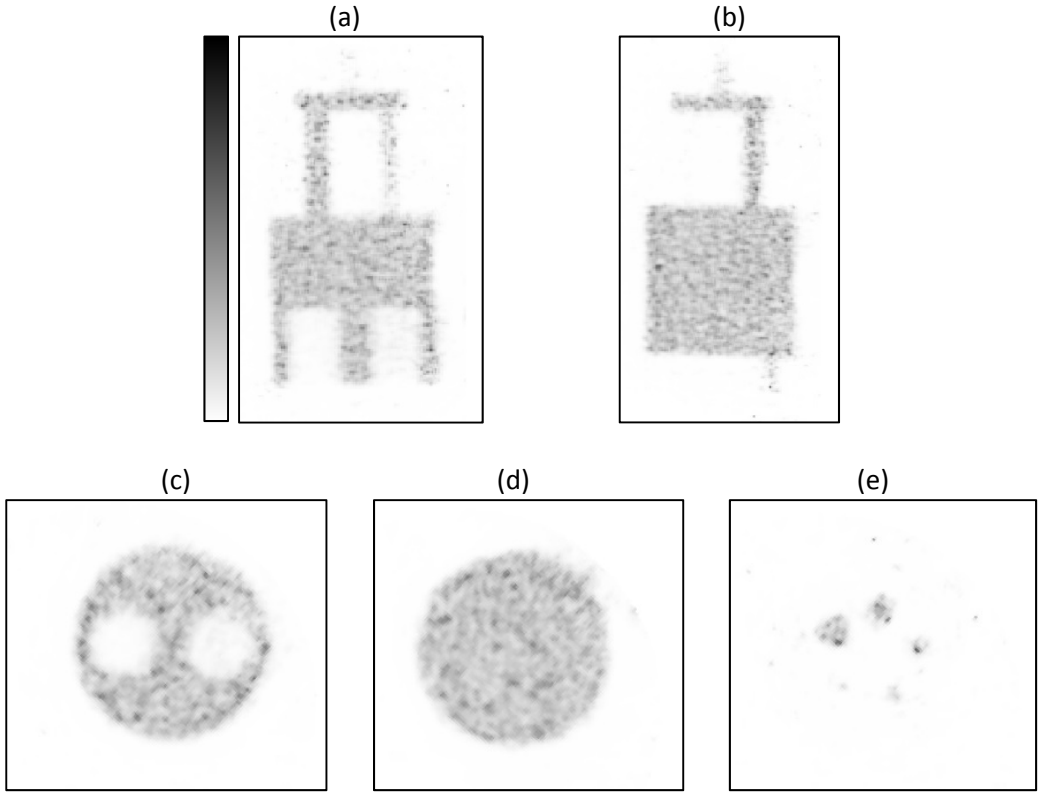

Figure 36: Reconstructed image slices from the Bioscan NanoSPECT-CT system of the NEMA phantom: transaxial (a) (b) and axial (c – e) slices, with axial slices showing the cold region (c), uniform region (d) and hot rods (e).

Table 10: NanoSPECT NEMA rod RC results

	1 mm	2 mm	3 mm	4 mm	5 mm
RC	0.178	0.861	1.260	1.335	1.166
$\%STD_{RC}$	196.3	182.0	180.4	176.5	180.2

IV.5.3 Dual-Isotope Acquisition

To demonstrate the benefit of HPGe's energy resolution, dual-isotope acquisitions using ^{99m}Tc and ^{123}I were acquired on both the Bioscan NanoSPECT and the HPGe-SPECT systems. The Bioscan NanoSPECT utilizes a NaI(Tl)

gamma camera, which typically have an energy resolution of ~10% at 140 keV (Hwang, Franc et al. 2008), while as previously shown the HPGe detector's energy resolution is ~1% at 140 keV. ^{123}I has an emission energy of 159 keV, while ^{99m}Tc's emission energy is 140 keV; the less than 20 keV difference between these energy peaks allow investigation of the ability of these two system to separate the two isotopes in multi-isotope images. For each system three short planar and three helical SPECT acquisitions were acquired, with each set having only a syringe filled with ^{99m}Tc, only a syringe filled with ^{123}I, or having two syringes, one with ^{99m}Tc and one with ^{123}I present.

IV.5.3.1 Planar Acquisitions

First, three planar acquisitions were performed according to Bioscan's instructions on how to determine the cross-talk factor, which is a built-in tool in the system's analysis software InvivoScope, that is used in multi-isotope acquisitions to help correct artifacts caused by spillover between energy windows. A 3 mL syringe was filled with 1 mL of ^{123}I solution having a total activity of 37 MBq at the start of scanning. Another syringe of the same volume was filled with 37 MBq of ^{99m}Tc. Based on the overlap of the energy spectra of the two isotopes, energy windows of 150.5 to 171.5 for ^{123}I and 122.5 to 149.5 keV for ^{99m}Tc were used for acquisition. Three four-minute planar acquisitions were acquired, where the ^{99m}Tc syringe, both syringes, and ^{123}I syringe were imaged and data collected in both energy windows for all scans. For the single-syringe acquisitions, the number of counts in the projections was summed for each energy window, and the ratio of the counts in the two windows determines the spill-over ratio correction factor. The ^{99m}Tc syringe only acquisition had 2.65×10^6 counts in the ^{99m}Tc energy window and 1.42×10^5 counts in the ^{123}I energy window, giving a cross-talk ratio of 5.3%. The ^{123}I syringe only acquisition had 1.43×10^6 counts in the ^{123}I energy window and 2.36×10^5 counts in the ^{99m}Tc energy window, giving a cross-talk ratio of 16.4%. The dual-syringe projection, acquired using a 9-pinhole collimator and shown in Figure 37, visually shows the effect of the energy-window cross-talk, with a second 'ghost' syringe appearing where only one should be present.

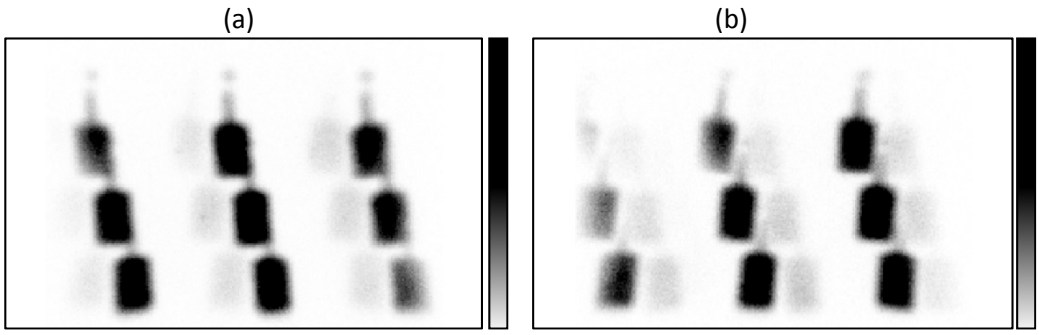

Figure 37: NanoSPECT dual-isotope planar images from (a) the ^{99m}Tc energy window and (b) the ^{123}I energy window. The cross-talk artifacts are seen as the shadow of the second, lower intensity syringes in the projections.

A similar acquisition scheme was performed on the HPGe-SPECT system, except with starting activities in the syringes as 31.82 MBq of ^{123}I and 24.42 MBq of ^{99m}Tc. A four-minute acquisition was performed with the single-pinhole collimator in place. For all HPGe projection acquisitions, only counts that are estimated to occur in a valid depth (between 1 and 10 mm) and within the UFOV defined in section III.7 are included in total count sums and projection images. Energy windows of 159 keV ± 2.5 keV and 140 ± 2.5 keV were used for ^{123}I and ^{123}Tc respectively. For the ^{123}I syringe only, 5.13×10^4 counts were recorded in the ^{123}I energy window, and 3.44×10^3 counts were recorded in the ^{99m}Tc energy window, giving a cross-talk ratio of 6.71%. For the ^{99m}Tc syringe only, 5.47×10^4 counts were recorded in the^{99m}Tc energy window and 167 counts were recorded in the ^{123}I energy window giving a cross-talk ratio of 0.31%. Both isotopes' energy-windowed projections from the dual-syringe planar acquisition are shown in Figure 38. Unlike the commercial NanoSPECT system, the HPGe SPECT system can save the entire pulse-height spectrum collected for each projection, therefore Figure 38 also includes the dual-syringe pulse-height spectrum from the acquisition. Both of the projection images show the HPGe SPECT system does not suffer from the same cross-talk artifacts that are shown in Figure 37, which is confirmed by the clearly separate peaks in the pulse-height spectrum. The cross-talk ratios of each system for each energy window are shown in Table 11.

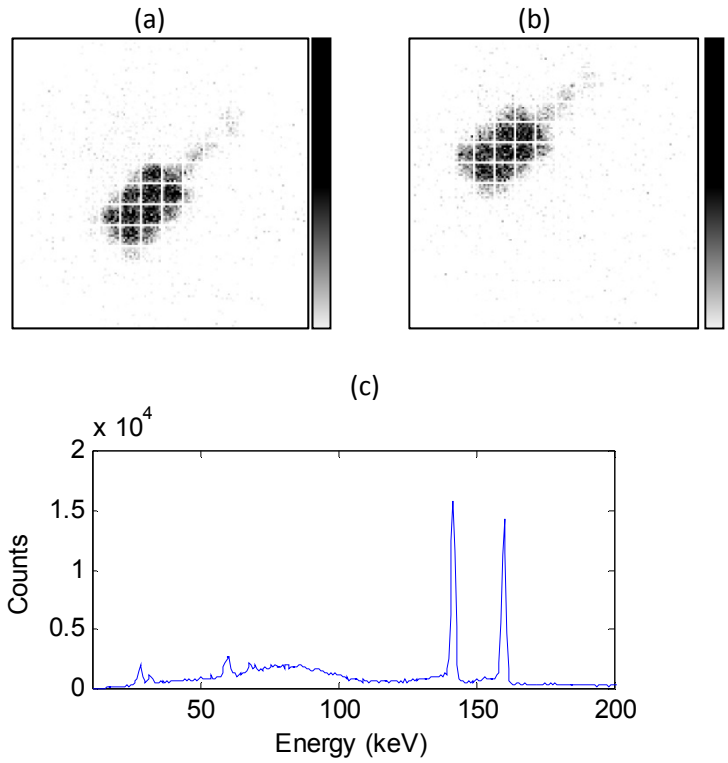

Figure 38: HPGe SPECT dual-isotope planar images from (a) the ^{99m}Tc energy window and (b) the ^{123}I energy window. The pulse-height spectrum, shown in (c), shows the clearly separable energy photopeaks.

Table 11: Cross-talk ratio comparison

	NanoSPECT	HPGe SPECT
^{99m}Tc into ^{123}I	5.3%	0.31%
^{123}I into ^{99m}Tc	16.4%	6.71%

IV.5.3.2 Helical SPECT Acquisitions

Helical SPECT acquisitions were collected using an acrylic phantom with two cylindrical bores. The same syringes were used as in the planar projection acquisition, and were placed into the hollow bores of the phantom for imaging. When only one radionuclide was being imaged, a syringe filled with the same volume of water was placed in the second empty bore. The NanoSPECT acquisitions were performed first, imaging the ^{99m}Tc only syringe, then both the ^{99m}Tc and ^{123}I syringes, and finally only the ^{123}I syringe. Both the ^{123}I and ^{99m}Tc energy windows were collected for each of the three data sets. Each scan acquired for 60 seconds per each of the 24 projections, for a total scan time of approximately 12 minutes. Following acquisition, projections were corrected for cross-talk between the energy windows using the

previously determined cross-talk ratios. For each syringe combination, images were reconstructed for both energy windows in addition to with and without cross-talk correction. All NanoSPECT images were reconstructed using the HiSPECT software with the 'standard' reconstruction setting, which applies 35% smoothing, 100% resolution and 3*3 OSEM iterations, which gave a reconstructed voxel size of 0.6 mm × 0.6 mm × 0.6 mm with 114 × 114 in-slice voxels and z-slice voxels varying depending on the chosen axial FOV of the helical acquisition. Reconstructed images were not calibrated to activity concentration, and therefore the units of the images are referred to as 'image intensity'. Figure 39 through Figure 41 show image slices of the three different images with and without the cross-talk correction.

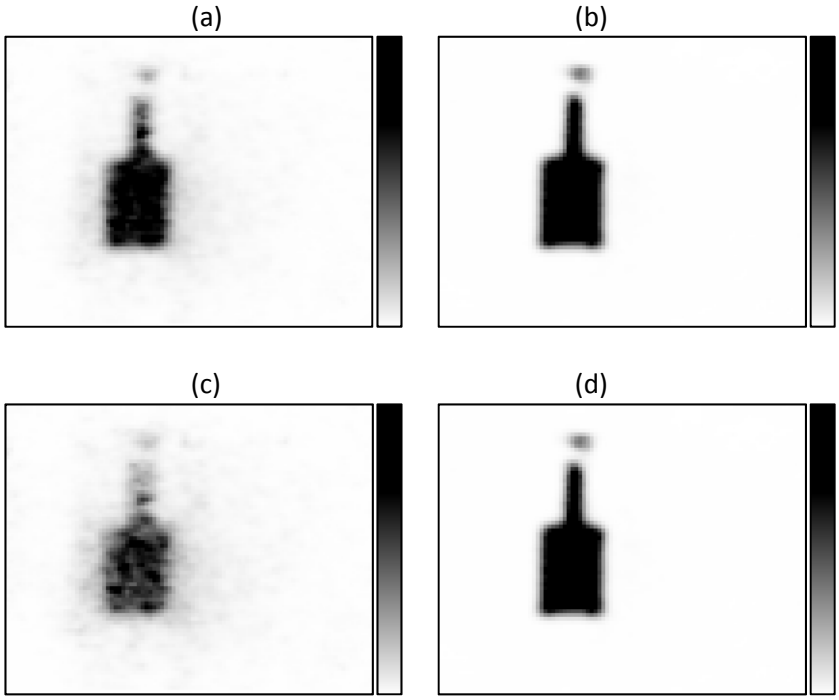

Figure 39: NanoSPECT image slices of the reconstructed ^{123}I Only acquisition without cross-talk correction for the ^{99m}Tc window (a) and the ^{123}I window (b), in addition to with the cross-talk corrected slices for the ^{99m}Tc window (c) and the ^{123}I window (d). The cross-talk correction reduces the cross-talk artifact between (b) and (d), but clearly does not completely eliminate the ghost artifact.

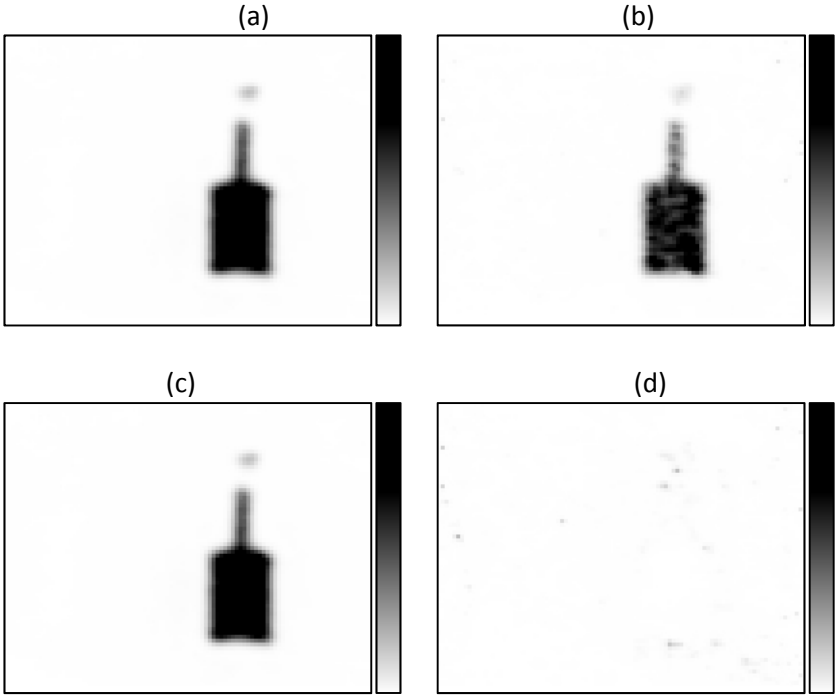

Figure 40: NanoSPECT image slices of the reconstructed ^{99m}Tc only acquisition without cross-talk correction for the ^{99m}Tc window (a) and the ^{123}I window (b), in addition to with the cross-talk corrected slices for the ^{99m}Tc window (c) and the ^{123}I window (d). Unlike in the ^{123}I case, the cross-talk ghost artifact in (b) is removed and no longer visible in (d).

Figure 39 shows slices from the ^{123}I only acquisition, and shows that even after cross-talk correction is applied, there are enough counts to drive the ^{99m}Tc window reconstruction to a ghost syringe artifact in the energy window that should just be background noise. In the ^{99m}Tc only acquisition, the ghost artifact is present in the uncorrected reconstruction, but not found in the corrected reconstruction. As ^{123}I has the higher emission energy, ^{99m}Tc photons do not scatter into its energy window, therefore the cross-talk correction, which is based on the amount of overlap of the two photopeaks in the pulse-height spectrum can easily correct for the cross-talk. This becomes more challenging with ^{123}I, because its photons can scatter, lose energy, and subsequently fall into the ^{99m}Tc window, which may not be accounted for due to the lack of scatter medium present in the cross-talk procedure. The amount of scattering is also object-dependent, making accurate corrections more difficult. This is likely why the correction improves, but does not eliminate the artifact in Figure 39 but does eliminate the artifact in Figure 40. Figure 41 demonstrates how these artifacts affect reconstructions when both isotopes are present, showing that the ghost artifacts are clearly visible when no corrections are employed, but require more drastic windowing in order to visualize when corrections are used. The

correction method does cause a negative artifact, where no signal is present in the ^{99m}Tc-syringe location of the ^{123}I window reconstruction. This may have negative effects on image quality and/or quantification if both radiotracers are localized in the same region.

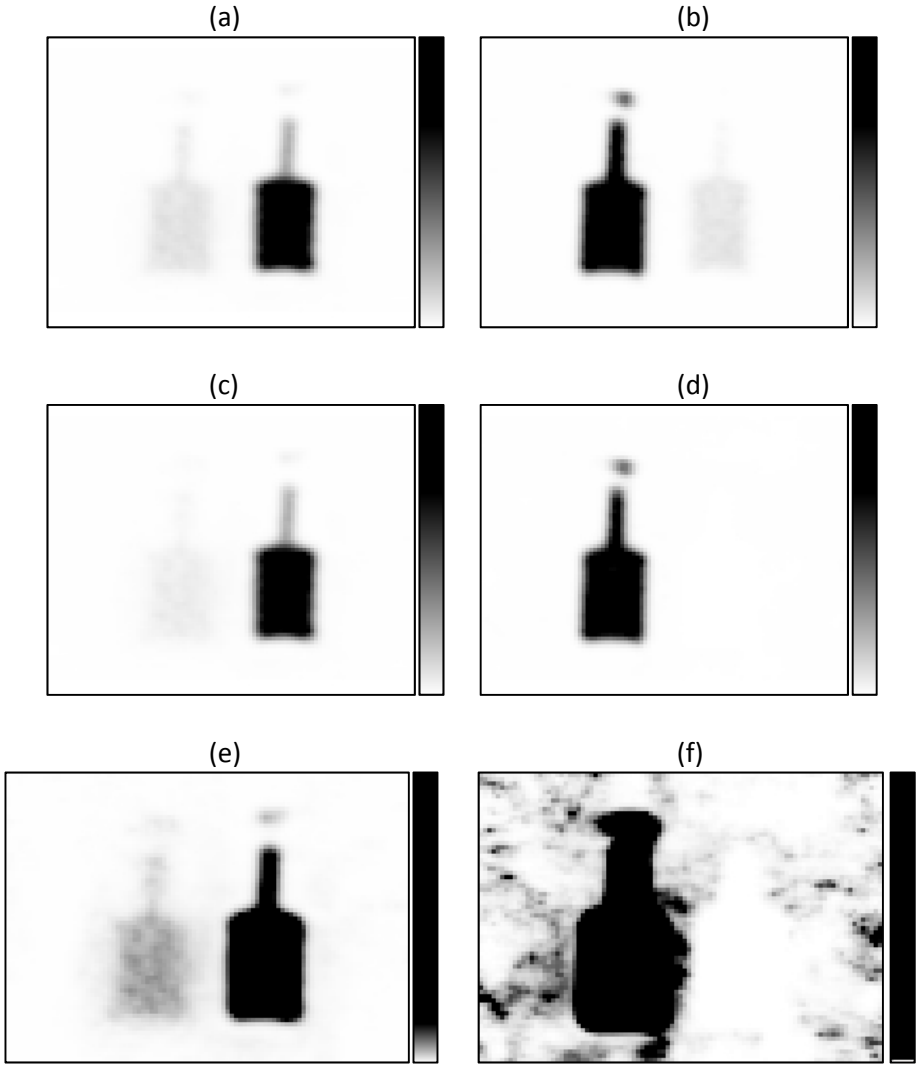

Figure 41: NanoSPECT image slices of the reconstructed acquisition with both isotopes present without cross-talk correction for the ^{99m}Tc window (a) and the ^{123}I window (b), in addition to with the cross-talk corrected slices for the ^{99m}Tc window (c) and the ^{123}I window (d). The cross-talk ghost artifacts are clearly seen in the uncorrected images, while the corrected images show better results. The ^{123}I window shows no artifact in (d), and when the color-scale is altered to be essentially an image mask in (f), it can be seen that the cross-talk correct eliminates all activity in the region of the ^{99m}Tc syringe. When the ^{99m}Tc window image's color-scale is lowered (e), the cross-talk artifact is once again visible.

The helical HPGe SPECT acquisitions were performed after the NanoSPECT images using the same syringes and imaging only the ^{123}I syringe, then both the ^{99m}Tc and ^{123}I syringes, and finally only the ^{99m}Tc syringe. At the start of the

first scan the ^{123}I syringe contained 30.71 MBq. The ^{99m}Tc syringe was filled with additional activity prior to imaging, and contained 32.56 MBq at the start of the ^{123}I and ^{99m}Tc acquisition. HPGe SPECT images were acquired in a helical scan with a pitch of 17.1 mm per 360° revolution. All scans acquired 64 projections over 360° for 60 seconds per projection, giving a total scan time of slightly over 1 hour. Raw data for the projections were collected with no energy windowing (0 to 270 keV), and were windowed post-acquisition to 159 ± 2.5 keV and 140 ± 2.5 keV for ^{123}I and ^{99m}Tc, respectively. As the energy windows can be made significantly smaller than the NanoSPECT system without excluding a large portion of counts, no cross-talk correction was implemented. Images were reconstructed using the previously described MLEM algorithm, with 0.5 mm isotropic voxel size and 120 × 120 × 160 voxels, which were subsequently rotated in the transverse plane such that the two syringes were visible in the same axial slice and cropped to 81 × 81 × 66 voxels to exclude pileup on the edges of the FOV. Resulting images are shown in Figure 42.

Unlike the uncorrected NanoSPECT images, there are no obvious artifacts in the reconstructed HPGe images, even in the more challenging case of the ^{123}I syringe reconstructed in the ^{99m}Tc window. This shows that qualitatively there is less cross-talk between the two energy windows when using the HPGe detector with excellent energy resolution compared to the standard NaI(Tl) detector, even with the manufacturer-provided cross-talk removal tools implemented. To compare, the both-syringe reconstructions' color-scales were lowered similar to those in Figure 41, and still show little to no cross-talk artifacts. However, there is a slight increase in background in the ^{99m}Tc window of the dual scan, which is in excess of what is seen in the ^{99m}Tc window of the ^{99m}Tc only acquisition when low color-scale thresholds are viewed. This background demonstrates that not enough counts are present for the image reconstruction to move towards a syringe shape as in the NanoSPECT example.

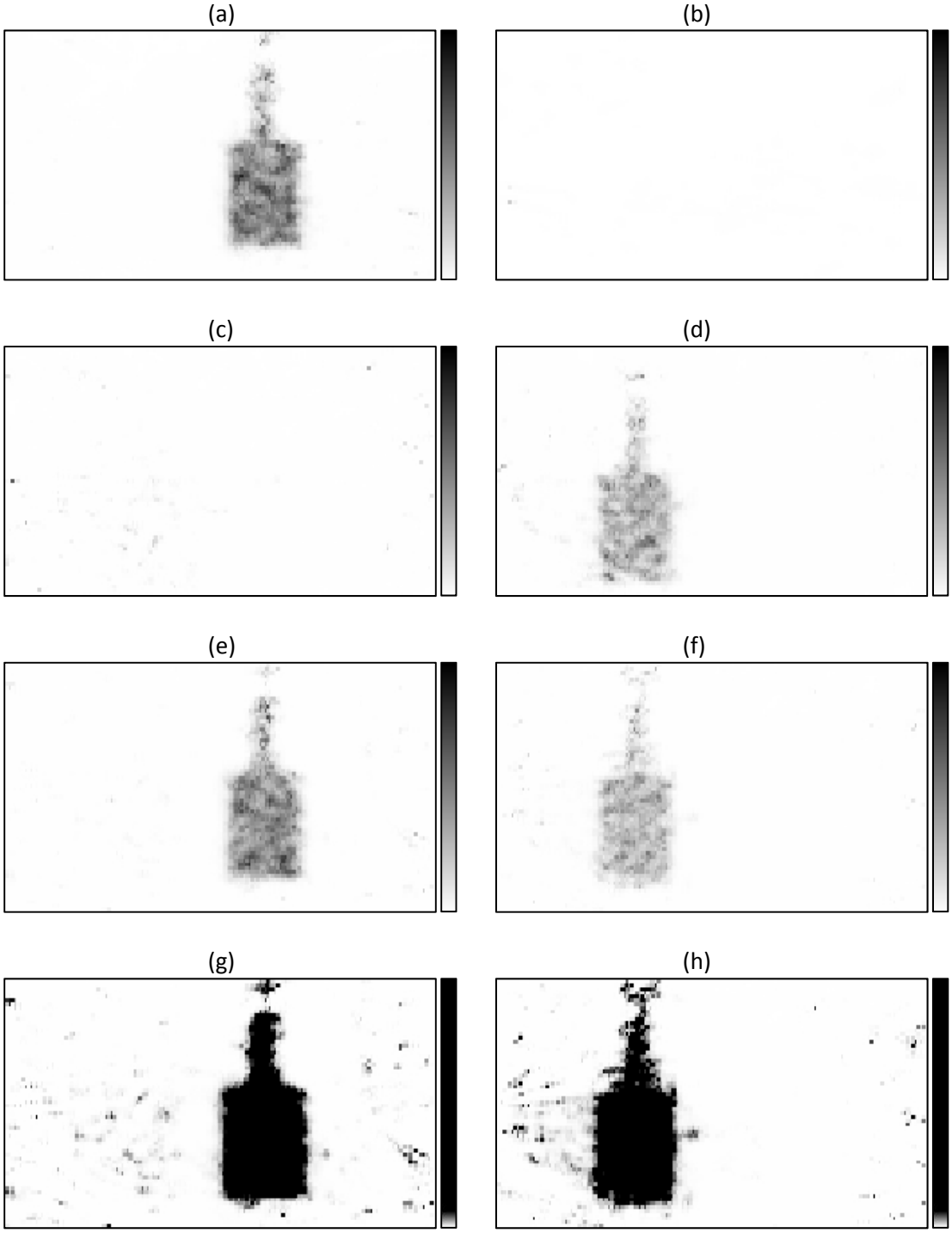

Figure 42: HPGe SPECT image slices of the reconstructed acquisition: ^{99m}Tc only with the window ^{99m}Tc (a) and ^{123}I window (b), ^{123}I only with the ^{99m}Tc window (c) and ^{123}I window (d), and both syringes with the ^{99m}Tc window (e) and ^{123}I window (f). Similar to Figure 41, the color-scale was lowered to allow for easier visual inspection of artifacts in the both-syringes acquisition, with (g) and (h) showing the ^{99m}Tc window and ^{123}I window, respectively.

IV.6 Effects of Detector Gaps on Image Quality

In section IV.5.2, the NEMA phantom shows a regular, grid-like or herringbone-like artifact in the uniform region of the reconstructed phantom (Figure 35 (b)). We hypothesized, and later verified in simulation, that these artifacts were caused by lack of signal collected in the gap regions of the detector. The gaps in the detector used in this project are 0.25 mm × 0.53 mm between strips and 0.25 mm × 0.25 at the strip corners. No counts are recorded in the gaps, and although smaller gaps give greater system efficiency, the gaps cannot be completely eliminated as strip separation is required for position information. Although other systems have gaps between read-out electrodes, they tend to be uniform with respect to the pixel size/placement and much smaller relative to the size of the pixel, but in our HPGe system sub-strip interpolation is used, making the gaps only appear after every 9^{th} pixel on projection images. The gaps are also fairly large relative to the detector pixel size, 0.25 mm compared to 0.53 mm. This section presents verification through simulation that the artifacts seen in images are due to the presence of the gaps, and describes several methods that were implemented to attempt to reduce the artifacts in the resulting images. None of these methods were able to fully correct the artifacts, and a second simulation is presented to determine how high the accuracy of the counts in the gaps must be in order to avoid artifacts.

IV.6.1 Determining the Effect of Missing Gap Counts in Simulation

The first step in addressing the artifacts seen in the images from section IV.5 is to verify that these artifacts are in fact due to the presence of gaps in the detector. To do this, a NEMA-like digital phantom was created. This phantom is similar to the version used in section IV.5.2, except that it does not have the hot rod section as the uniformity and spill-over regions are of interest here, which also this allows the NEMA-like phantom to fit within the axial FOV of the single-pinhole system. The phantom object had dimensions of 270 × 270 × 180 and a 0.167 mm isotropic voxel size. This phantom is located slightly off-axis to mimic the center-of-rotation error described in section IV.4.1. The object was forward-projected using the method described in section V.2.3, and used the same set of calibration parameters used to reconstruct the NEMA and hot rod phantoms from section IV.5. A single bed position was used for the initial simulation. This allows for a realistic simulation of the location of the object in image space and a more intuitive comparison

between the simulation and actual phantom data. The same MLEM reconstruction used in section IV.5 was used to reconstruct the noise-free projections. The first instance of the phantom was reconstructed with the correct gap value determined from the forward projections, while a second and third reconstruction had the gap values manually set to zero and double their original value, respectively. They have the same reconstructed voxel sixes as previous images, 120 × 120 × 160 with a 0.5 mm isotropic voxel size. The reconstructions' 25th iterations are shown in Figure 43.

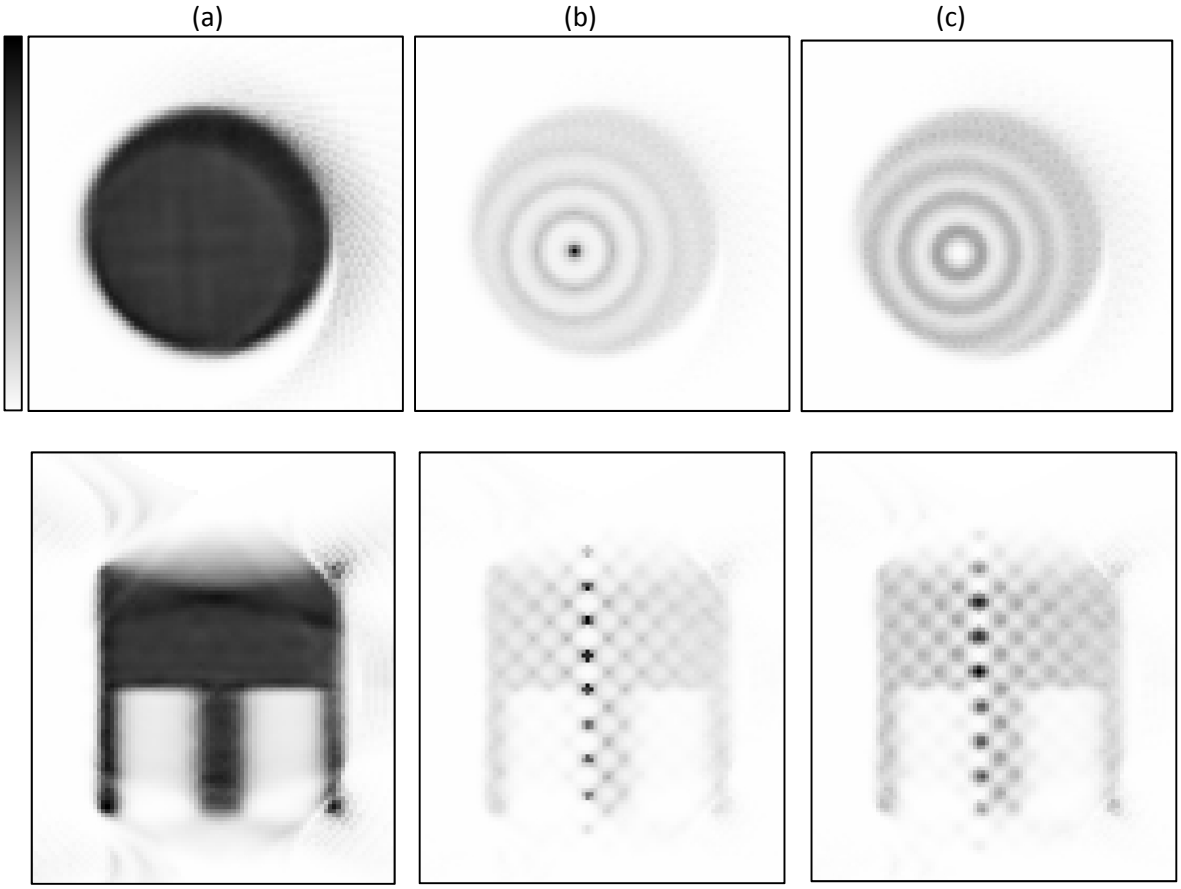

Figure 43: Example of simulated NEMA-like phantom that demonstrates effect of gaps in image quality showing axial and transaxial slices of correct gap values (a), gap values set to zero (b), and gap values doubled (c).

The checker-board-like pattern seen in Figure 32 (b) follows the same trend as the under (b) and over (c) estimated gap values in Figure 43. The artifacts arise very quickly in the reconstruction process, and can be seen in the first iteration of both the zero-gap and double gap reconstructions. One interesting trend is the shift in the high and low intensity regions of the grid-pattern between the over and under-estimates of the gap values. This shows that the when the gap region is underestimated counts are piled away from gap-sensitive regions, while in the over-estimate case

counts are in the gap-sensitive regions, shifting the artifact. To minimize the effect of the gaps, we implemented helical scanning. This approach should allow for more even sampling of the object space from gap and non-gap regions of the detector. Results for a similar noise-free simulation (correct gap values, zeroed gaps, and doubled gaps) are shown in Figure 44 for a helical reconstruction with a 1.7 mm pitch and two detector revolutions. These results show a similar pattern to those in the real reconstructed NEMA phantom (Figure 35), which change the grid-pattern to a more spiral, herringbone-like pattern, which mimics the helical acquisition path.

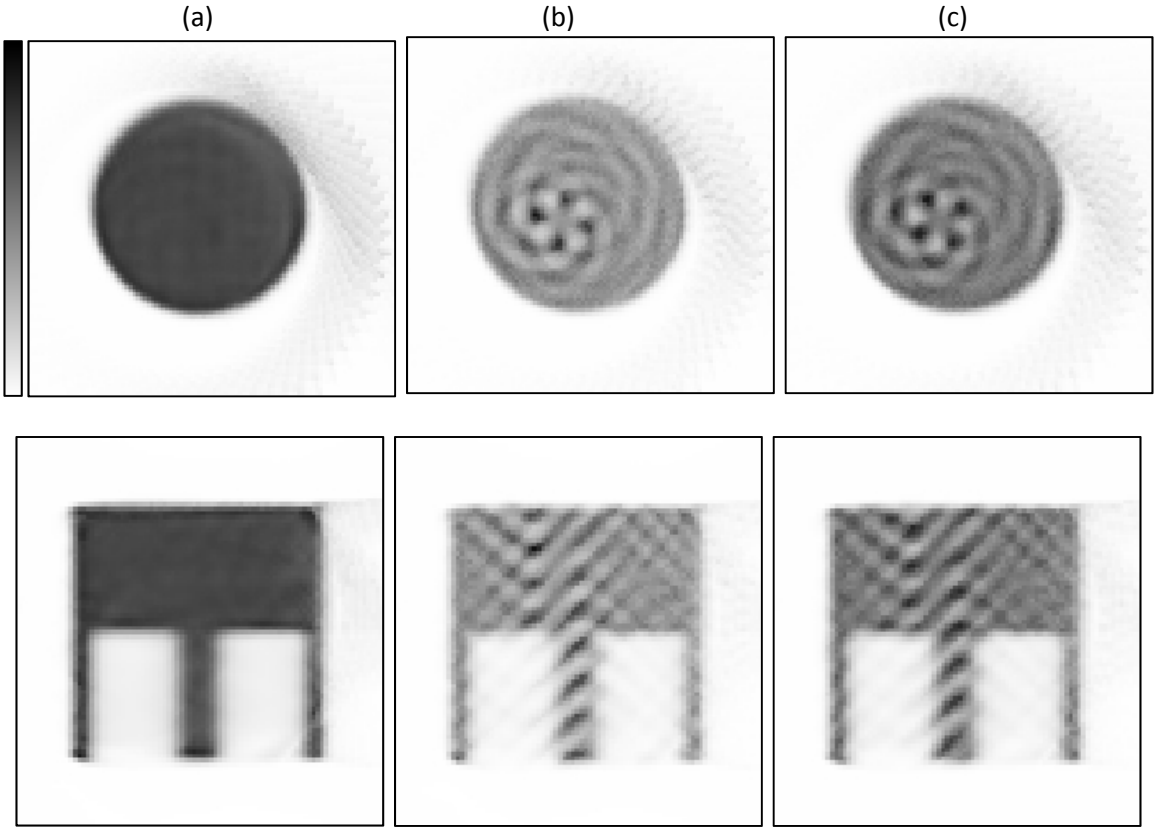

Figure 44: Simulated helical reconstruction of NEMA-like phantom for correct gap (a), zeroed gap (b), and doubled gap (c) values. Artifacts in (b) and (c) show similar trends to actual acquired phantom data (Figure 35).

IV.6.2 Attempted Methods of Gap Correction

The reconstruction algorithm used accounts for the non-uniform pixel size of the projection images, but there is no clear solution as to how to estimate or update the gap value when the recorded counts in the pixel are zero. If the

standard MLEM algorithm is used, the zero values in the gaps drastically skew the reconstruction due to the multiplicative nature of the algorithm (Equation 10). One simple way to avoid this is to create an image mask which performs different actions based on whether or not a pixel in the projection is located in a gap. The first correction attempt was to simply 'skip' the update of the gap pixel, which is equivalent to assuming that the current estimate of the gap is correct, and thus the correction factor would simply be 1. This allows the value of the gap to be driven solely by the activity of the object near and around the gaps since the gap value is not updated. This preliminary test did not adequately deal with the gap artifacts, as this caused the regions of the object that project near the gaps to converge at a different rate than the rest of the object. This caused images with similar artifacts to those shown in Figure 35.

The second attempt to correct gap artifacts was the method used to process the data in the experimental section (IV.5) of this chapter. The projection images were first flood corrected to account for non-uniformities in the detector response. Following flood correction, the value of the gaps was estimated by averaging its two nearest neighbors in the case of edge-gaps, or the four diagonal neighbors in the case of corner gaps. These estimates were subsequently weighted to account for the difference in area, and the reconstruction algorithm was altered to account for the spatially-varying pixel size of the projections. Although the results shown in the experimental section (IV.5), especially those acquired with a helical acquisition, show less severe artifacts, the patterns they create in the reconstruction images are still very obvious.

A final method to attempt to better estimate the gap values utilized additional processing of raw data from the Imager32 software. Original work with the detector utilized counts that were fully processed by Imager32, with each event including the sub-strip position in the x and y direction, depth of interaction in the detector (z), and the energy of the deposited photon. These events include only interactions in which charge is collected on a single strip on both sides of the detector. It was hypothesized that additional event data could be used to estimate events in the gaps. This was done by recording the 'semi-raw' data from Imager32, which includes interaction information from events in which charge is collected on multiple strips of the detector. These data include the relative arrival time, strip number, energy deposited (slowE), and the energy collected on the two nearest neighbors (fastE) for each interaction in the total event

cascade. This raw data, which is saved during acquisition, can be re-sorted after imaging acquisition to only include events that interact on two strips on one detector side and one strip on the other (often referred to as 2-1 or 1-2 events). These events can subsequently be filtered to only include events that have the two-strip interaction occur on two adjacent strips within a close timing window and to have the sum of two same-side events fall within a reasonable energy-window to minimize the collection of Compton interactions being included. This method has been used in previous HPGe signal processing of Compton interactions (Hayward and Wehe 2008).

To test the feasibility of this method, a 4-hour ^{57}Co flood image was first acquired. The events were saved in the 'semi-raw' format and re-processed post-acquisition to include the two-strip events that arrive in a ± 20 ns energy window (± 1 clock cycle) with an energy window of ± 6 keV. The results of these processed gap events are shown in Figure 45.

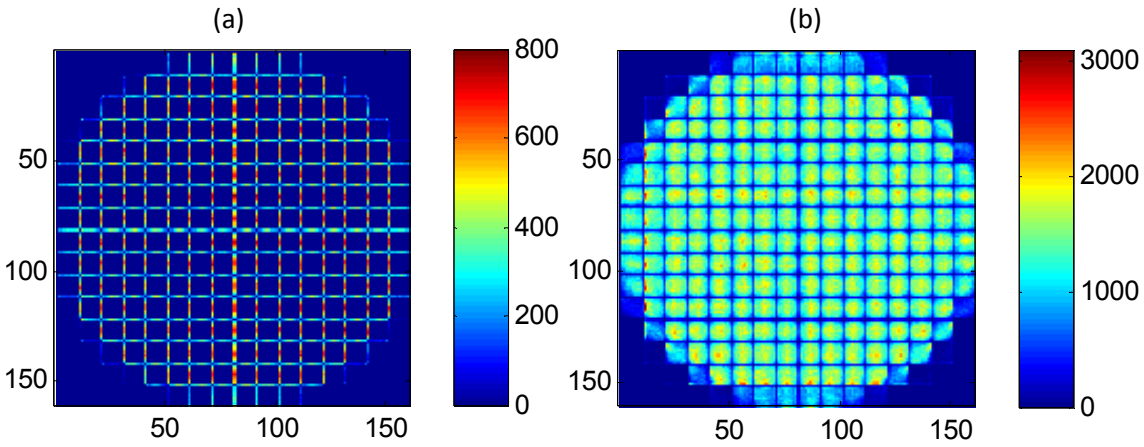

Figure 45: Processed 'semi-raw' events to estimate number of counts in the gaps showing (a) the processed gap events and (b) the gap events and the standard events that occur in the detector strips. It is clear that although some recovery is possible, the recovered gap counts are significantly lower than that of the counts collected in the strips.

The gap-only projection shows that although there appears to be a reasonable amount of counts being recovered, when compared to the number of counts in the flood's non-gap pixels there is still a large discrepancy. Additionally, there is an obvious difference in the gap counts collected on the front (x-direction) and back (y-direction) of the detector. This is most likely due to the fact that charge collected on the back of the detector has a longer distance to propagate, and therefore the charge cloud diffuses more by the time of collection than the front-side interactions,

leading to more counts spread over 2 strips. Although these values can be flood-corrected in the same manner that was used for the sub-strip positioning, there are challenges to applying these corrections when projection images have few counts. Figure 46 shows an example of a typical projection image, in this case an uncorrected projection from the helical NEMA phantom shown in section IV.5.2, where the gap values have been estimated (but not normalized). In Figure 46 (b), the image has been zoomed into the uniform region and masked to show that a large portion of the estimated raw gaps, especially in the x-direction where less gap events are seen, have zero counts. This makes the flood-correction method useless as pixels with zero counts cannot be corrected using a multiplicative factor. This would propagate the zero counts in the projections, and subsequently distort reconstructed images.

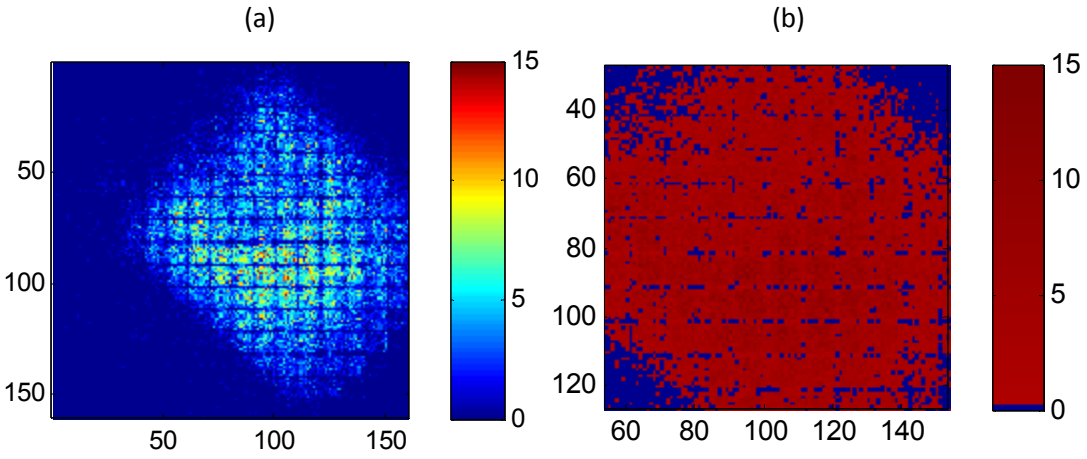

Figure 46: Example of a single NEMA phantom projection with raw gap events processed, with (a) showing the full projection and (b) showing a zoomed-in version that is masked to show where normalization would fail due to no gap events being present.

IV.6.3 Sensitivity of Image Reconstructions to Inaccurate Gap Estimations

To better understand these artifacts an additional simulation of the NEMA-like phantom was performed. The NEMA-like digital phantom was forward-projected as in section IV.6.1 such that the true values of the gaps were calculated along with the rest of the projection. The same geometric calibration file as in section IV.6.1 was used in the forward-projection in order to give resulting images similar to those acquired experimentally, and a single-bed position (non-helical) acquisition was simulated. The gap values were then lowered by 10, 7, 5, and 2.5% to gain perspective on how much variation in the gap estimate is tolerable before artifacts in the reconstructed images appear. Slices of images

from this test at the 25th MLEM iteration are shown in Figure 47. The gap artifacts can be clearly seen in the 10% case, and can be seen slightly in the 2.5% case. Although in an experimental acquisition there is likely to be some over-estimation or under-estimation of the gap values, this simulation shows that due to the regular grid/patterned nature of the gap locations, the reconstruction is very sensitive to slight deviations of the gap values.

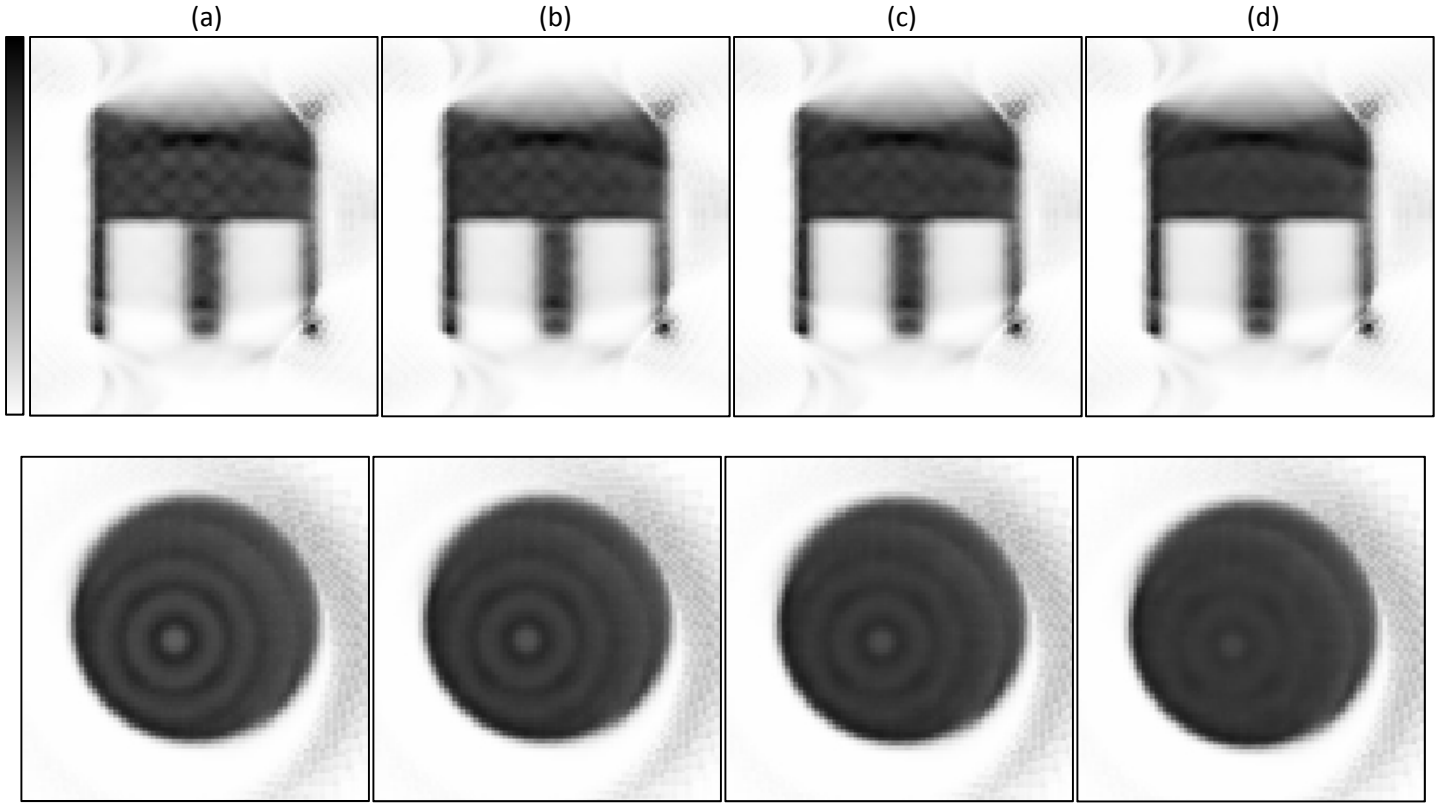

Figure 47: Effect of inaccurate gap estimation on image quality, with (a), (b), (c), and (d) showing the results of reducing the gap value by 10, 7, 5, and 2.5%. The upper row shows transaxial slices while the lower row shows axial slices. As the percent reduced is lowered, the amplitude of the artifact pattern decreases, although it can still slightly be seen even in the lowest 2.5% case.

A potential confounding factor to inaccurate gap estimations is the sub-strip position estimation process. It is likely that due to charge sharing, charges are less likely to move/be collected near the edge of strips, resulting in a lower number of counts being collected on the neighbors to gaps. But, in the process of sub-strip position estimation, this difference is ignored and counts are forced into an even distribution across a strip. Even though counts should, in theory, be equally distributed across a strip using this method, in flood acquisitions non-uniform detector response within a strip is still present (as shown in the uncorrected flood shown in Figure 45 (b)). This inaccuracy, even when

flood-corrected, could be part of the cause as to why the neighbor-averaging technique does not completely compensate for the gap effect.

Future work with this system will involve investigating additional ways to better estimate gap values, which could also include additional ways to estimate sub-strip position. For example, instead of a single flood-acquisition to determine the nearest neighbor ratios, a highly-collimated point source could be stepped through detector space to better estimate the ratio of charge collection on neighboring strips. Better position estimation near the edges of strips would then lead to better gap estimation when the averaging method is used. Another possibility is to use the same collimated beam placed directly over a gap to gain a better understanding of the detector response to gap events. This could be used to better process the 'semi-raw' data used in section IV.6.2 and possibly leading to more gap events being recovered.

IV.7 Discussion

IV.7.1 System Resolution

Spatial resolution in small-animal systems that utilize pinhole collimators, as shown in Equation 2, is determined by both the intrinsic resolution of the detector, and the geometric resolution of the system (Equation 1), which is dependent on the pinhole diameter and the system magnification. There is an inherent tradeoff between the field of view and the resolution for a given detector size, therefore making a direct comparison of intrinsic spatial resolution less insightful without overall system configuration being included. In the case of the HPGe system configuration, the ROR was extended to correct for the off-center pinhole position, therefore lowering the system magnification and subsequently the spatial resolution. Although the spatial resolution, determined by inspection of the hot rod phantom as being between 1.7 mm and 1.35 mm, is in the expected range, there are a wide variety of other small-animal systems that have better spatial resolution. This preliminary HPGe SPECT-CT system was designed to demonstrate capabilities of HPGe for SPECT in a straight-forward manner and has not been optimized for high-resolution imaging; it is expected that the other small-animal systems will have similar or better spatial resolution performance.

A small-animal SPECT system developed at UCSF for myocardial perfusion imaging of mice uses a 1.0 mm pinhole, 3.8 cm ROR and has 1.1 mm spatial resolution (Wu, Hasegawa et al. 2002), and when a 0.5 mm pinhole is used has spatial resolution less than 1 mm. Another single-pinhole system designed by Metzler et al. used a 1.0 mm pinhole with a 4.0 cm ROR and gave a spatial resolution of 1.6 mm (Metzler, Jaszczak et al. 2005). Some systems with multiple pinholes allow for better resolution, such as the U-SPECT II system, which utilizes collimators with 75 pinholes with 0.35 or 0.6 mm diameters, and has a spatial resolution as small as 0.35 mm in certain configurations. In the future, larger HPGe detectors will allow for more flexible system configuration, and the addition of multiple detectors around the subject with multi-pinhole collimators will allow for increased spatial resolution by maintaining sensitivity if pinhole diameters are decreased.

IV.7.2 Comparison of NEMA Quantification Results

Although the NEMA phantom was designed for small-animal PET, and has been used to quantify image quality of a variety of different PET systems (Goertzen, Bao et al. 2012), some groups have used it to investigate image quality in SPECT systems. One challenging aspect of comparing these quantification values across systems is that SPECT systems can have drastically different spatial resolution, fields of view and sensitivity that depend on pinhole configuration. Magota et al. used the phantom in the Inveon preclinical tri-modality system, but did not follow the NEMA guidelines for quantification, and therefore results are not compared (Magota, Kubo et al. 2011). Harteveld et al. used the phantom with the U-SPECT-II system to investigate system performance with different reconstruction correction techniques and different levels of activity (Harteveld, Meeuwis et al. 2011). The phantom was filled with 81.4 MBq of ^{99m}Tc and imaged for 1 hour. Twenty scans were acquired sequentially, with the final scan having 7.92 MBq of ^{99m}Tc. Rod RC values were reported for 1, 2, and 3 mm rods for varying filtering and reconstruction corrections. At higher iterations the 3 mm rod with no filtering had a RC of 1.3, and with filtering it lowered to 0.8. This is in the same range as the 3 mm rod from both the NanoSPECT (1.26) and the HPGe SPECT (0.97). In the 1 mm rod case, all three systems lacked the resolution to properly estimate the activity, with 0.2, 0.17, and 0.13 RCs for Harteveld's U-SPECT-II, NanoSPECT, and HPGe SPECT, respectively.

SOR_{air} and SOR_{water} were also in similar ranges for all three systems, with U-SPECT-II having 0.1 and 0.7 for air and water, while the NanoSPECT had 0.10 and 0.05 and HPGe had 0.10 and 0.11 for SOR_{air} and SOR_{water}, respectively. The uncorrected U-SPECT-II SORs follow the expected trend of having a slightly higher SOR_{water} than SOR_{air} due to the increasing probability of photon scatter in water over air. With no corrections in the HPGe, the SORs are similar; this shows that scatter within the water does not affect image quality due to the energy resolution of the system. The NanoSPECT's reconstruction software does not clarify the exact correction methods employed by its proprietary algorithm, but results show much lower activity in the water category than the air, which implies that overcorrection might be occurring.

The $\%STD_{unif}$ of the U-SPECT-II system was ~27 when a 1.0 mm FWHM filter was used, while the NanoSPECT and HPGe-SPECT had $\%STD_{unif}$ of 25.18 and 20.3, respectively. Although quantitatively the HPGe SPECT images have better uniformity, it is obvious that this measure does not capture structural artifacts, which are clearly present in the uniform slice in Figure 35. It is expected that the uniformity of the HPGe SPECT will improve once the structural artifacts due to gap effects are corrected.

These results show quantitatively that HPGe SPECT performs similarly to other commercial small-animal SPECT systems. It does not require the additional scatter correction required in the commercial systems to reduce the effects of scatter in the SORs due to its energy resolution. Its resolution is similar to that of the rat apertures on the NanoSPECT system as shown in both of the hot rods in the NEMA phantom and in the hot rod phantom.

CHAPTER V

SIMULATION OF MULTIPLEXING EFFECTS IN A DUAL-DETECTOR SI-HPGE SYSTEM

V.1 Background

SPECT image quality is limited by a number of factors, including a system's detection efficiency. Efficiency can by improved in pinhole systems by placing multiple detectors and collimators around the object being imaged, and by increasing the number of pinholes on a particular collimator. The amount of physical space available around an object to be imaged limits the number and arrangement of detectors that can be used; therefore to maximize efficiency typical systems include multiple detectors with multi-pinhole apertures. Although multi-pinhole collimators increase detection efficiency, they often result in multiplexing, or overlap in pinhole projections on the detector, which leads to artifacts in reconstructed images (Mok, Yuchuan et al. 2009). The amount of multiplexing on a projection depends on the magnification of the system and the spacing/positioning of the pinholes on the collimator. There have been many investigations that developed methods to quantify the impact of multiplexing, and methods for determining the optimal multiplexing through pinhole configuration, which were discussed in detail in section II.2.2.2.

Previous work in our lab has utilized the concept of synthetic collimation (described in section II.2.2.4), by using two sets of stacked Si detectors for imaging of ^{125}I radiotracers in small animals. The stacked system allows for projections to be collected at multiple magnifications, allowing for limited angle acquisitions to be reconstructed (McDonald 2010). This staked system gave way to the idea of utilizing a stacked Si and NaI(Tl) system for use with ^{123}I, as it emits at almost equal amounts of 27-32 keV and 159 keV photons, allowing the Si detector to collect the lower-energy photons and the NaI(Tl) to collect the 159 keV photons. This stacked idea involves using the typical collection of many angles of projection data for use in the SPECT reconstruction. The feasibility of this study was investigated with our lab's Si detector and a modular NaI(Tl) gamma camera (McDonald, Shokouhi et al. 2007), and it was determined that scatter from one detector into the second only accounted for approximately 1% of the camera's detected counts within the appropriate energy window. This stacked system idea led to the idea of replacing the modular NaI(Tl) gamma camera

with a HPGe detector. One benefit of using the HPGe detector instead of the NaI(Tl) camera is that detected scatter would be slightly lower for the Si-HPGe system given that HPGe's energy resolution is significantly better than that of the NaI(Tl) gamma camera tested, and smaller energy windows can be used to reject these scattered events.

One limitation of the MI4.1 HPGe system used in Chapters III and IV is that, given the limited detector area, moving to a multi-pinhole system to increase sensitivity will most likely lead to some amount of multiplexing, particularly if a large number of pinholes are used. To mitigate these multiplexing artifacts, we hypothesize that pairing an HPGe detector (with high multiplexing) with a Si detector that has a small enough focal length to have minimal multiplexing will improve image quality over using the highly-multiplexed HPGe projections alone.

In a simulation study, a multi slit-slat collimator for clinical brain scans was modeled to investigate whether the reconstruction of multiplexed projections can be improved by the addition of non-multiplexed projections (Mahmood, Erlandsson et al. 2010). They investigated three different object phantoms, with different projection multiplexing and varied the ratio of multiplexed to non-multiplexed projections included in reconstructions. They determined that spatial resolution could be maintained with a reduction in noise, quantified by a 25% increase in SNR, when non-multiplexed projections were included with multiplexed projections in reconstruction. They followed this simulation with an experimental validation and found similar trends in improvement, except with lower SNR gains that were dependent on the amount of multiplexing present in the projections (Mahmood, Erlandsson et al. 2011).

Although we currently have both the HPGe and the Si systems available in our lab to build this type of stacked-detector system, the scope of this aim is to investigate in simulation to what degree a second detector can help to reduce multiplexing artifacts in images. The motivation and methods of this study were based on those of Mok et al., who investigated the effects of object activity distribution on multiplexing artifacts (Mok, Tsui et al. 2011). This investigation is divided into three main parts. The first part investigates how to combine the different detector projections into a reconstruction algorithm, testing both MLEM and different subset configurations of OSEM. The second part investigates the resolution and sensitivity tradeoff for the detector pixel size and pinhole diameter of the silicon system. The final part uses the reconstruction algorithm from results of part one and the silicon system configuration

from part two to investigate the effect of the additional Si projections on multiplexing artifacts in four different object types with varying amounts of multiplexing due to differing pinhole configurations.

V.2 General Simulation Methods

V.2.1 System Configuration

The system geometry is shown in Figure 48. The 6-cm square silicon detector (1 mm thick) is placed between the pinhole collimator and the 12-cm square HPGe detector (1 cm thick). The silicon detector, which our lab purchased from SINTEF ICT (Norway), actually has 1024 × 1024 strips with a 59 µm pitch, but was reduced in the simulations to 256 × 256 strips (0.234 mm × 0.234 mm) or 512 × 512 (0.117 mm × 0.117 mm) to allow for faster reconstruction times and to reduce the influence of noise in reconstructions. The HPGe detector is simulated to have 240 × 240 pixels of size 0.5 mm × 0.5 mm. The simulated detector was chosen to be larger in size than our actual detector (circular 8 cm in diameter as opposed to a 12-cm square) to allow for a larger range of multiplexing variation in the projections, with higher-multiplexing pinhole configurations not fully utilizing the entire detector area. The system has a 4 cm ROR, with a focal length of 2 cm and 7 cm for Si and HPGe, respectively, giving a magnification of 0.5 and 1.75 for Si and HPGe, respectively.

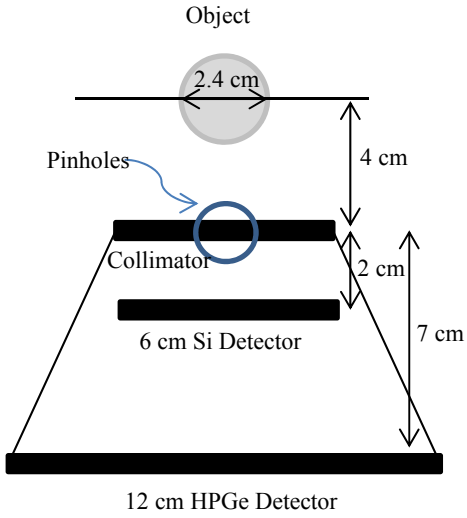

Figure 48: Configuration of simulated stacked detector system, with Si placed close to the collimator to limit multiplexing of projections.

Three different pinhole combinations were used for the simulations. All pinholes have a 1 mm diameter and a 70° full opening angle in a 1-cm thick tungsten plate. Three multi-pinhole collimators with varying amounts multiplexing were used. A four-pinhole collimator with holes spaced on a 10-mm radius circle allowed for a low amount of multiplexing (p4LM), while 4 pinholes spaced on a 7-mm radius created a higher amount of multiplexing (p4HM). The final high-multiplexing case was a 7-pinhole collimator with 6 pinholes on a 7-mm radius and one pinhole placed at the center (p7). The pinhole configurations are shown in Figure 49, with each determining a different amount of projection multiplexing depending on the object. Additionally, the configurations with multiple pinholes had random jitter added to their position to remove potential aliasing effects from sampling at a given set frequency.

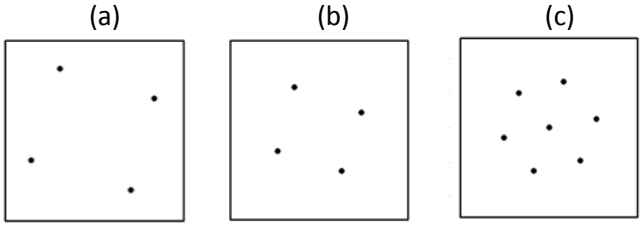

Figure 49: Pinhole configurations of the 4-pinhole low multiplexing (a), 4-pinhole high multiplexing (b), and seven-pinhole (c) collimators.

V.2.2 Simulated Objects

Four digital object phantoms were used in the various simulations: a Cool Sphere, Hot Rod, Cold Rod, and a variation of the NEMA phantom (Altered-NEMA), as shown in Figure 50. All objects were simulated with 300 × 300 × 300 voxel space with dimensions 0.1 × 0.1 × 0.1 mm^3. The Hot and Cold Rod phantoms have rods with diameters of: 3.0, 2.4, 1.6, 1.2, 1.0, and 0.75 mm. The Cool Sphere phantom has a center sphere of 4.2 mm diameter with an activity 30% lower than the rest of the object. The Altered-NEMA phantom has two sections, one with five hot rods of 1, 2, 3, 4, and 5 mm diameters and a height of 16 mm centered on a 7 mm radius circle, and the second section consists of a single cold-cylinder region (8 mm diameter, 10 mm height) placed off-center inside of a uniform activity-filled cylindrical region (28 mm diameter, 12 mm height). To simulate noise, objects were given activity concentrations that corresponded to a ten minute scan of 111.0 MBq, 18.5 MBq, 88.8 MBq, and 74.0 MBq for the Cool Sphere, Hot Rod, Cold Rod, and Altered-

NEMA, respectively, and Poisson noise was added to the noise-free projections prior to reconstruction. Each simulation set includes reconstructions of 20 different Poisson noise realizations and one noise-free.

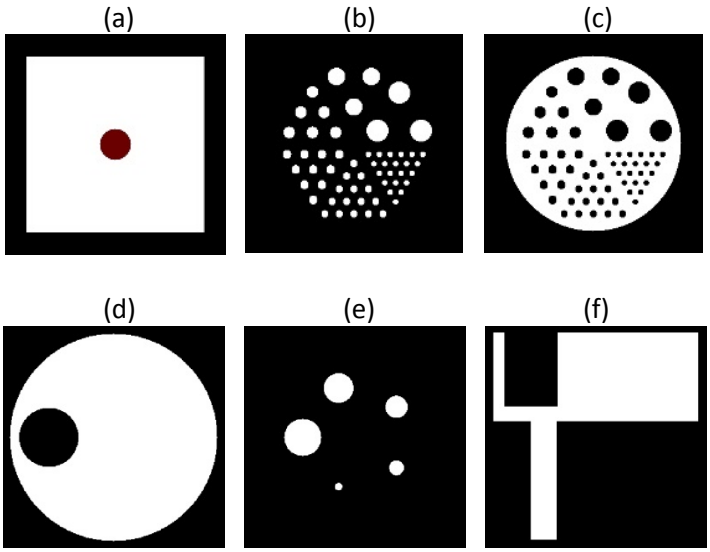

Figure 50: Single, central slices of simulated objects: (a) Cool Sphere, (b) Hot Rod and (c) Cold Rod. Rod diameters range from 3 mm to 0.75 mm. Slices of sections of the Altered-NEMA phantom are shown, including uniform/cold cylinder (d) and hot rod (e) regions and a coronal slice of the rods, cold cylinder and uniform region (f).

V.2.3 Analytical Simulation Methods

For all simulations, the previously described digital object phantoms were forward projected through the desired pinhole configuration for 64 projections over 360°. The percent of multiplexing for each data set was determined using the method of Shokouhi et al. (Shokouhi, Wilson et al. 2010), in which the sum of counts in detector pixels contributed by projections through more than one pinhole is divided by the total number of counts in the detector. The amount of multiplexing for each detector's projection, pinhole, and object combination is shown in Table 12, when the Si pixel dimensions were 512 × 512. The resulting forward projections (with or without added Poisson noise) were then used as an input into the reconstruction algorithms. Although multiple reconstruction algorithms were tested (MLEM, OSEM, etc.), all were based on an analytical system matrix that incorporates the geometric positioning of the pinhole collimator in conjunction with a voxel-based ray tracing method to determine the sensitivity of the detector to a position in object-space. The forward projector and reconstruction methods did not include penetration, scatter or attenuation in the collimator, scatter within the detector, nor scatter or attenuation in the object.

Table 12: Percentage of multiplexing in each object, pinhole, and projection combination

	Cold Rod		Cool Sphere		Hot Rod		Altered-NEMA	
	Si	**Ge**	**Si**	**Ge**	**Si**	**Ge**	**Si**	**Ge**
p4LM	0%	29.71%	0%	28.61%	0%	19.95%	0%	37.62%
p4HM	7.56%	72.97%	6.91%	72.78%	4.91%	65.05%	14.05%	74.40%
p7	68.21%	94.19%	67.64%	94.35%	56.72%	90.92%	71.04%	94.86%

Si and Ge detector intrinsic detection efficiencies were modeled for their appropriate energy ranges. The Si detector efficiency was determined using the NIST database (Hubbell and Seltzer 2004) that gave the mass attenuation coefficients for the 27-32 keV emission range, which were then converted into a single linear attenuation coefficient by weighting each attenuation coefficient by the probability of emission, which was determined to be 4.794 cm^{-1}. The linear attenuation coefficient for HPGe, which includes coherent scattering, was also calculated from NIST to be 1.246 cm^{-1}, which results in an intrinsic efficiency of 71%. Previous simulations and actual data using a 122 keV source in HPGe demonstrate significantly lower efficiency, most likely due to scattering across detector strips, charge not being fully collected, and gap effects. To better estimate the efficiency value, colleague Desmond Campbell performed a simulation similar to section III.4 except it used 159 keV photons to model ^{123}I. The linear attenuation was estimated from simulation results, and was found to be 0.7029 cm^{-1}, giving a detection efficiency of 49.7%. This result is, as expected, slightly lower than the ~55% efficiency at 122 keV determined in section III.4. The intrinsic efficiency was incorporated into both the forward projections and the reconstruction algorithms. All reconstructed images were 60 × 60 × 60 voxels of size 0.5 × 0.5 × 0.5 mm^3.

V.2.4 Quantitative Image Analysis

Two different quantitative metrics are used in this aim to characterize and compare image quality. The average normalized mean square error (NMSE) is used to evaluate error in images, while the normalized standard deviation (NSD) is used as a measure of noise.

Error in reconstructed images was determined by using the average normalized mean square error (NMSE) for the noisy images. The average NMSE,

$$average\ NMSE = \frac{1}{n}\sum_{j=1}^{n}\left(\frac{x_j - \lambda_j}{\bar{\lambda}}\right)^2,$$

Equation 23

is calculated as in (Mok, Tsui et al. 2011), where *n* is the number of voxels in the reconstructed volume, λ is the voxel value in the original phantom, $\bar{\lambda}$ is the mean voxel value of the original phantom, x is the voxel value in the reconstructed image, and j is the voxel index.

Again, NSD was based on the method used in (Mok, Tsui et al. 2011), and is based on the mean and variance of the 20 noisy reconstructed images. The NSD was calculated over a region of 2,100 voxels, which was drawn in 3D regions of uniform activity in each of the different object types. The NSD was calculated as:

$$average\ NSD = \frac{1}{n}\sum_{j=1}^{n}\frac{\sqrt{\frac{1}{m-1}\sum_{i=1}^{m}\left(x_j^i - \overline{x_j}\right)^2}}{\overline{x_j}},$$

Equation 24

where *m* is the number of noise realizations (20 in this case), *n* is the number of voxels in the selected region of interest, *x* is the voxel value in the noisy image, $\bar{x}$ is the mean voxel value of the noisy reconstructions, *i* is the noise realization index, and *j* is the voxel index.

V.2.5 Differential Point Response Function

While the NSD and NMSE allow for quantitative comparison of image quality, we also used the differential point response function (DPRF) to qualitatively evaluate multiplexing artifacts (Hesterman, Kupinski et al. 2007). First, a lumpy background object was created using an altered form of The University of Arizona's Center for Gamma-Ray Imaging's Gaussian Lump MATLAB code. A 3D object with 300 × 300 × 300 voxels was created by using a mean of 310 Gaussian spheres having a magnitude of 1, a radius of 20 voxels and a DC offset of 10. Next an object the same size as the lumpy background was created with a point of very low activity at its center and zero elsewhere. To give perspective, the sum of the intensity of all voxels in the lumpy object was 1.09×10^9, while the intensity of the single voxel of signal in the small signal object was 500. These objects were then forward-projected separately using the same algorithm described

previously in section V.2.3. The forward projections of both the lumpy object and the small signal object were summed together and reconstructed to form a combined lumpy and signal object. The original lumpy projections were also reconstructed. Finally, the original lumpy-only image was subtracted from the combined lumpy and signal image, and the resulting image – the DPRF – visually shows any artifacts due to multiplexing. Figure 51 shows an example set of reconstructed images from a single-pinhole, MLEM reconstruction of only the Ge projections of the lumpy object without (a) and with (b) the small-signal object present, and the difference of the images (c).

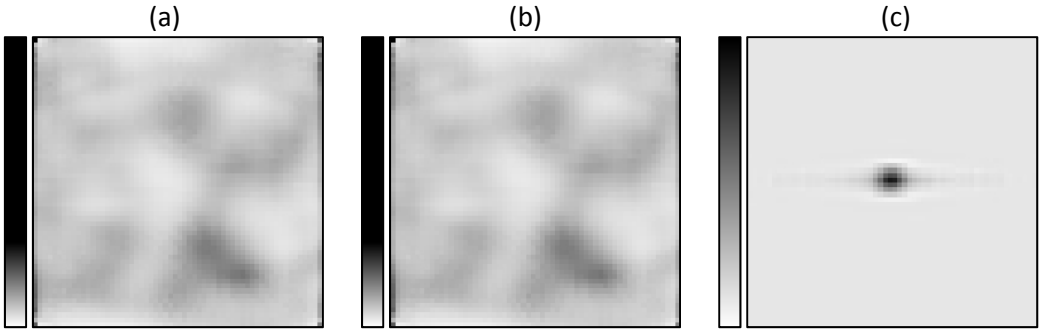

Figure 51: Example of reconstructions using lumpy-only projections (a) and the combined lumpy-signal projections (b) are shown for at the 25th iteration. The difference between the reconstructed images, the DPRF, is shown in (c).

V.3 Simulation Part 1: Determine Reconstruction Method

V.3.1 Cool Sphere Object for Reconstruction Testing

As discussed in section II.2.3, the most commonly used reconstruction techniques in small-animal SPECT are OSEM and MLEM. Because the proposed system in this study involves utilizing projections from two detectors, each having its own magnification, resolution, and noise properties, how to most effectively combine the projections in a reconstruction algorithm is not obvious. Four different reconstruction algorithms were tested, including: (1) MLEM with all projections from both Si and HPGe used each iteration, (2) OSEM with 8 subsets, with the first four subsets using all of the Si projections and the next 4 subsets using all of the HPGe projections, (3) OSEM with 2-phases, where a number of iterations are first completed with 4 subsets of only Si projections, followed by a second phase of 4 subsets of only HPGe projections, and (4) another OSEM with 2-phases, where the first phase uses 4 subsets of only Si projections and

the second phase uses 8 subsets, 4 with Si followed by 4 with HPGe. The Cool Sphere phantom was forward-projected through the highly-multiplexing seven-pinhole collimator having 1-mm diameter pinholes with the system configuration shown in Figure 48 with Si projections having 256 × 256 (0.234 mm × 0.234 mm) pixels. Twenty noisy and one noise-free sets of projection data were reconstructed using each of the four reconstruction algorithms, and for a 4 subset OSEM reconstruction using only Ge projections (Ge Only) for comparison. As the convergence point was unknown at the time of running the simulations, reconstructions were run to the point of over-iteration (300 iterations for MLEM and 150 iterations for OSEM) to ensure reconstructions reached convergence.

In order to implement the two-phase reconstructions, the update number at which the reconstruction changes from using the first phase projection set to the second phase projection set, or the switch-point, must be determined. The switch-point should occur when the first phase image reaches its ideal stopping point, which occurs at a balance between the amount of noise in the reconstruction and its accuracy. This tradeoff is shown in NSD versus NMSE curves, where the origin of the curve represents a perfect reconstruction – no noise and perfect accuracy. To determine the optimal switch-point, Si only reconstructions were first run beyond a reasonable optimal number. The NSD versus NMSE was then plotted for each update, where the ideal switch-point would be the update number that minimizes the distance to the origin. However, the scales of the two axes – the NMSE and NSD – cannot be converted into units that allow them to be comparable. To determine a reasonable switch-point, the Si only curve was first shifted relative to its own minimum value, such that the minimum NMSE value was set to zero and the rest of the NMSE values were linearly shifted by the minimum. The same method was applied to the NSD, resulting in a plot that has 'zero-shifted' axes, which helps to correct for large differences between the scales of the NSD and NMSE values. The update number that corresponds to the minimum distance to the zero-shifted origin is calculated and then rounded to the nearest complete iteration and is subsequently used as the switch-point between the Si projection subsets and the Ge projection subsets. The NSD versus NMSE is shown in Figure 52, where the large 'X' indicates the point on the curve that is the minimal distance to the zero-shifted origin. The actual minimum point occurred at iteration 15, update 59, but this was rounded

up to update 60 to allow for all subsets in the iteration to be computed, and subsequently was used as the stopping point for the Si projection only phase of the two-phase reconstruction.

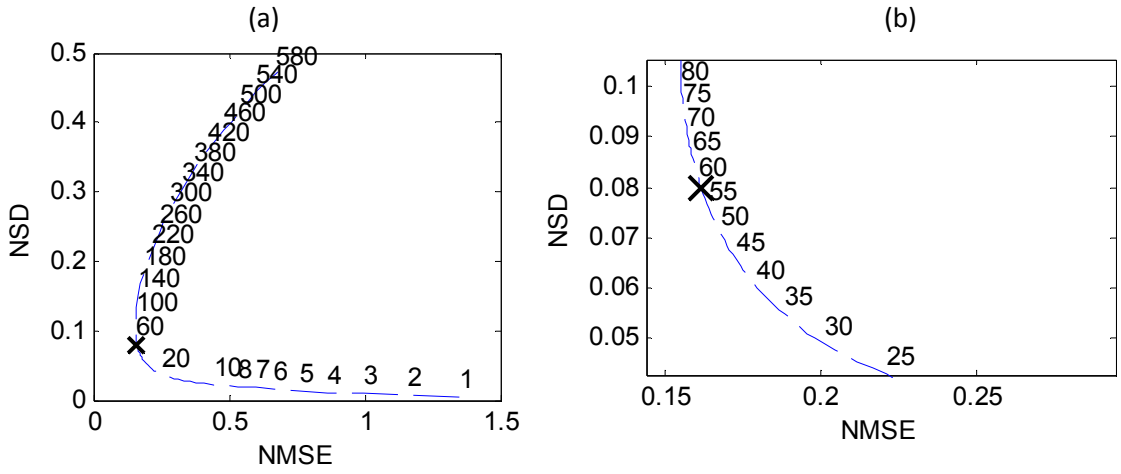

Figure 52: NSD versus NMSE for an OSEM reconstruction with 4 Si subsets of the Cool Sphere phantom with the seven-pinhole collimator. (a) shows the update number (4 updates per iteration), and an X indicates the minimum distance from the origin to the curve, (b) shows an inset of the same plot.

After all reconstructions were completed, the NSD and NMSE values for each reconstruction type at every iteration were calculated. The results are shown in Figure 53. Visual inspection of the zoomed plot shows an obvious improvement in the NSD versus NMSE tradeoff when the two-phase OSEM algorithm with 4 Si subsets followed by 4 Ge subsets is used. The sharp turn of the curve occurs when the reconstruction changes from the Si OSEM phase to the Ge OSEM phase. The ‘x’ indicates the location of the zero-shifted minimum, rounded to the nearest complete iteration in the OSEM cases, and is used as the iteration at which to compare the reconstructions. These iteration and update numbers are shown in Table 13.

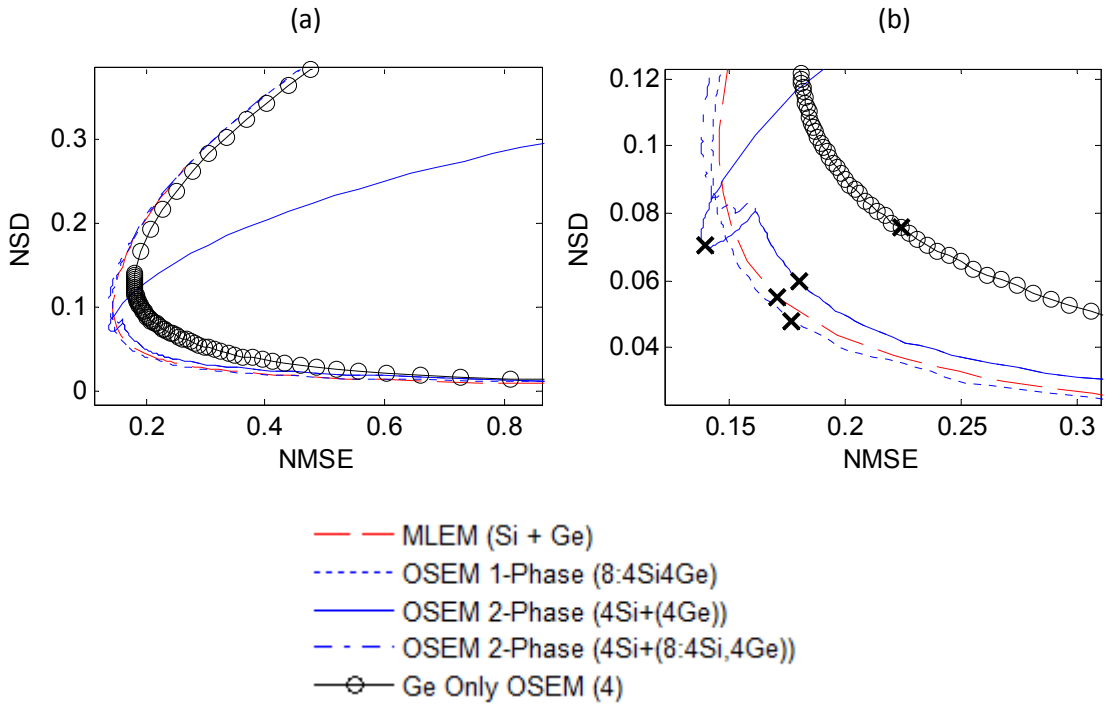

Figure 53: The NMSE vs NSD are shown for the Si + HPGe reconstructions with (a) showing the overall trends and (b) showing an inset of (a) with the minimal (zero-shifted) distance to the origin for each curve marked with 'x'.

Table 13: Comparison iteration and update number for each reconstruction algorithms

Recon:	OSEM Ge Only	MLEM Si + Ge	OSEM 1 Phase	OSEM 2 Phase (4 Si + 4 Ge)	OSEM 2 Phase (4 Si + (4Si 4Ge))
Iteration	9	40	4.5	20	10
Update	36	40	36	80	40

Figure 54 shows slices of the reconstructed images at the determined optimal iteration. For the OSEM 2 Phase 4 Si + (4 Si + 4 Ge) results, the minimum value actually occurs during the first Si Only phase of the results, eliminating the inclusion of the second detector and therefore eliminating the purpose of the two-detector multiplexing study. The image slices show that the Ge Only reconstruction has very visible artifacts, with a dark band moving down through the center of the slice shown in Figure 54 (a).

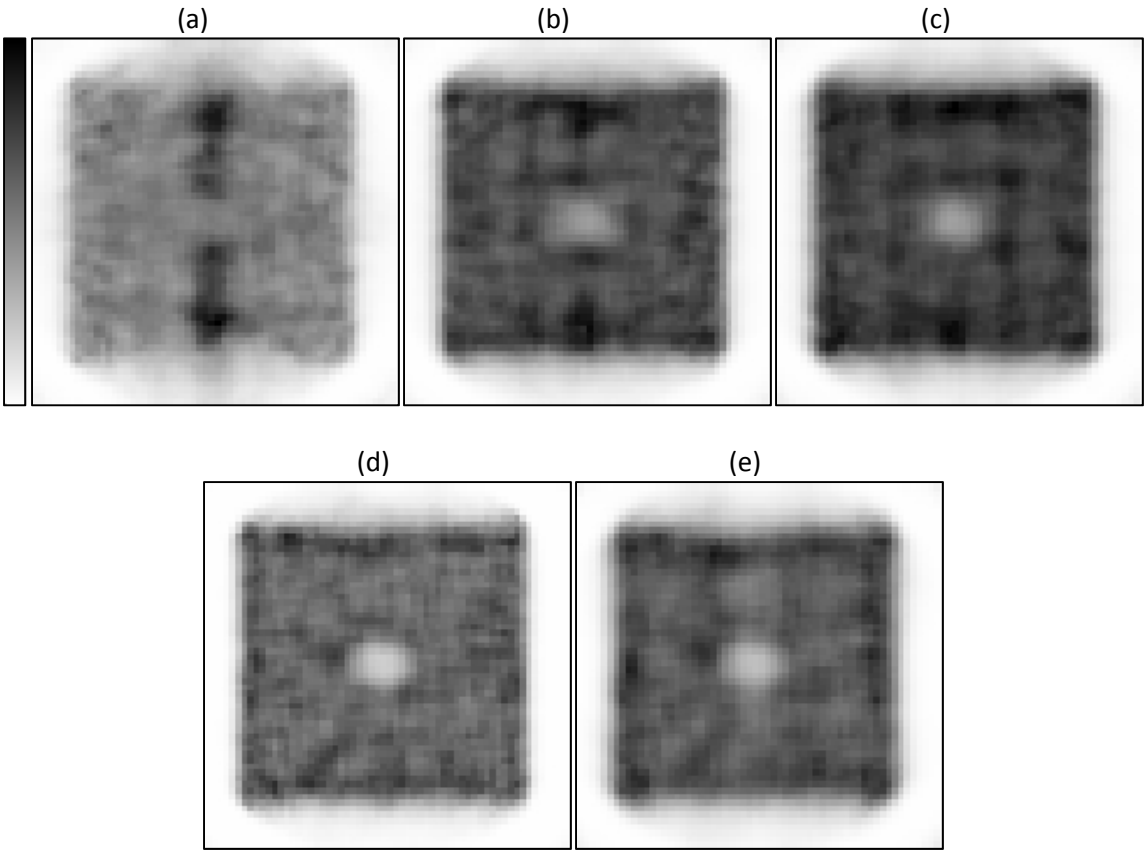

Figure 54: Slices of the Cool Sphere phantom reconstructions with Ge Only OSEM at 9th iteration (a), MLEM Si + Ge at 40th iteration (b), OSEM 1 Phase Si + Ge at 36th update (c), OSEM 2 Phase (4 Si + 4 Ge) at 80th update (d), and OSEM 2 Phase (4 Si + (4 Si + 4Ge)) at 36th update (e).

In all cases where the additional Si projections were included in the reconstruction, the NSD versus NMSE tradeoff curves show improvement over only using Ge projections. This suggests that quantitatively there is an improvement in image quality in the case of the Cool Sphere phantom with the seven-pinhole collimator, with the 2 Phase (4 Si + 4 Ge) reconstruction having, relatively, the best results by visual assessment of the curves. Although the instinctive approach to compare these different reconstructions would involve determining the distance from the comparison iteration's point on the NSD versus NMSE curve, this method is not practical as it requires a way to relate the unit-less NMSE value, which is a measure of accuracy, to the also unit-less NSD value which represents image smoothness. The lack of conversion between these two parameters requires results to be analyzed by visual inspection instead of with quantifiable methods.

Looking at the reconstructed image slices, a reduction in the multiplexing artifacts is seen in the Si + Ge reconstructions over Ge Only, with the 2 Phase reconstructions appearing to have the greatest reduction. Because the 2 Phase (4 Si + (4 Si + 4 Ge)) minimum point occurred before the second phase started, there is little to no multiplexing artifacts, as the highly-multiplexed Ge projections are not included in the reconstruction. Although different objects may result in a different switch-point and minimum NSD versus NMSE point, the reconstruction method is not ideal for the desired two-detector system in this aim.

V.3.2 DPRF with varying reconstruction methods

The DPRF for each reconstruction type and projection combination was calculated, including: Ge Only OSEM (4 Ge), MLEM (Si + Ge), OSEM (4 Si + 4 Ge), OSEM 2 Phase (4 Si + 4 Ge), and OSEM 2 Phase (4 Si + (4Si 4Ge)). The switch-point for the two-phase reconstructions and update number comparison points were the same as used in the Cool Sphere phantom in the section V.3.1, as listed in Table 13.

Slices through the resulting difference images are shown in Figure 55, and line profiles including the obvious artifacts are shown in Figure 56. The results from OSEM 2 Phase (4 Si + (4Si 4Ge)) were not shown as the Ge projections were not included in this reconstruction, and therefore no multiplexing, and subsequently no DPRF artifacts, were present.

The DPRF for each reconstruction option was calculated to allow for a qualitative assessment of multiplexing artifacts. The DPRF image slices (Figure 55) and line profiles (Figure 56) show the effect of the highly-multiplexed Ge projections with the seven-pinhole collimator. The DPRF of an image with little to no multiplexing would result in a reconstruction similar to the original signal-only object (a single point in the center of object space as seen in Figure 51 (c)). All of the DPRF image slices display the same type of artifacts, the high-activity ring of counts around the central signal point, except they vary in magnitude. The magnitude of these artifacts is better seen in the line profiles (Figure 56), where the Si + Ge reconstructions show a decrease in magnitude relative to the Ge Only reconstruction. The two smaller side peaks are the artifact peaks, and the magnitude of the 2 Phase (4 Si + 4 Ge) peaks appear to be slightly lower than the other reconstruction methods.

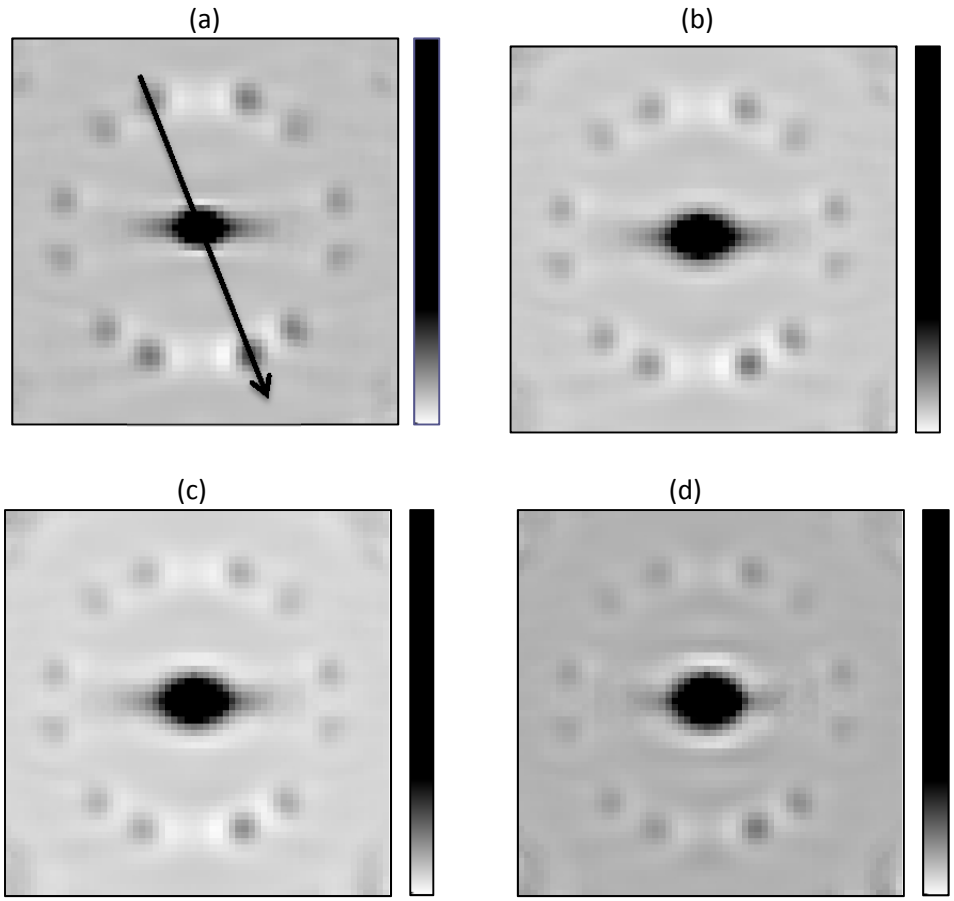

Figure 55: Image slices of the DPRF for each reconstruction type, including the Ge Only OSEM (a), Si+Ge MLEM (b), 1 Phase OSEM (c), and the 2 Phase OSEM (4 Si + 4 Ge) (d). The line in (a) represents the line profiles through each image shown in Figure 56.

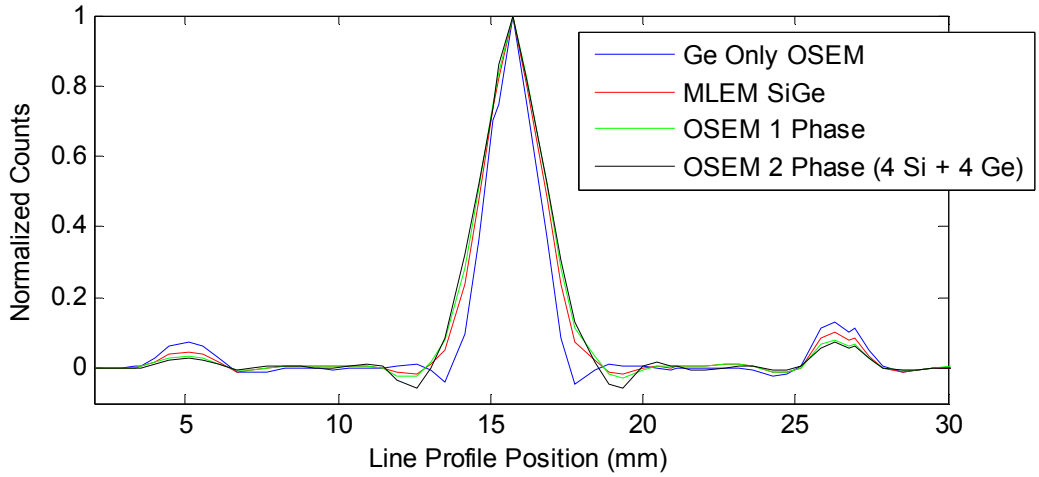

Figure 56: Line profiles through the DPRF slices of the varying reconstructions, including the Ge Only OSEM, Si+Ge MLEM, 1 Phase OSEM, and the 2 Phase OSEM (4 Si + 4 Ge). The line profile acquired for each is shown in Figure 55 (a).

V.3.3 Conclusions

The results of the Cool Sphere NSD versus NMSE show by visual inspection that the 2 Phase (4 Si + 4 Ge) is slightly closer to the origin, and therefore gives better image quality than the other reconstruction algorithms investigated. Visual inspection of the reconstructed images agreed with the quantitative assessment. Additionally, the DPRF showed improvement when using 2 Phase (4 Si + 4 Ge) reconstruction as compared to using Ge alone, and appeared to reduce, if only marginally, the magnitude of the multiplexing artifact peaks relative to the other reconstruction algorithms tested. Because of this, all subsequent simulations were performed using the 2 Phase (4 Si + 4 Ge) reconstruction when both the Si and Ge projections were included, and is referred to as Si + Ge reconstructions in future sections.

V.4 Simulation Part 2: Determine Silicon Parameters

Following the determination of the reconstruction algorithm for the Si + Ge reconstructions, the sensitivity versus resolution tradeoff was investigated in order to determine the Si system parameters. The Si detectors to be utilized in the planned physical system have a strip pitch of 1024 × 1024 with a pixel size of 59 μm. The amount of noise with pixel sizes this small likely would degrade the combined image quality. Additionally, the larger number of pixels slows the total reconstruction size due to the increased system matrix size. Therefore, two different Si projection sizes were tested: 256 × 256 strips (0.234 mm × 0.234 mm) and 512 × 512 (0.117 mm × 0.117 mm).

A second option tested for the Si system configuration utilized the concept of a sandwich pinhole, which is derived from work from previous lab members (McDonald, Shokouhi et al. 2007). As Si detects lower-energy photons, a molybdenum insert can be placed between two layers of tungsten, such that the tungsten pinhole used to stop the higher-energy photons detected by the Ge detector can be one size, and the molybdenum insert makes a smaller pinhole that only stops the lower-energy photons which are detected by the Si detector. Smaller pinholes allow for better spatial resolution but decrease the sensitivity. This set of simulations sought to determine an appropriate system

configuration with respect to sensitivity and spatial resolution by varying the Si detector's pixel dimensions and the diameter of the Si pinhole.

V.4.1 Varying Si Properties in Hot Rod Phantom Reconstructions

The Hot Rod phantom was used for this simulation study as it allows for visual qualitative evaluation of system resolution, while the seven-pinhole collimator was chosen so that the effects of multiplexing would also be included. Twenty noise realizations and one noise-free projection for each 1.0, 0.8, 0.7, 0.5, 0.4 and 0.3 mm pinhole diameters with 256 × 256 and 512 × 512 Si detector pixels were reconstructed using the 2 Phase (4 Si + 4 Ge) method. The switch-point for each of these combinations was determined by calculation of the NSD versus NMSE curve for the Si Only results, and iteration and update that minimized distance to the zero-shifted origin was determined as done in section V.3.1.1. The determined switch-point for each combination is shown in Table 14.

Table 14: Switch-point for Hot Rod object with varying pinhole diameter and Si pixel size

Pinhole Diameter	1 mm		0.8 mm		0.7 mm		0.5 mm		0.4 mm		0.3 mm	
Si Pixels	256	512	256	512	256	512	256	512	256	512	256	512
Iteration	14	11	10	36	7	7	5	4	3	3	2	2
Update	56	44	40	9	28	28	20	16	12	12	8	8

The resulting NSD versus NMSE curves for the Hot Rod phantom with the seven-pinhole collimator are shown in Figure 57. A number of the combinations tested show worse results than with the Ge Only OSEM reconstruction, demonstrating the dominating effect of noise in the Si projections with the finer Si detector resolution and smaller pinholes. The NSD versus NMSE curve shows that Si pinholes of 0.5 mm diameter and smaller perform worse than Ge Only. Figure 57 (b) shows the same results, except with only combinations that have an improved curve over the Ge Only results, which include the 1.0 mm pinhole diameter with a 256 × 256 Si detector, the 1.0 mm pinhole diameter with a 512 × 512 Si detector, the 0.8 mm pinhole diameter with a 512 × 512 Si detector, and the 0.7 mm pinhole diameter with a 512 × 512 Si detector.

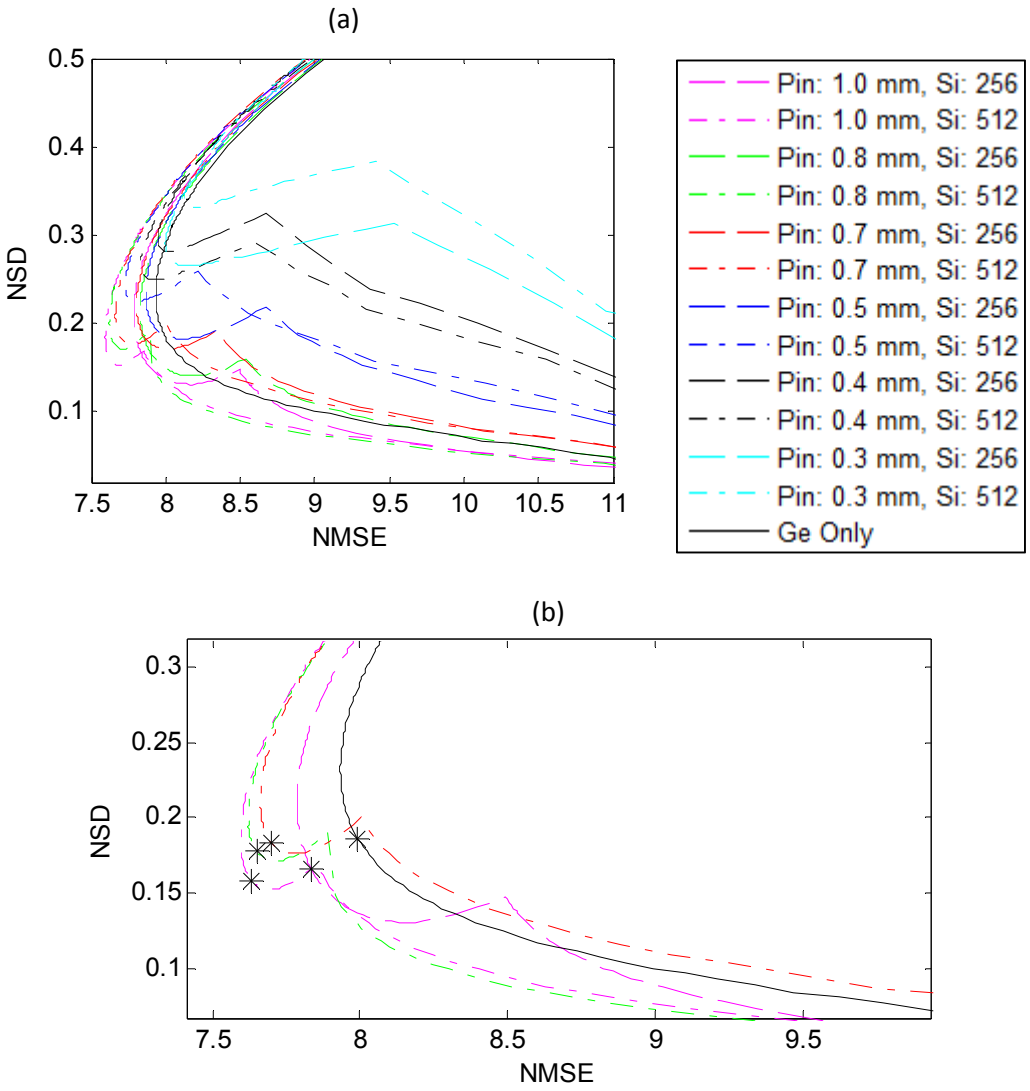

Figure 57: Hot Rod NSD versus NMSE curves for varying Si properties, with (a) showing all combination results and (b) showing the four results with the least distance to the center origin of the NSD versus NMSE plus the Ge Only curve. The '*' symbol indicates the location of each curve's zero-shifted minimum.

As in section V.3.1.1, minimum distance to the zero-shifted origin was determined and rounded to the nearest iteration for each curve, which was subsequently used as a point at which to compare each reconstruction. The resulting optimal iteration number and update number for each curve are shown in Table 15. By visual inspection of the minimum points (indicated by *) in Figure 57 (b), the 1 mm diameter pinhole with the 512 × 512 pixel detector appears to be closest to the origin.

Table 15: Iteration comparison point for Hot Rod reconstructions

Pinhole Diameter	1 mm		0.8 mm		0.7 mm		0.5 mm		0.4 mm		0.3 mm		Ge Only
Si Pixels	256	512	256	512	256	512	256	512	256	512	256	512	NA
Iteration	22	16	18	15	14	13	13	11	11	11	11	11	12
Update	88	64	72	60	56	52	52	44	44	44	44	44	48

Slices from selected images at the comparison iteration are shown in Figure 58, which show the expected trend of an increase in spatial resolution as the pinhole used becomes smaller and finer Si pixel dimensions are used, until the noise is too high and image reconstructions become dominated by noise (Figure 58 (f)). To give perspective, example reconstructions of the noise-free projections, shown in Figure 59, show the resolution gained by the smaller pinhole without the noise effects due to loss of sensitivity. These noise-free projections continue to improve in resolution past the comparison point determined for their noisy counterparts, and show an improved resolution the longer they are iterated, (Figure 59 (a) to (b)), but still show a slight overall improvement in resolution between the 1 mm pinhole 256 × 256 Si pixel case and the 0.3 mm pinhole 512 × 512 pixel case (Figure 59 (b) to (c)).

As expected, the smaller the pinhole size used for the Si reconstruction, the better the spatial resolution. The resolution is also improved as the Si detector is changed from 256 × 256 to 512 × 512. But this improvement increases the amount of noise present in images, to the point where including the Si projections in the Ge reconstruction actually lowers image quality, as seen on the NSD versus NMSE curves. These results eliminated potential Si configurations that did not improve image quality relative to the Ge Only reconstruction. When noise-free projections are reconstructed, the increase in spatial resolution can be seen without the noise induced by a decrease in sensitivity. In NSD versus NMSE plot, the 1.0 mm pinhole diameter with the 512 × 512 Si pixels appears to be closer to the origin than the other options investigated.

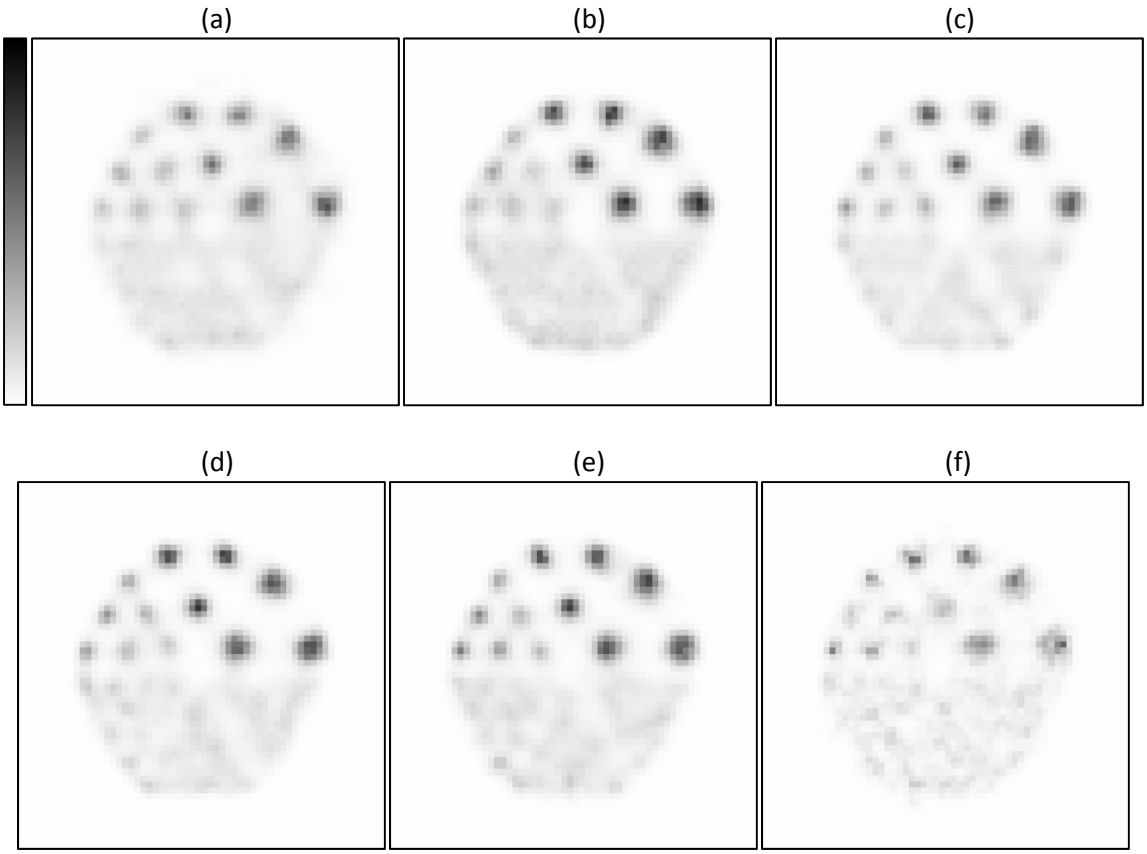

Figure 58: Slices from the noisy Hot Rod phantom reconstructions, from Ge Only (a), and Si + Ge of 1 mm pinhole with 256 × 256 Si pixels (b), 1 mm pinhole with 512 × 512 Si pixels (c), 0.8 mm pinhole with 512 × 512 Si pixels (d), 0.7 mm pinhole with 512 × 512 Si pixels (e), and 0.3 mm pinhole with 512 × 512 Si pixels (f).

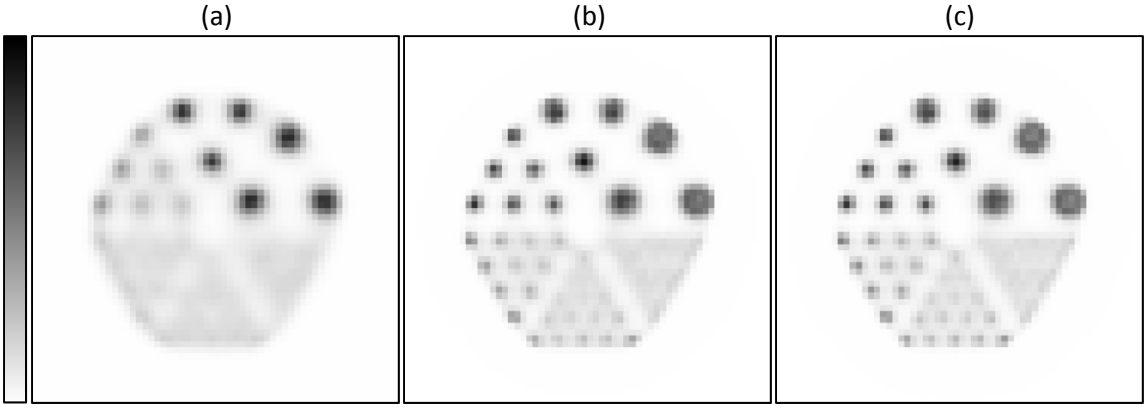

Figure 59: Example of noise-free reconstructions of the Hot Rod phantom with the 1 mm pinhole and 256 × 256 Si pixels at the original comparison iteration of 44 updates and 11 iterations (a) and at 400 updates and 100 iterations (b), and the 0.3 mm pinhole with 512 × 512 Si pixels at 400 updates and 100 iterations (c).

V.4.2 Varying Si Properties in Altered-NEMA Phantom Reconstructions

To gain additional perspective on image quality, reconstructions of the Altered-NEMA phantom were also performed. Only the Si configurations that performed better than Ge Only for the Hot Rod reconstructions in section V.4.1 were included in this simulation. Twenty noise realizations and one noise-free reconstruction were run for the 256 × 256 Si detector pixels with 1 mm pinholes, 512 × 512 Si detector pixels with 1 mm pinholes, 512 × 512 Si detector pixels with 0.8 pinholes, and 512 × 512 Si detector pixels with 0.7 mm pinholes. The switch-points were determined using the same method as previously described in section V.3.1.1, and are listed below in Table 16. The NSD versus NMSE graphs were calculated, in addition to a comparison of the quantitative NEMA metrics described in section IV.5.2.2.

Table 16: Switch-Point for Altered-NEMA phantom

Pinhole Diameter	1 mm	1 mm	0.8 mm	0.7 mm
Si Pixels	256	512	512	512
Iteration	9	6	5	4
Update	36	24	20	16

The resulting NSD versus NMSE curve for the Altered-NEMA reconstruction of Ge Only, and the Si + Ge with varying Si parameters are shown in Figure 60. Visual inspection shows that the 1.0 mm pinhole with 256 × 256 Si pixels and the 1.0 mm pinhole with 512 × 512 Si pixels are the closest to the NSD versus NMSE origin. Table 17 shows the iteration and update number of the minimum distance to each curve's zero-shifted origin that is used as a comparison point.

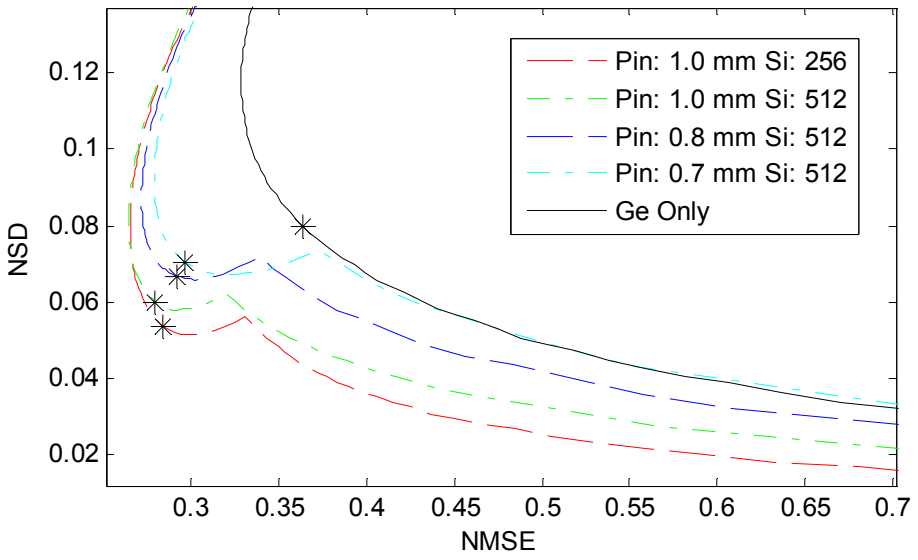

Figure 60: NSD versus NMSE of the Altered-NEMA with Ge Only, and Si + Ge reconstructions of 1 mm pinhole with 256 × 256 Si pixels, 1 mm pinhole with 512 × 512 Si pixels, 0.8 mm pinhole with 512 × 512 Si pixels, and 0.7 mm pinhole with 512 × 512 Si pixels. The '*' indicates the location of the minimum distance to the zero-shifted origin.

Table 17: Comparison points for Altered-NEMA phantom

Pinhole Diameter	1 mm	1 mm	0.8 mm	0.7 mm	Ge Only
Si Pixels	256	512	512	512	NA
Iteration	12	9	8	8	9
Update	48	36	32	32	36

Slices of the reconstructed images at the determined comparison points are shown in Figure 61, which qualitatively show little difference in image quality between the varying Si properties, with the exception of a slight increase in the magnitude of noise in the uniform region as the pinholes become smaller. To better understand these changes, the same NEMA quantitative procedure performed in section IV.5.2.2 was applied to the Altered-NEMA phantom and the results are shown in Table 18. These quantitative measures show that all Si + Ge options shown in Figure 61 have better uniformity than the Ge Only reconstruction, with the $\%STD_{unif}$ becoming slightly worse the smaller the pinhole used. The same trend holds true for the SOR into the cold cylinder while the RC of the rods show mixed trends.

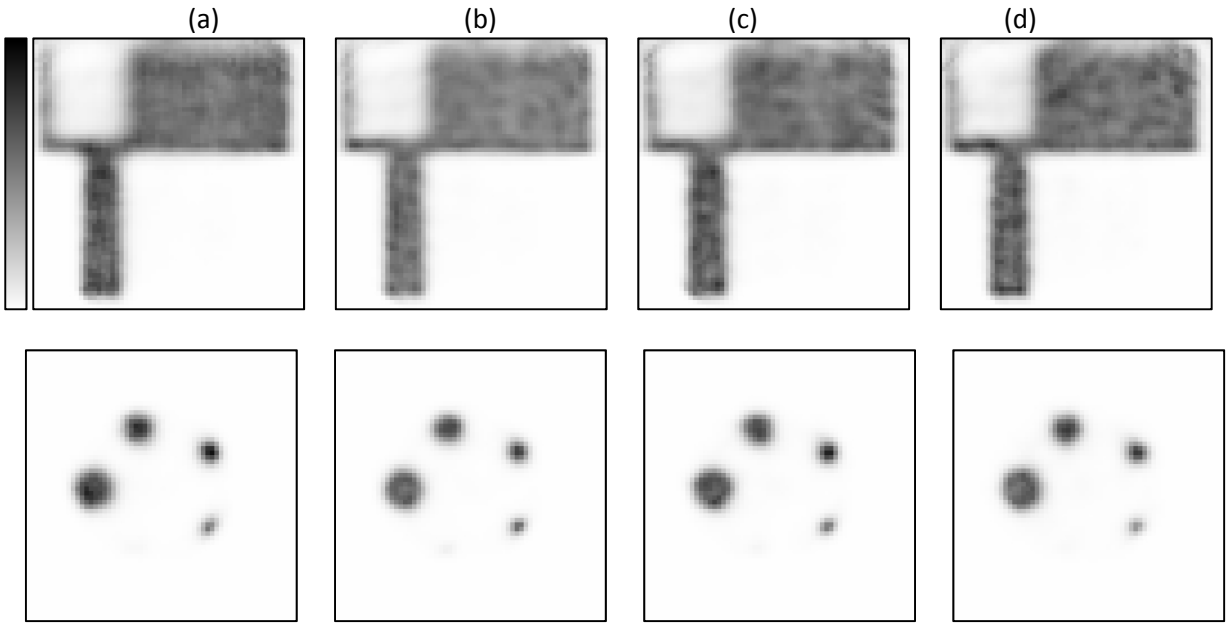

Figure 61: Reconstructed image slices of the Altered-NEMA phantom with Si + Ge reconstructions of 1 mm pinhole with 256 × 256 Si pixels (a), 1 mm pinhole with 512 × 512 Si pixels (b), 0.8 mm pinhole with 512 × 512 Si pixels (c), and 0.7 mm pinhole with 512 × 512 Si pixels (d).

Table 18: Quantitative results of Altered-NEMA phantom

		Ge Only	Pin: 1.0 mm Si: 256 × 256	Pin: 1.0 mm Si: 512 × 512	Pin: 0.8 mm Si: 512 × 512	Pin: 0.7 mm Si: 512 × 512
Uniformity	$\%STD_{unif}$	13.97	6.65	7.57	8.46	8.67
SOR	SOR	0.12	0.07	0.09	0.10	0.10
	$\%STD_{SOR}$	31.00	38.71	40.02	38.54	39.19
RC	5 mm	1.15	1.25	1.23	1.23	1.21
	$\%STD_{RC}$	89.21	22.61	36.70	24.50	39.70
	4 mm	1.19	1.45	1.38	1.33	1.31
	$\%STD_{RC}$	89.55	23.62	36.47	26.42	39.83
	3 mm	1.27	1.58	1.54	1.59	1.55
	$\%STD_{RC}$	92.40	23.44	36.35	25.04	39.71
	2 mm	0.91	1.02	1.12	0.92	0.92
	$\%STD_{RC}$	106.21	27.29	36.75	27.21	47.41
	1 mm	0.12	0.11	0.11	0.10	0.09
	$\%STD_{RC}$	110.75	98.13	80.41	63.60	69.99

The Altered-NEMA NSD versus NMSE curves show a slightly different response than the Hot Rod results, with the 1.0 mm pinhole diameter and the 256 × 256 Si pixels appearing to be slightly better than that of the 1.0 mm pinhole diameter and the 512 × 512 Si pixels. Given that the Altered-NEMA phantom has regions where the spatial resolution is

less important (uniform region and cold cylinder), this result is not surprising. The quantitative results show that the images have less uniformity as the pinhole size decreases, but the pinhole sizes investigated in this section all had better uniformity than the Ge Only reconstruction. In the case of the larger rods (5 mm to 3 mm), the addition of Si projections increases the rod RCs, while in the smaller diameter rods the RCs remain approximately the same.

V.4.3 Varying Si Properties in DPRF

The DPRF was determined for the same set of pinhole diameter and Si detector pixels as shown in Table 14, where the Hot Rod switch point was used, since the DPRF does not include any noise realizations in order to be able to determine its own NSD versus NMSE curve. Although the optimal switch-point varies between different object types, the Hot Rod points were chosen in this case and a discussion and alternative method for choosing the switch-point is addressed in section V.5.2.

The DPRF gives insight into the multiplexing artifacts of a particular system configuration, which is dependent on the system's spatial resolution and its spatial sensitivity instead of on the effect of noise. Figure 62 shows a select number of the DPRF combinations which were computed using the Hot Rod switch point in Table 14, and are compared at the iteration and update number listed in Table 15 that was determined to minimize the zero-shifted distance to the origin of the NSD versus NMSE curve. The influence of resolution on the DPRF's signal spot size is clearly seen, as the smallest pinhole's spot size (Figure 62 (d)) is noticeably smaller than the spot size of the 1 mm pinhole with 256 × 256 Si pixels (Figure 62 (b)). To give better perspective on the effect of the resolution on multiplexing artifacts, line profiles through the artifact regions, as indicated in Figure 62 (a), are shown in Figure 63.

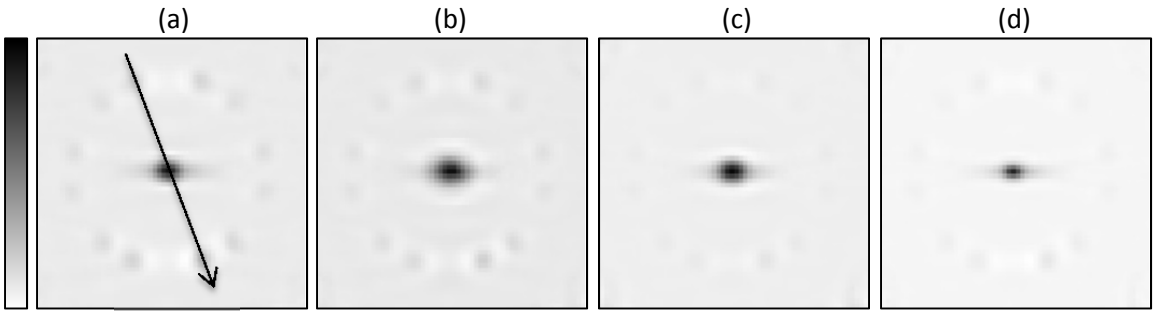

Figure 62: Example DPRF images with varying Si pinhole and detector resolutions, with Ge Only (a), and Si + Ge for 1 mm pinhole with 256 × 256 Si pixels (b), 1 mm pinhole with 512 × 512 Si pixels (c), 0.3 mm pinhole with 512 × 512 Si pixels (d). The arrow in (a) represents the path of the line profile used in Figure 63.

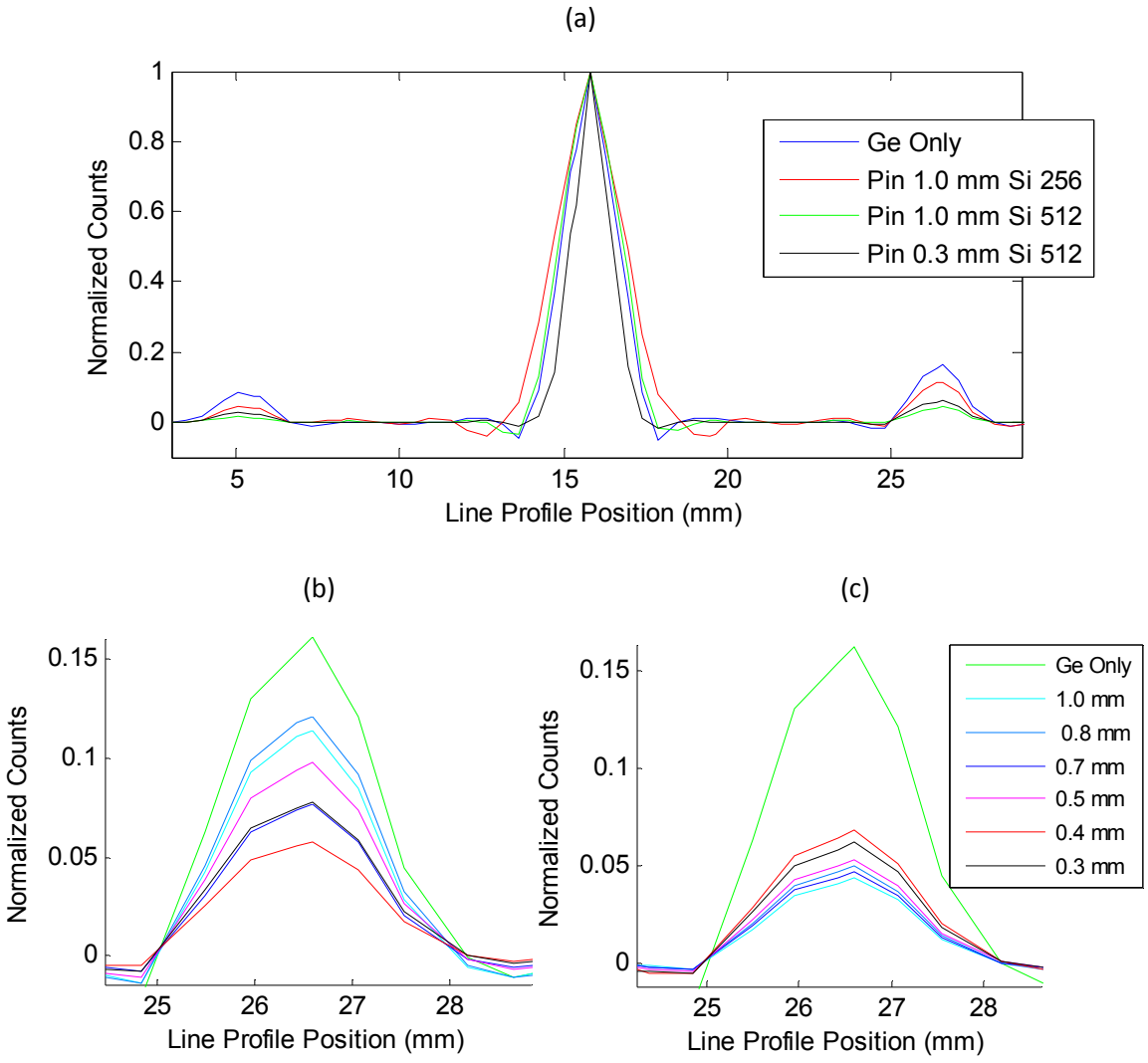

Figure 63: Line profiles through the DPRF of varying Si pinhole and detector sizes, with (a) showing the line profile of the results in Figure 62 with (b) and (c) showing a zoomed axis with DPRF results of the 256 × 256 and 512 × 512 Si pixel cases, respectively.

The resulting DPRF line profiles in Figure 63 give perspective on how spatial resolution can help to compensate for multiplexing artifacts. In (a) it can be seen that the narrowest signal peak is obtained by the best spatial resolution combination of the 0.3 mm pinhole 512 × 512 Si pixel case. The 1 mm 256 × 256 Si pixel case shows a broadening of this peak. The overall system resolution (R_{TOT}, Equation 2), is dependent on the detector resolution (R_d), where it is normalized by the system magnification. As discussed in section V.2.1, the magnification of the Si and Ge detector is 0.5 and 1.75, respectively, which gives the R_d/M term in Equation 2 as 0.468 and 0.234 mm for the 512 × 512 and 256 × 256 Si pixel cases, respectively, and 0.285 for the Ge detector. Although in actual systems the detector resolution is generally larger (or worse) than the detector pixel size, in these simulations detector resolution was not modeled, and therefore the detector pixel size determines the detector resolution. These DPRF results reflect the intuitive change between having a magnification-normalized detector resolution worse than that of the Ge projections with the 256 × 256 case to being slightly better with the 512 × 512 case. Although the total resolution (Equation 2) is highly dominated by the much larger R_g, these results show that decreasing R_d/M from 0.468 to 0.234 increases the reconstruction algorithm's ability to compensate for multiplexing artifacts while helping to maintain (and not worsen) the overall resolution. In the zoomed-in axis it can be seen that the majority of the results with 512 × 512 Si pixels are clustered very close together, while the 256 × 256 Si pixel with the 1 mm diameter is much closer to the Ge Only peak height. This result again shows that there will be better image quality in highly-multiplexed projections with the better resolution detector.

V.4.4 Conclusions

The results from the Hot Rod and Altered-NEMA phantom show that the noise to resolution tradeoff difference is very close between the 1 mm pinhole 256 × 256 Si pixel case and the 1 mm pinhole 512 × 512 Si pixel, with the Altered-NEMA having slightly better results with the former and the Hot Rod the latter. The DPRF clearly shows that higher Si pixel dimensions help to better reduce multiplexing artifacts. Because of these reasons, the Si configuration used in the final set of simulations was chosen to be the 1 mm pinhole with the 512 × 512 Si pixel dimensions.

V.5 Simulation Part 3: Varying Objects with Varying Multiplexing

V.5.1 Object Dependence of Multiplexing

The two-phase OSEM reconstruction with 4 Si subsets followed by 4 Ge subsets was used with a 1-mm pinhole diameter and 512 × 512 Si detector pixels for all four object types: Cold Rod, Cool Sphere, Hot Rod, and Altered-NEMA. Twenty noise realizations were reconstructed for each phantom and one noise-free instance with each of the three pinhole collimators, p4LM, p4HM, p7, as shown in Figure 49. The same combinations were reconstructed for the Ge Only OSEM (4 subsets) case as well. Following the same methods as in section V.3 and V.4, the switch-point for the two-phase reconstruction was determined, with the iteration and update number for each of the pinhole and object combinations shown in Table 19.

Table 19: Two-phase reconstruction switch-point for each object and pinhole combination

	Cold Rod		**Cool Sphere**		**Hot Rod**		**Altered-NEMA**	
	Iteration	Update	Iteration	Update	Iteration	Update	Iteration	Update
p4 LM	3	12	3	12	6	24	3	12
p4 HM	4	16	3	12	7	28	3	12
p7	8	32	7	28	11	44	6	24

The NSD versus NMSE curves for each object are shown in Figure 64. It can be seen, even in the low multiplexing p4LM case, that the addition of the Si projections into the reconstructions results in more accurate, less noisy images than with reconstructions based on Ge projections alone. The resulting optimal iteration stopping points for each pinhole and object combination are shown in Table 20.

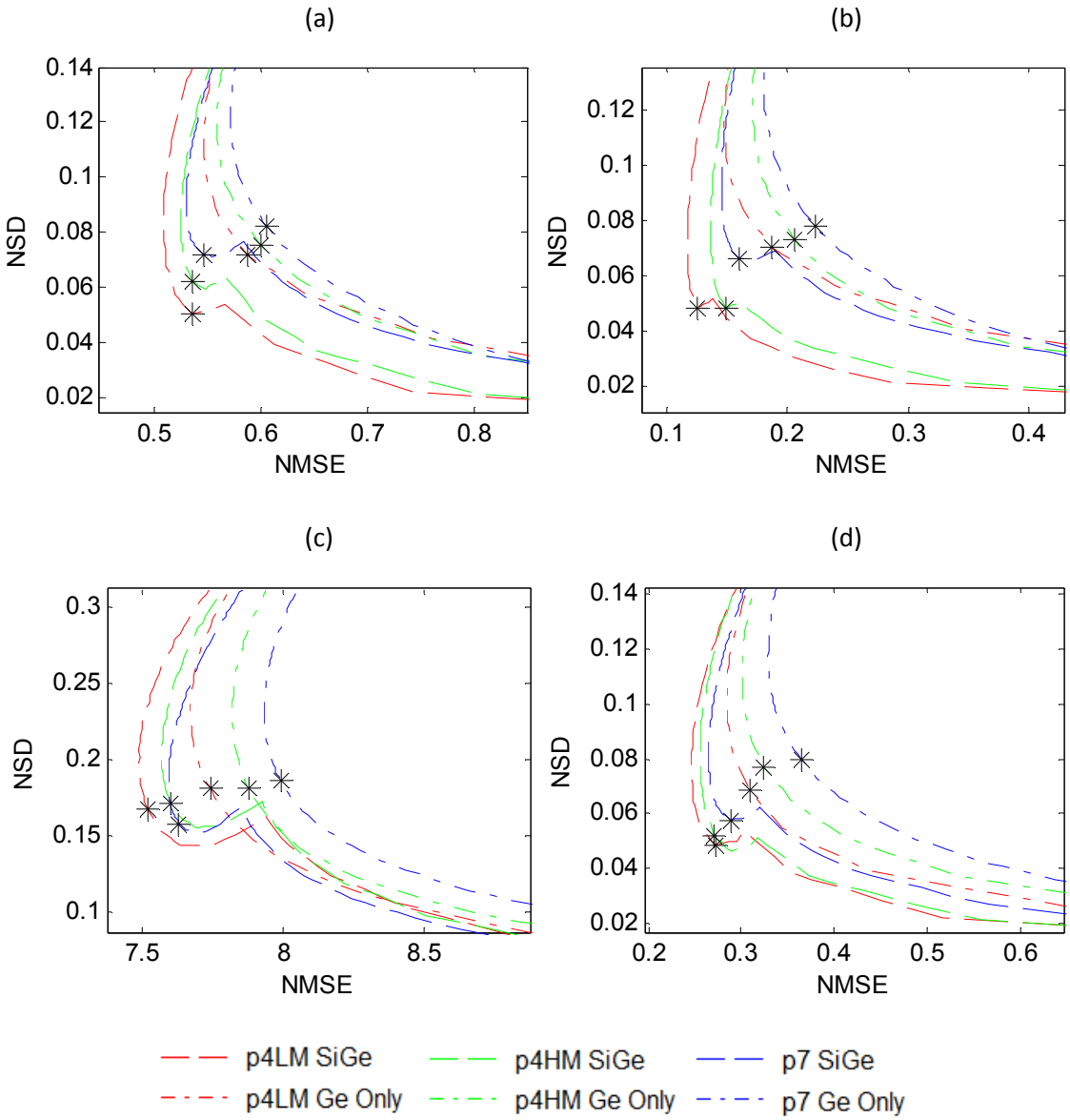

Figure 64: NSD versus NMSE for Cold Rod (a), Cool Sphere (b), Hot Rod (c), and Altered-NEMA (d) phantoms for each pinhole combination and for Ge Only and the combined Si + Ge reconstruction.

Table 20: Iteration stopping point for all object-pinhole combinations

	Si + Ge		Ge Only	
	Update	**Iteration**	**Update**	**Iteration**
Cold Rod				
p4LM	16	4	16	4
p4HM	24	6	20	5
p7	44	11	40	10
Cold Sphere				
p4LM	16	4	16	4
p4HM	16	4	20	5
p7	40	10	36	9
Hot Rod				
p4LM	40	10	24	6
p4HM	44	11	28	7
p7	64	16	48	12
Altered-NEMA				
p4LM	16	4	16	4
p4HM	20	5	20	5
p7	36	9	36	9

Resulting images of the Cold Rod phantom are shown in Figure 65. The addition of the Si projections appears to increase the ability to resolve the cold regions in the lowest multiplexing case, Figure 65(a) compared to (d). The highest multiplexing case, Figure 65(c) compared to (f), shows that the addition of the Si projections helps to lower the intensity of the hot artifact at the center of the slices, and subsequently gives better contrast between hot background and cold rods.

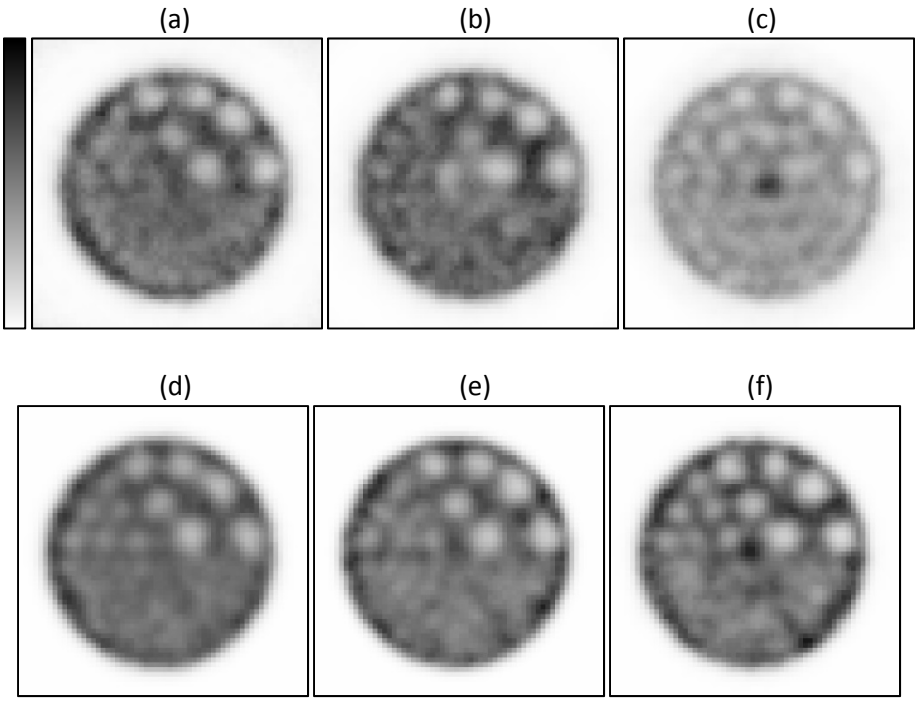

Figure 65: Cold Rod reconstructions at the iteration stopping point, showing p4LM (a), p4HM (b), and p7 (c) Ge Only slices and p4LM (d), p4HM (e), and p7 (f) Si + Ge slices.

The Cool Sphere reconstructions also show significant artifacts, as seen in Figure 66. The low-multiplexing case of p4LM shows little difference between images except for the Si + Ge appearing to have slightly lower noise, but in the p4LM and p7 cases where higher amounts of multiplexing are present, it can be seen that the addition of the Si projections compared to Ge Only reconstructions helps to significantly reduce artifacts. This is especially true in the p7 case, where the artifact causes the cool sphere at the center of the object to have roughly the same intensity as the hot background, while in the Si + Ge case, the cool sphere is better resolved.

To quantify the accuracy of activity inside the cool sphere region in the center of the phantom, a spherical ROI with a ∼2.5 mm diameter was drawn inside of the cool sphere region and a cylindrical ROI of ∼5 mm diameter and ∼10 mm height through the uniform hot background section (avoiding multiplexing artifacts) of a single noisy reconstruction of each pinhole type. The ratio of the mean of the cool sphere ROI to the mean of the background ROI was determined for each reconstruction, with the results shown in Table 21. The actual activity ratio in the Cool Sphere to background is

30%, which shows that both reconstructions perform equally in the p4LM case, while the Si + Ge over-estimates the activity compared to Ge Only in the p4HM case, but performs significantly better in the p7 case.

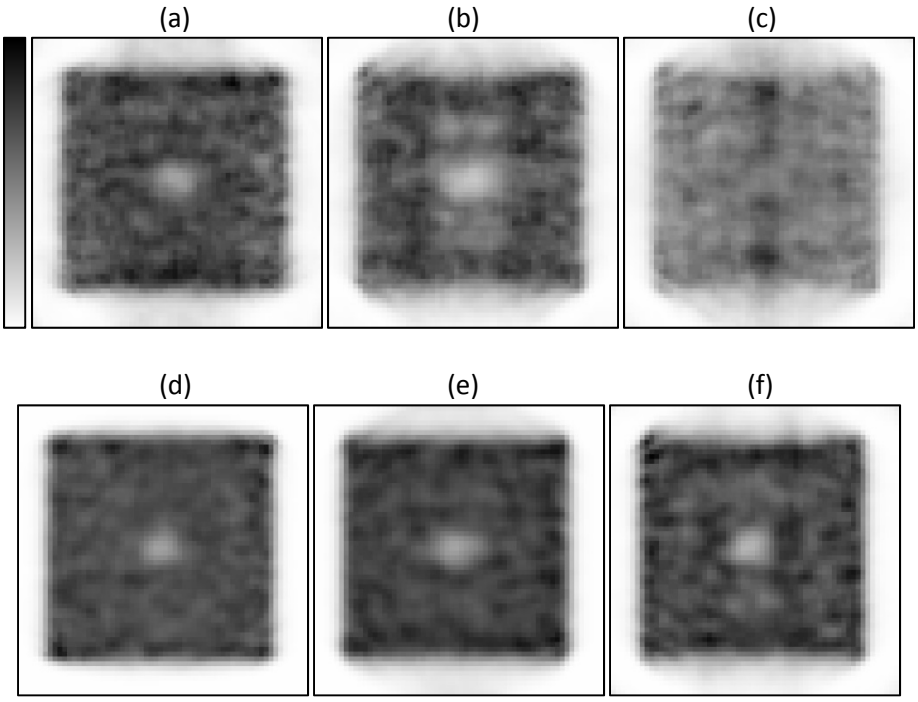

Figure 66: Cool Sphere reconstructions at the iteration stopping point, showing p4LM (a), p4HM (b), and p7 (c) Ge Only slices and p4LM (d), p4HM (e), and p7 (f) Si + Ge slices.

Table 21: Ratio of mean background to mean cool sphere activity

4pLM		p4HM		p7	
Ge	**Si + Ge**	**Ge**	**Si + Ge**	**Ge**	**Si + Ge**
53.41%	55.13%	35.95%	50.31%	104.50%	42.01%

The Hot Rod phantom reconstructions have little to no multiplexing artifacts even in the highly-multiplexing seven-pinhole case, and therefore resulting images are not shown here, but examples of these reconstructions are shown in section V.4.1 Figure 58 and Figure 59. The Altered-NEMA phantom also exhibits minimal multiplexing artifacts, only displaying a slight increase in activity in the center of the uniform region similar to that of the Cool Sphere artifact except to a lesser degree, and are only present in the highly multiplexing seven-pinhole case, therefore examples are not shown.

Although the NEMA phantom did not have many obvious multiplexing artifacts, it is possible for multiplexing to alter the image quality. To investigate this, the same procedure for quantification described in section IV.5.2.2 and used in section V.4.2 was applied to the determined iteration stopping point of the Ge Only and the Si + Ge reconstructions for all three pinhole types. The results of this quantification are shown in Table 22.

Table 22: Quantification of Altered-NEMA phantom for varying multiplexing

		p4 LM		p4HM		p7	
		Ge Only	**Si + Ge**	**Ge Only**	**Si + Ge**	**Ge Only**	**Si + Ge**
Uniformity	$\%STD_{unif}$	7.58	5.02	9.28	6.00	13.97	7.57
SOR	SOR	0.12	0.13	0.12	0.12	0.12	0.09
	$\%STD_{SOR}$	31.08	30.67	42.99	38.09	31.00	40.02
RC	5 mm	1.21	1.22	1.23	1.29	1.15	1.23
	$\%STD_{RC}$	36.29	17.57	38.18	36.55	89.21	36.70
	4 mm	1.25	1.34	1.26	1.33	1.19	1.38
	$\%STD_{RC}$	37.80	17.45	37.96	36.56	89.55	36.47
	3 mm	1.42	1.50	1.33	1.49	1.27	1.54
	$\%STD_{RC}$	36.66	17.81	38.28	37.60	92.40	36.35
	2 mm	1.08	1.18	0.79	1.14	0.91	1.12
	$\%STD_{RC}$	41.32	18.62	48.95	36.84	106.21	36.75
	1 mm	0.08	0.18	0.08	0.19	0.12	0.11
	$\%STD_{RC}$	55.90	37.08	60.90	42.38	110.75	80.41

As Mok et al. concluded, multiplexing artifacts are highly dependent on the activity distribution of the object (Mok, Tsui et al. 2011). This study investigated a variety of object distributions, including those that Mok et al used, in addition to adding the Altered-NEMA phantom. These activity distributions, which include cold backgrounds, hot backgrounds, high-contrast distributions, and a mix of each in the Altered-NEMA, cover the broad spectrum of distributions likely in small-animal imaging. Qualitatively, in all cases where multiplexing artifacts were clearly visible (Cool Sphere and Cold Rod phantoms) the additional Si projections in the reconstruction either eliminated or reduced the visibility of the artifact. Quantitatively, the NSD versus NMSE curves show that at the determined iteration stopping point, the Si + Ge reconstructions provided improved image quality when compared to their Ge Only counterparts.

The Altered-NEMA phantom allows for quantitative evaluation of changes in image quality due to multiplexing. The results in Table 22 show that in every pinhole case, the addition of the Si projections decreases the $\%STD_{unif}$, giving

better uniformity, while maintaining approximately the same SOR in all cases. The rod RCs for all reconstructions show that the 1 mm rod is not resolvable, and show the same trends as in the results from section V.4.2. Overall, adding Si projections into reconstructions results in higher rod RCs, even though in some cases the rod RCs are greater than one.

V.5.2 DPRF

The DPRF was also determined for each pinhole combination, but as the switch-point for each pinhole type is highly dependent on the object type (demonstrated by the varying switch-points in Table 19), a slightly different approach was necessary. If the objects are grouped into two types: (1) high contrast consisting of the Hot Rod phantom, and (2) standard contrast consisting of the Cold Rod, Cool Sphere, and Altered-NEMA, then estimates of the optimal reconstruction switch-point can be determined by averaging the switch-points determined in Table 19. In this case, Table 23 shows the determined switch-points of the standard contrast and high contrast objects. The DPRFs in this section were determined for both the standard contrast and high contrast object switch-points. The same method was used to determine a stopping point for each pinhole and general object type using the results presented in Table 20, with results being shown in Table 24.

Table 23: General two-phase reconstruction switch-points

	Standard Contrast		**High Contrast**	
	Iteration	Update	Iteration	Update
p4LM	3	12	6	24
p4HM	4	16	7	28
p7	7	28	11	44

Table 24: General two-phase reconstruction comparison point

	Standard Contrast		**High Contrast**	
	Iteration	Update	Iteration	Update
p4LM	4	16	10	40
p4HM	5	20	11	44
p7	10	40	16	64

Although the DPRF was determined from both the standard contrast and high contrast object, only the high contrast results are presented here. The DPRF task of resolving a single point of activity can be considered a high

contrast task, and therefore is more applicable in this case. The resulting DPRFs for Ge Only or Si + Ge reconstruction are shown in Figure 67, Figure 68, and Figure 69 for the p4LM, p4HM, and p7 collimators.

In the lowest multiplexing case, there are few artifacts shown in the DPRF, and the line profiles between the Ge Only and Si + Ge reconstruction show little difference. In both the p4HM and p7 case, the line profiles through the multiplexing artifacts show a decrease in the artifact peak's normalized intensity in the Si + Ge case relative to the Ge Only reconstruction. These decreases demonstrate the advantage of the addition of the Si projections to highly multiplexed Ge projections.

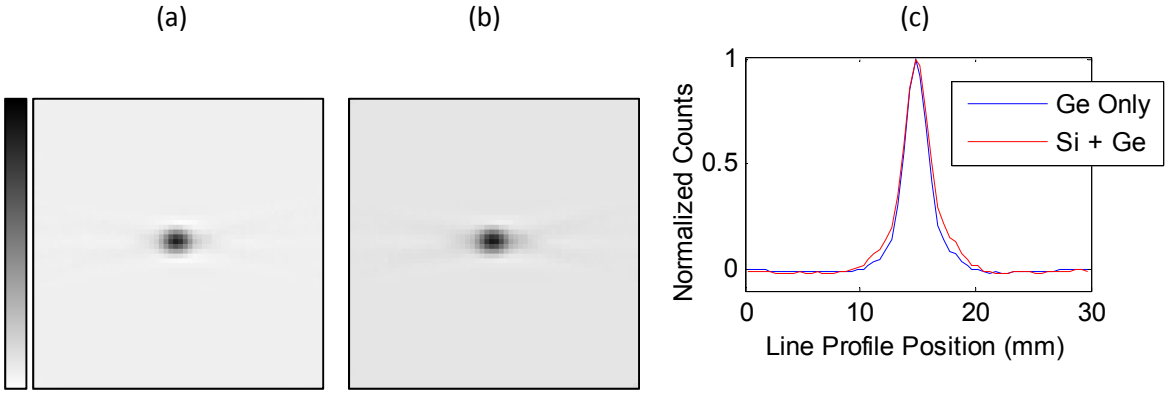

Figure 67: The p4LM DPRF results are shown , with (a) and (b) showing the high contrast update version of the Ge Only and Si + Ge reconstructions, respectively and (c) show the resulting line profiles of 180° through the center of the image slices.

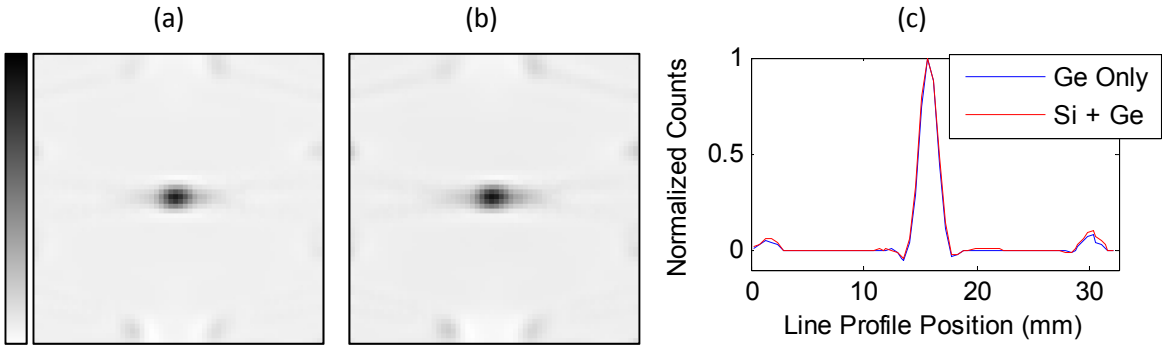

Figure 68: The p4HM DPRF results are shown , with (a) and (b) showing the high contrast update version of the Ge Only and Si + Ge reconstructions, respectively and (c) show the resulting line profiles of -71° through the center of the image slices.

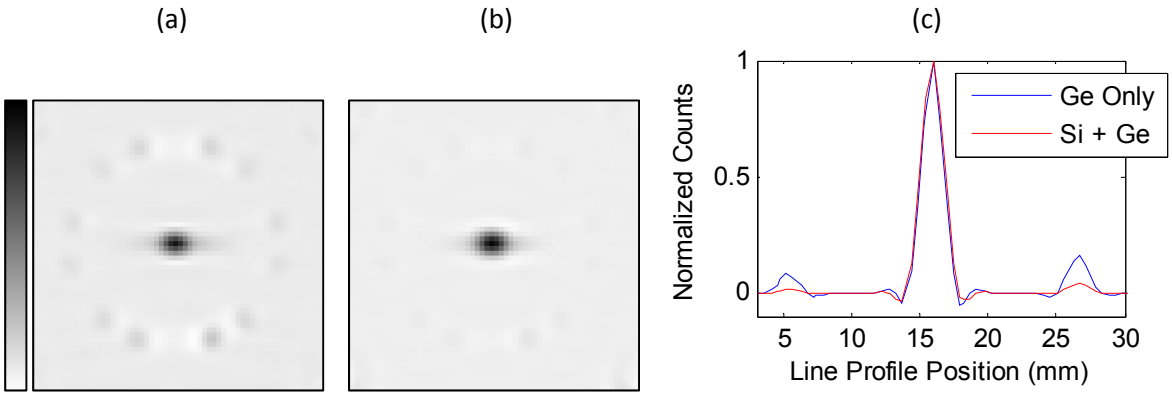

Figure 69: The p7 DPRF results are shown , with (a) and (b) showing the high contrast update version of the Ge Only and Si + Ge reconstructions, respectively and (c) show the resulting line profiles of -68° through the center of the image slices.

V.6 Discussion

The goal of this aim was to determine via simulation the feasibility of using low-multiplexed Si projections in combination with highly-multiplexed Ge projections in order to reduce artifacts in reconstructed images. A system configuration was chosen such that the magnifications allowed for different amounts of multiplexing to be investigated. From the first set of simulations, we determined a reconstruction algorithm that combined Si and Ge projections in a way that allowed for better reconstructed image quality. We determined the configuration of the Si detector and pinhole that balanced the noise to resolution tradeoff while keeping the reconstruction's ability to reduce multiplexing artifacts in the second set of simulations. The final simulations investigated a variety of object types and pinhole configurations to determine whether the addition of Si projections reduces multiplexing artifacts.

Of the objects simulated, the Cool Sphere and Cold Rod objects had the most visible multiplexing artifacts, especially in the highly multiplexing seven-pinhole collimator case. Both of these artifacts were reduced, interpreted visually and through the NSD versus NMSE curves, in the Si + Ge case compared to Ge Only. The DPRF allows for simple visual interpretation of multiplexing artifacts for a given system configuration, and also showed a decrease in image artifacts when the Si + Ge case was compared to Ge Only. These results show that a combined Si-HPGe system has the potential to improve image quality over a highly multiplexing Ge system alone.

The choice of iteration at which to switch between phases of the reconstructions and for the comparison point was determined by having prior knowledge of the object's activity distribution, which is not available in real-world applications. As presented in the section V.5.2, the results of these simulations can be used to estimate more general reconstruction protocols that can have pre-defined switch-points and stopping iterations based on general knowledge of the subject being imaged. This generalization could include options as described above – general contrast or high contrast – or could be set depending on desired noise-resolution tradeoffs. To better understand the influence of choosing a less than ideal stopping point, we can compare, by visual inspection, how image quality changes before or after the chosen stopping point in the simulation results. Figure 70 shows the image quality of both the Ge only reconstructions and the two-phase Si and Ge reconstructions before, at, and after the determined ideal stopping point in the cool sphere phantom with the seven pinhole collimator. This figure shows that in the Ge Only case, varying the stopping point leads to a tradeoff between the severity of the multiplexing artifact and the amount of noise in the image. In the Si + Ge case, the response is similar, where the first phase Si Only input has a slight multiplexing artifact (the cool-regions above and below the cool sphere), that are eliminated by the chosen stopping point in the second phase (Figure 70 (f)). Further iterations beyond this point increase in noise, and do not show a re-emergence of the multiplexing artifacts. This indicates that as long as several iterations of the second phase of the reconstruction are implemented, the choice of the stopping point becomes one of a noise limitation, which is the same challenge as a traditional single-detector reconstruction, as discussed in section II.2.3.2.

Given the improvements seen in image quality in this study, the next phase of this project will be to build a stacked Si-HPGe system. This will allow for experimental validation of these simulation results. Some portions of the system design will be modified, such as having a smaller Ge detector size, but this should not alter the main conclusions of this study. The physical system will involve using the collimator from section IV.2 to attach the Si detector to the Ge detector to allow for simultaneous imaging. Future work will also involve determining optimal collimator designs, as this simulation study did not explore pinhole design in detail and only provides proof-of-principle that additional information from low multiplexed Si projections can improve the reconstructions of highly multiplexed Ge projections.

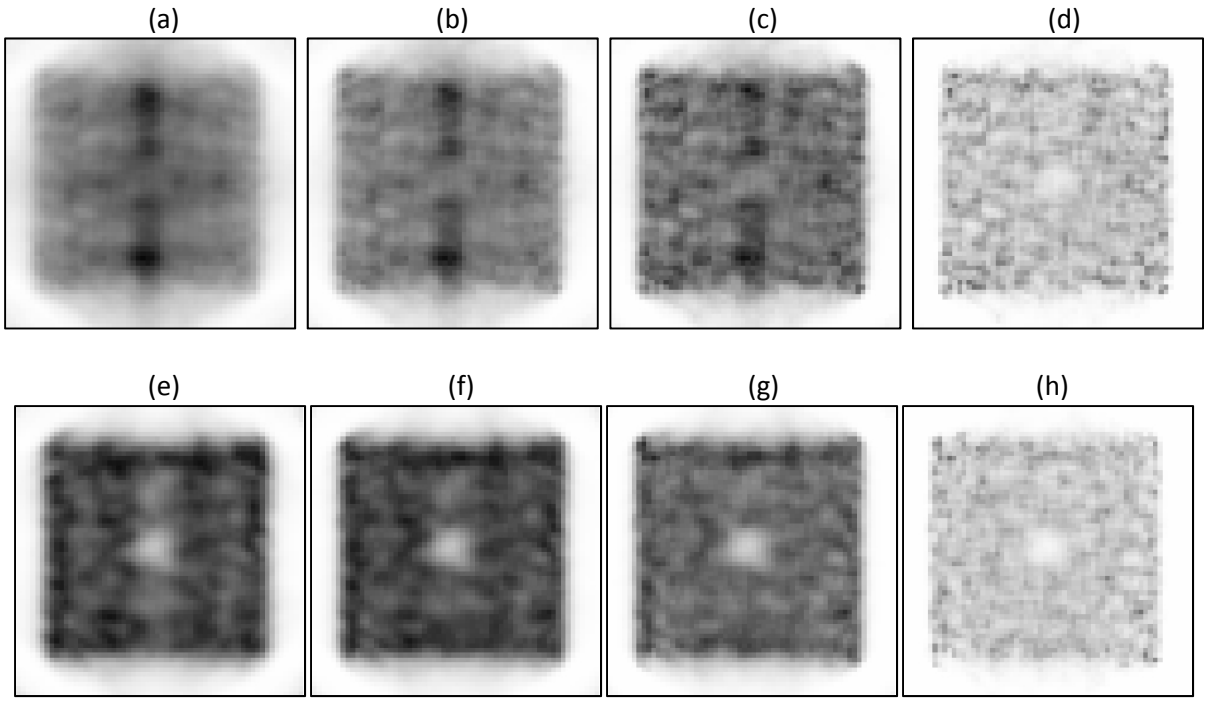

Figure 70: Reconstructions of the Cool Sphere phantom with the p7 collimator comparing different update stopping points: Ge Only noisy reconstructions at 20 updates (a), the chosen stopping point of 36 updates (b), 60 updates (c) and 200 updates (d), and the Si + Ge reconstructions of the Si Only phase 1 result at 28 updates (e), the phase 2 stopping point at 40 updates (f), 60 updates (g), and 200 updates (h).

The practical benefit to moving from a single-pinhole collimator to a multi-pinhole collimator allows for an increase in sensitivity. Adding a Si detector that counts the low-energy photons will also increase the system's sensitivity. This additional sensitivity allows for either a decrease in the total imaging time, or it can allow for less radiotracer to be injected and subsequently reducing the subject's radiation dose.

CHAPTER VI

CONCLUSIONS AND FUTURE WORK

An HPGe detector was characterized to determine its potential for use in small-animal imaging. The energy resolution was determined to be 0.92% at 140 keV, and the improvement over the industry standard NaI(Tl) gamma camera was clearly shown in a multi-isotope flood scan. The spatial resolution was estimated to be < 1.5 mm, and the system has an intrinsic efficiency of 55.4% at 122 keV. The HPGe system also provides an estimation of the depth of interaction in 1 mm bins. The demonstrated proof-of-concept image reconstructions in section IV.5 show reasonable system spatial resolution, between 1.7 and 1.35 mm, while the uniformity needs to be improved upon. The following discussion focuses on several key components of the HPGe system which could likely be modified to improve SPECT image quality.

Currently the intrinsic spatial resolution of the system is limited by the accuracy of the sub-strip positioning algorithm. Future work will investigate methods to improve this accuracy. One way to try to improve upon this method will be to look at the response of a small point source as it is moved across a strip, as opposed to the current flood-acquisition method. This method may allow for better estimation of event positions as the interaction site approaches the pixel gaps. Another method for improving the sub-strip position estimation would involve modeling the position-dependent response of different interaction types within the detector bulk in order to create a library of interactions and the modeled output signal. This could be used in conjunction with maximum-likelihood estimation to estimate interaction position. Further work could also include pulse-shape analysis as opposed to only using the signal seen at the peak rise time (fast energy) and summed signal output (slow energy) currently used.

One area of investigation that could lead to improvement in image quality is incorporation of depth of interaction information. In the reconstructions presented in section IV.5 all projections were summed into a single depth before being reconstructed, as the analytical system matrix used does not include depth. As discussed in section II.5.2, using the depth information has the potential to increase spatial resolution by reducing parallax error. The analytical

derivation of the system matrix can be altered to include additional depth estimations, but would require some additional calibrations in order to ensure that the focal length determined from the system characterization is the distance from the pinhole origin to the surface of the detector, and not to the average interaction depth as is currently determined. One confounding factor to using the DOI information is that using individual depth positions would significantly increase the noise in the reconstruction, as the number of counts in one projection pixel would be divided over the 10 depth bins. We plan to investigate this tradeoff by reconstructing a hot rod phantom acquisition with 1 depth bin, 2 depth bins, 5 depth bins, and 10 depth bins in order to determine the amount of resolution improvement when different depth bins are utilized. Another potential downside to the inclusion of DOI information is that system matrix size will increase by a factor of the number of depths, leading to slower reconstruction times.

As discussed in detail in section IV.6, there is still a significant amount of investigation required into how to correct for the image artifacts due to event losses from interactions in the gap region between strips. The same methods to improve sub-strip position estimation could also be applied to improve gap-event estimation, especially the signal modeling and the single-pixel illumination via a point source. Both of these methods would help to gain additional understanding of the physics of interactions in the gaps, which would help to recover these events. Interactions that occur both directly below and adjacent to gap regions can cause charge to be collected on two strips (charge-sharing). To accurately model the position of these charge-sharing events, knowledge of how far away from gaps charge-sharing events can occur is required, and could possibly be determined by the single-pixel illumination method. Altering the signal processing, either at the pulse-shape processing level or at the 'semi-raw' level described in section IV.6.2, may help to better estimate the number of interactions that occur in the gaps, and subsequently help to correct for the gap artifacts seen in reconstructed images.

Another area of potential improvement to the system is to implement a method to relate reconstructed image intensity to activity in the object. This can be done using a calibration factor that is dependent on the isotope being used and the collimator, as both affect system sensitivity. Some reconstructions also incorporate scatter correction (Hutton, Buvat et al. 2011) and attenuation correction (Hwang and Hasegawa 2005) into the reconstruction to improve the

quantitative accuracy. As discussed in section II.5.1, the amount of scatter accepted in the system's energy window is dependent on the size of the energy window and the energy resolution of the system. The high energy resolution of the HPGe system may not require scatter corrections as it has the ability to reject more scattered counts using its narrow energy windows. It will be beneficial in the future to determine whether scatter correction is required for quantitative accuracy.

The effect of attenuation must also be determined in conjunction with scatter correction results. It has been shown in simulations that, for a mouse-sized cylindrical phantom with a ^{99m}Tc point source located in the center, scatter causes a 6.1% increase in the counts in a ROI of the reconstructed object, while attenuation causes an 18.5% decrease for a standard NaI(Tl) detector with a 20% energy window (Chen, Wang et al. 2009). These two effects directly combine to determine the difference between activity concentration and the estimated activity concentration in an image. In the case of no scatter or attenuation corrections, images from NaI(Tl) detectors will include both scatter and attenuation while images from HPGe detectors will likely only include very small amounts of scatter but the same amount of attenuation. When these effects are combined, images based on NaI(Tl) detector projections will have estimated activity concentrations closer to the actual activity concentration than those based on HPGe projections. For accurate quantification to be possible with HPGe systems, both of these correction types must be investigated.

Finally, the next stage of this project will involve the Ge detector being reconfigured into a stacked geometry with the Si, as discussed in detail in Chapter V. This stacked system will allow for multi-pinhole collimators with highly multiplexing Ge projections to be used with little multiplexing on Si projections that will improve image quality over reconstructions with only the highly multiplexed Ge projections alone. These simulation results will be validated by phantom studies in an actual system as the future work of other students in the lab. One potential benefit to the stacked-system design is that this configuration may also help to reduce the gap artifacts seen in section IV.5. The Si projections will not have gap artifacts like the Ge projections, and combining the two could help to mitigate the gap artifacts if the above methods do not adequately solve the gap estimation problem.

This projection has demonstrated that HPGe detectors have the potential to be used as part of a practical small-animal SPECT system.

REFERENCES

Accorsi, R. and Metzler, S. D. (2004) Analytic determination of the resolution-equivalent effective diameter of a pinhole collimator. *Medical Imaging, IEEE Transactions on*, **23**, 750-763.

Agostinelli, S., Allison, J., Amako, K., Apostolakis, J., Araujo, H., Arce, P., Asai, M., Axen, D., Banerjee, S., Barrand, G., et al. (2003) Geant4—a simulation toolkit. *Nuclear Instruments and Methods in Physics Research Section A: Accelerators, Spectrometers, Detectors and Associated Equipment*, **506**, 250-303.

Alptekin, K., Degirmenci, B., Kivircik, B., Durak, H., Yemez, B., Derebek, E. and Tunca, Z. (2001) Tc-99m HMPAO brain perfusion SPECT in drug-free obsessive-compulsive patients without depression. *Psychiatry Research: Neuroimaging*, **107**, 51-56.

Anger, H. O. (1958) Scintillation Camera. *Review of Scientific Instruments*, **29**, 27-33.

Barber, B. H. and Woolfenden, J. M. (1996). Semiconductor Detectors in Nuclear Medicine: Progress and Prospects. Nuclear Medicine. Henkin, R. St. Louis, Mosby-Year Book, Inc.**:** 168 - 184.

Barrett, H. H., Eskin, J. D. and Barber, H. B. (1995) Charge Transport in Arrays of Semiconductor Gamma-Ray Detectors. *Physical Review Letters*, **75**, 156-159.

Barrett, H. H., Hunter, W. C. J., Miller, B. W., Moore, S. K., Yichun, C. and Furenlid, L. R. (2009) Maximum-Likelihood Methods for Processing Signals From Gamma-Ray Detectors. *Nuclear Science, IEEE Transactions on*, **56**, 725-735.

Beekman, F. J., van der Have, F., Vastenhouw, B., van der Linden, A. J., van Rijk, P. P., Burbach, J. P. and Smidt, M. P. (2005) U-SPECT-I: a novel system for submillimeter-resolution tomography with radiolabeled molecules in mice. *Journal of nuclear medicine : official publication, Society of Nuclear Medicine*, **46**, 1194-1200.

Bellm, E. C., Boggs, S. E., Bandstra, M. S., Bowen, J. D., Perez-Becker, D., Wunderer, C. B., Zoglauer, A., Amman, M., Luke, P. N., Hsiang-Kuang, C., et al. (2009) Overview of the Nuclear Compton Telescope. *Nuclear Science, IEEE Transactions on*, **56**, 1250-1256.

Beque, D., Nuyts, J., Bormans, G., Suetens, P. and Dupont, P. (2003) Characterization of pinhole SPECT acquisition geometry. *Medical Imaging, IEEE Transactions on*, **22**, 599-612.

Beque, D., Nuyts, J., Suetens, P. and Bormans, G. (2005) Optimization of geometrical calibration in pinhole SPECT. *Medical Imaging, IEEE Transactions on*, **24**, 180-190.

Blair, J., Beckedahl, D., Kammeraad, J. and Schmid, G. (1999) Spatial resolution attainable in germanium detectors by pulse shape analysis. *Nuclear Instruments and Methods in Physics Research Section A: Accelerators, Spectrometers, Detectors and Associated Equipment*, **422**, 331-336.

Bruyant, P. P. (2002) Analytic and Iterative Reconstruction Algorithms in SPECT. *Journal of Nuclear Medicine*, **43**, 1343-1358.

Burks, M., Jordan, E., Hull, E., Mihailescu, L. and Vetter, K. (2004) Signal interpolation in germanium detectors for improved 3-D position resolution. *IEEE Symposium Conference Record Nuclear Science 2004.*1114-1118.

Bybel, B., Brunken, R. C., DiFilippo, F. P., Neumann, D. R., Wu, G. and Cerqueira, M. D. (2008) SPECT/CT imaging: clinical utility of an emerging technology. *Radiographics : a review publication of the Radiological Society of North America, Inc*, **28**, 1097-1113.

Cao, Z., Bal, G., Accorsi, R. and Acton, P. D. (2005) Optimal number of pinholes in multi-pinhole SPECT for mouse brain imaging—a simulation study. *Physics in medicine and biology*, **50**, 4609.

Chen, C.-L., Wang, Y., Lee, J. and Tsui, B. (2009) Toward Quantitative Small Animal Pinhole SPECT: Assessment of Quantitation Accuracy Prior to Image Compensations. *Molecular Imaging and Biology*, **11**, 195-203.

Chen, Y.-C. (2006). System calibration and image reconstruction for a new small-animal SPECT system. Ph. D., University of Arizona.

Chiewitz, O. and Hevesy, G. (1935) Radioactive indicators in the study of phosphorus metabolism in rats. *Nature*, **136**, 754.

Choong, W. S., Moses, W. W., Tindall, C. S. and Luke, P. N. (2005) Design for a high-resolution small-animal SPECT system using pixellated Si(Li) detectors for in vivo ¹²⁵I imaging. *Nuclear Science, IEEE Transactions on*, **52**, 174-180.

Collins, D. A., Hogenkamp, H. P. C. and Gebhard, M. W. (1999) Tumor Imaging Via Indium 111–Labeled DTPA–Adenosylcobalamin. *Mayo Clinic Proceedings*, **74**, 687-691.

Cooper, R. J., Boston, A. J., Boston, H. C., Cresswell, J. R., Grint, A. N., Harkness, L. J., Nolan, P. J., Oxley, D. C., Scraggs, D. P., Mather, A. R., Lazarus, I. and Simpson, J. (2009) Positron Emission Tomography imaging with the SmartPET system. *Nuclear Instruments and Methods in Physics Research Section A: Accelerators, Spectrometers, Detectors and Associated Equipment*, **606**, 523-532.

Cooper, R. J., Boston, A. J., Boston, H. C., Cresswell, J. R., Grint, A. N., Mather, A. R., Nolan, P. J., Scraggs, D. P., Turk, G., Hall, C. J., et al. (2007) SmartPET: Applying HPGe and pulse shape analysis to small-animal PET. *Nuclear Instruments and Methods in Physics Research Section A: Accelerators, Spectrometers, Detectors and Associated Equipment*, **579**, 313-317.

Cowey, S., Szafran, A. A., Kappes, J., Zinn, K. R., Siegal, G. P., Desmond, R. A., Kim, H., Evans, L. and Hardy, R. W. (2007) Breast cancer metastasis to bone: evaluation of bioluminescent imaging and microSPECT/CT for detecting bone metastasis in immunodeficient mice. *Clinical & experimental metastasis*, **24**, 389-401.

Deconinck, F. (2003) Nuclear imaging in the realm of medical imaging. *Nuclear Instruments and Methods in Physics Research Section A: Accelerators, Spectrometers, Detectors and Associated Equipment*, **509**, 213-228.

Dobrucki, L. W. and Sinusas, A. J. (2010) PET and SPECT in cardiovascular molecular imaging. *Nat Rev Cardiol*, **7**, 38-47.

Dokhale, P. A., Silverman, R. W., Shah, K. S., Farrell, R., McClish, M. A., Entine, G. and Cherry, S. R. (2006) Intrinsic Spatial Resolution and Parallax Correction Using Depth-Encoding PET Detector Modules Based on Position-Sensitive APD Readout. *Nuclear Science, IEEE Transactions on*, **53**, 2666-2670.

Durko, H. L., Barrett, H. H. and Furenlid, L. R. (2012). High-resolution anamorphic SPECT imaging. Nuclear Science Symposium and Medical Imaging Conference (NSS/MIC), 2012 IEEE.

Ficaro, E. P., Fessler, J. A., Shreve, P. D., Kritzman, J. N., Rose, P. A. and Corbett, J. R. (1996) Simultaneous transmission/emission myocardial perfusion tomography. Diagnostic accuracy of attenuation-corrected 99mTc-sestamibi single-photon emission computed tomography. *Circulation*, **93**, 463-473.

Forrer, F., Valkema, R., Bernard, B., Schramm, N., Hoppin, J., Rolleman, E., Krenning, E. and de Jong, M. (2006) In vivo radionuclide uptake quantification using a multi-pinhole SPECT system to predict renal function in small animals. *European journal of nuclear medicine and molecular imaging*, **33**, 1214-1217.

Forster, R. A., Cox, L. J., Barrett, R. F., Booth, T. E., Briesmeister, J. F., Brown, F. B., Bull, J. S., Geisler, G. C., Goorley, J. T., Mosteller, R. D., Post, S. E., Prael, R. E., Selcow, E. C. and Sood, A. (2004) MCNP™ Version 5. *Nuclear Instruments and Methods in Physics Research Section B: Beam Interactions with Materials and Atoms*, **213**, 82-86.

Franc, B. L., Acton, P. D., Mari, C. and Hasegawa, B. H. (2008) Small-Animal SPECT and SPECT/CT: Important Tools for Preclinical Investigation. *Journal of Nuclear Medicine*, **49**, 1651-1663.

Furenlid, L. R., Wilson, D. W., Yi-chun, C., Hyunki, K., Pietraski, P. J., Crawford, M. J. and Barrett, H. H. (2004) FastSPECT II: a second-generation high-resolution dynamic SPECT imager. *Nuclear Science, IEEE Transactions on*, **51**, 631-635.

Goertzen, A. L., Bao, Q., Bergeron, M., Blankemeyer, E., Blinder, S., Cañadas, M., Chatziioannou, A. F., Dinelle, K., Elhami, E., Jans, H.-S., et al. (2012) NEMA NU 4-2008 Comparison of Preclinical PET Imaging Systems. *Journal of Nuclear Medicine*, **53**, 1300-1309.

Gros, S., Hammond, N. J., Lister, C. J., Chowdhury, P., Fischer, S. M. and Freeman, S. J. (2009) Performance tests of large area position-sensitive planar germanium detectors with conventional and amorphous contacts. *Nuclear Instruments and Methods in Physics Research Section A: Accelerators, Spectrometers, Detectors and Associated Equipment*, **602**, 467-476.

Gullberg, G. T., Zeng, G. L., Datz, F. L., Christian, P. E., Tung, C.-H. and Morgan, H. T. (1992) Review of convergent beam tomography in single photon emission computed tomography. *Physics in medicine and biology*, **37**, 507.

Hachamovitch, R., Berman, D. S., Shaw, L. J., Kiat, H., Cohen, I., Cabico, J. A., Friedman, J. and Diamond, G. A. (1998) Incremental prognostic value of myocardial perfusion single photon emission computed tomography for the prediction of cardiac death: differential stratification for risk of cardiac death and myocardial infarction. *Circulation*, **97**, 535-543.

Harkness, L. J., Boston, A. J., Boston, H. C., Cooper, R. J., Cresswell, J. R., Grint, A. N., Nolan, P. J., Oxley, D. C., Scraggs, D. P., Beveridge, T., Gillam, J. and Lazarus, I. (2009) Optimisation of a dual head semiconductor Compton camera using Geant4. *Nuclear Instruments and Methods in Physics Research Section A: Accelerators, Spectrometers, Detectors and Associated Equipment*, **604**, 351-354.

Harteveld, A. A., Meeuwis, A. P., Disselhorst, J. A., Slump, C. H., Oyen, W. J., Boerman, O. C. and Visser, E. P. (2011) Using the NEMA NU 4 PET image quality phantom in multipinhole small-animal SPECT. *Journal of nuclear medicine : official publication, Society of Nuclear Medicine*, **52**, 1646-1653.

Hasegawa, B. H., Stebler, B., Rutt, B. K., Martinez, A., Gingold, E. L., Barker, C. S., Faulkner, K. G., Cann, C. E. and Boyd, D. P. (1991) A prototype high-purity germanium detector system with fast photon-counting circuitry for medical imaging. *Med Phys*, **18**, 900-909.

Hayward, J. and Wehe, D. (2008) Charge Loss Correction in a High-Purity Germanium Double-Sided Strip Detector. *IEEE Transactions on Nuclear Science*, **55**, 2789-2797.

Hayward, J. and Wehe, D. (2008) Incomplete charge collection in an HPGe double-sided strip detector. *Nuclear Instruments and Methods in Physics Research Section A: Accelerators, Spectrometers, Detectors and Associated Equipment*, **586**, 215-223.

Hesterman, J. Y., Kupinski, M. A., Clarkson, E. and Barrett, H. H. (2007) Hardware assessment using the multi-module, multi-resolution system (M[sup 3]R): A signal-detection study. *Medical physics*, **34**, 3034-3044.

Hesterman, J. Y., Kupinski, M. A., Clarkson, E., Wilson, D. W. and Barrett, H. H. (2007) Evaluation of hardware in a small-animal SPECT system using reconstructed images. *Proceedings of SPIE*, **65151G**, 65151G.

Hesterman, J. Y., Kupinski, M. A., Furenlid, L. R., Wilson, D. W. and Barrett, H. H. (2007) The multi-module, multi-resolution system (M3R): a novel small-animal SPECT system. *Medical physics*, **34**, 987-993.

Hofstadter, R. (1948) Alkali Halide Scintillation Counters. *Physical Review*, **74**, 100-101.

Horn, B. K. P., Hilden, H. M. and Negahdaripour, S. (1988) Closed-form solution of absolute orientation using orthonormal matrices. *Journal of the Optical Society of America A*, **5**, 1127-1135.

Hruska, C. B. and O'Connor, M. K. (2008) A Monte Carlo Model for Energy Spectra Analysis in Dedicated Nuclear Breast Imaging. *Nuclear Science, IEEE Transactions on*, **55**, 491-500.

Hubbell, J. H. and Seltzer, S. M. (2004). Tables of X-Ray Mass Attenuation Coefficients and Mass Energy-Absorption Coefficients (version 1.4). Gaithersburg, MD, National Institute of Standards and Technology. http://physics.nist.gov/xaamdi.

Hudson, H. M. and Larkin, R. S. (1994) Accelerated image reconstruction using ordered subsets of projection data. *Medical Imaging, IEEE Transactions on*, **13**, 601-609.

Hutton, B. F., Buvat, I. and Beekman, F. (2011) Review and current status of SPECT scatter correction. *Physics in medicine and biology*, **56**, R85.

Hwang, A. B., Franc, B. L., Gullberg, G. T. and Hasegawa, B. H. (2008) Assessment of the sources of error affecting the quantitative accuracy of SPECT imaging in small animals. *Physics in medicine and biology*, **53**, 2233.

Hwang, A. B. and Hasegawa, B. H. (2005) Attenuation correction for small animal SPECT imaging using x-ray CT data. *Medical physics*, **32**, 2799-2804.

Hwang, A. B., Iwata, K. and Hasegawa, B. H. (2001). Simulation of depth of interaction effects for pinhole SPECT. Nuclear Science Symposium Conference Record, 2001 IEEE.

Jan, S., Santin, G., Strul, D., Staelens, S., Assié, K., Autret, D., Avner, S., Barbier, R., Bardiès, M., Bloomfield, P. M., et al. (2004) GATE: a simulation toolkit for PET and SPECT. *Physics in medicine and biology*, **49**, 4543.

Jaszczak, R. J., Li, J., Wang, H., Zalutsky, M. R. and Coleman, R. E. (1994) Pinhole collimation for ultra-high-resolution, small-field-of-view SPECT. *Physics in medicine and biology*, **39**, 425.

Johnson, L. C., Campbell, D. L., Hull, E. L. and Peterson, T. E. (2011) Characterization of a high-purity germanium detector for small-animal SPECT. *Phys Med Biol*, **56**, 5877-5888.

Kacperski, K., Erlandsson, K., Ben-Haim, S. and Hutton, B. F. (2011) Iterative deconvolution of simultaneous 99m Tc and 201 Tl projection data measured on a CdZnTe-based cardiac SPECT scanner. *Physics in medicine and biology*, **56**, 1397.

Kaufman, L. (1987) Implementing and Accelerating the EM Algorithm for Positron Emission Tomography. *Medical Imaging, IEEE Transactions on*, **6**, 37-51.

Kim, H., Furenlid, L. R., Crawford, M. J., Wilson, D. W., Barber, H. B., Peterson, T. E., Hunter, W. C., Liu, Z., Woolfenden, J. M. and Barrett, H. H. (2006) SemiSPECT: a small-animal single-photon emission computed tomography (SPECT) imager based on eight cadmium zinc telluride (CZT) detector arrays. *Medical physics*, **33**, 465-474.

Kim, H., Furenlid, L. R., Crawford, M. J., Wilson, D. W., Barber, H. B., Peterson, T. E., Hunter, W. C. J., Liu, Z., Woolfenden, J. M. and Barrett, H. H. (2006) SemiSPECT: A small-animal single-photon emission computed tomography (SPECT) imager based on eight cadmium zinc telluride (CZT) detector arrays. *Medical physics*, **33**, 465-474.

Knoll, G. F. (2000). Radiation Detection and Measurement. Hoboken, John Wiley & Sons, Inc.

Kuhn, A., Surti, S., Karp, J. S., Muehllehner, G., Newcomer, F. M. and VanBerg, R. (2006) Performance assessment of pixelated LaBr₃ detector modules for time-of-flight PET. *Nuclear Science, IEEE Transactions on*, **53**, 1090-1095.

Kuikka, J. T., Tenhunen-Eskelinen, M., Jurvelin, J. and Kiiliänen, H. (1993) Physical performance of the Siemens MultiSPECT 3 gamma camera. *Nuclear medicine communications*, **14**, 490-497.

Kupinski, M. A. and Barrett, H. H. (2005). Small-animal SPECT imaging, Springer.

Kurfess, J. D., Johnson, W. N., Kroeger, R. A. and Phlips, B. F. (2000) Considerations for the next Compton telescope mission. *AIP Conference Proceedings*, **510**, 789-793.

Lamusuo, S., Ruottinen, H. M., Knuuti, J., Härkönen, R., Ruotsalainen, U., Bergman, J., Haaparanta, M., Solin, O., Mervaala, E., Nousiainen, U., et al. (1997) Comparison of[18F]FDG-PET, [99mTc]-HMPAO-SPECT, and [123I]-iomazenil-SPECT in localising the epileptogenic cortex. *Journal of Neurology, Neurosurgery & Psychiatry*, **63**, 743-748.

Lange, K. and Carson, R. (1984) EM reconstruction algorithms for emission and transmission tomography. *Journal of computer assisted tomography*, **8**, 306-316.

Lavalaye, J., Linszen, D. H., Booij, J., Dingemans, P. M. A. J., Reneman, L., Habraken, J. B. A., Gersons, B. P. R. and van Royen, E. A. (2001) Dopamine transporter density in young patients with schizophrenia assessed with [123]FP-CIT SPECT. *Schizophrenia Research*, **47**, 59-67.

LeFree, M. T., Vogel, R. A., Kirch, D. L. and Steele, P. P. (1981) Seven-pinhole tomography--a technical description. *Journal of nuclear medicine : official publication, Society of Nuclear Medicine*, **22**, 48-54.

Levin, C. (2005) Primer on molecular imaging technology. *European journal of nuclear medicine and molecular imaging*, **32**, S325-S345.

Lin, Z., Vunckx, K. and Nuyts, J. (2011) Multi-Pinhole SPECT Calibration: Influence of Data Noise and Systematic Orbit Deviations. *Medical Imaging, IEEE Transactions on*, **30**, 1795-1807.

Magota, K., Kubo, N., Kuge, Y., Nishijima, K.-i., Zhao, S. and Tamaki, N. (2011) Performance characterization of the Inveon preclinical small-animal PET/SPECT/CT system for multimodality imaging. *European journal of nuclear medicine and molecular imaging*, **38**, 742-752.

Mahmood, S., Erlandsson, K., Cullum, I. and Hutton, B. (2011) Experimental results from a prototype slit-slat collimator with mixed multiplexed and non-multiplexed data. *Physics in medicine and biology*, **56**, 4311.

Mahmood, S. T., Erlandsson, K., Cullum, I. and Hutton, B. F. (2010) The potential for mixed multiplexed and non-multiplexed data to improve the reconstruction quality of a multi-slit–slat collimator SPECT system. *Physics in medicine and biology*, **55**, 2247.

Mankoff, D. A. (2007) A Definition of Molecular Imaging. *Journal of Nuclear Medicine*, **48**, 18N-21N.

McBiles, M., Lambert, A. T., Cote, M. G. and Kim, S. Y. (1995) Sestamibi parathyroid imaging. *Seminars in nuclear medicine*, **25**, 221-234.

McCready, V. R., Parker, R. P., Gunnersen, E. M., Ellis, R., Moss, E., Gore, W. G. and Bell, J. (1971) Clinical tests on a prototype semiconductor gamma-camera. *Br J Radiol*, **44**, 58-62.

McDonald, B. S. (2010). Development of the SiliSPECT Small-Animal Imager. Ph. D., Vanderbilt University.

McDonald, B. S., Shokouhi, S., Barrett, H. H. and Peterson, T. E. (2007) Multi-energy, single-isotope imaging using stacked detectors. *Nuclear Instruments and Methods in Physics Research Section A: Accelerators, Spectrometers, Detectors and Associated Equipment*, **579**, 196-199.

Meikle, S. R., Fulton, R. R., Eberl, S., Dahlbom, M., Koon-Pong, W. and Fulham, M. J. (2001) An investigation of coded aperture imaging for small animal SPECT. *Nuclear Science, IEEE Transactions on*, **48**, 816-821.

Meikle, S. R., Kench, P., Kassiou, M. and Banati, R. B. (2005) Small animal SPECT and its place in the matrix of molecular imaging technologies. *Physics in medicine and biology*, **50**, R45.

Meikle, S. R., Kench, P., Weisenberger, A. G., Wojcik, R., Smith, M. F., Majewski, S., Eberl, S., Fulton, R. R., Rosenfeld, A. B. and Fulham, M. J. (2001). A prototype coded aperture detector for small animal SPECT. Nuclear Science Symposium Conference Record, 2001 IEEE.

Metzler, S. D., Bowsher, J. E., Greer, K. L. and Jaszczak, R. J. (2002) Analytic determination of the pinhole collimator's point-spread function and RMS resolution with penetration. *Medical Imaging, IEEE Transactions on*, **21**, 878-887.

Metzler, S. D., Greer, K. L. and Jaszczak, R. J. (2003) Helical pinhole SPECT for small-animal imaging: a method for addressing sampling completeness. *Nuclear Science, IEEE Transactions on*, **50**, 1575-1583.

Metzler, S. D., Jaszczak, R. J., Greer, K. L. and Bowsher, J. E. (2007) Angular-Dependent Axial-Shift Correction for Pinhole SPECT. *Nuclear Science, IEEE Transactions on*, **54**, 124-129.

Metzler, S. D., Jaszczak, R. J., Patil, N. H., Vemulapalli, S., Akabani, G. and Chin, B. B. (2005) Molecular imaging of small animals with a triple-head SPECT system using pinhole collimation. *Medical Imaging, IEEE Transactions on*, **24**, 853-862.

Miller, B., Barrett, H., Barber, H. and Wilson, D. (2007) Gamma-ray microscopy using micro-coded apertures and Bazooka SPECT, a low-cost, high-resolution image intensifying gamma camera. *J NUCL MED MEETING ABSTRACTS*, **48**, 47P-a-.

Miyaoka, R. S., Lewellen, T. K., Yu, H. and McDaniel, D. L. (1998) Design of a depth of interaction (DOI) PET detector module. *Nuclear Science, IEEE Transactions on*, **45**, 1069-1073.

Mok, G. S. P., Tsui, B. M. W. and Beekman, F. J. (2011) The effects of object activity distribution on multiplexing multi-pinhole SPECT. *Physics in medicine and biology*, **56**, 2635.

Mok, G. S. P., Yuchuan, W. and Tsui, B. (2009) Quantification of the Multiplexing Effects in Multi-Pinhole Small Animal SPECT: A Simulation Study. *Nuclear Science, IEEE Transactions on*, **56**, 2636-2643.

Mueller, B., O'Connor, M. K., Blevis, I., Rhodes, D. J., Smith, R., Collins, D. A. and Phillips, S. W. (2003) Evaluation of a Small Cadmium Zinc Telluride Detector for Scintimammography. *J Nucl Med*, **44**, 602-609.

NEMA (2007). Performance Measurements of Gamma Cameras. Rosslyn VA, NEMA.

NEMA (2008). Performance Measurements for Small Animal Positron Emission Tomographs; NEMA Standards Publication NU 4-2008. NEMA Standards Publication NU 4-2008.

Noo, F., Clackdoyle, R., Mennessier, C., White, T. A. and Roney, T. J. (2000) Analytic method based on identification of ellipse parameters for scanner calibration in cone-beam tomography. *Physics in medicine and biology*, **45**, 3489.

Nuyts, J., Vunckx, K., Defrise, M. and Vanhove, C. (2009) Small animal imaging with multi-pinhole SPECT. *Methods*, **48**, 83-91.

Ogawa, K., Ohmura, N., Iida, H., Nakamura, K., Nakahara, T. and Kubo, A. (2009) Development of an ultra-high resolution SPECT system with a CdTe semiconductor detector. *Annals of nuclear medicine*, **23**, 763-770.

Parnham, K. B., Chowdhury, S., Li, J., Wagenaar, D. J. and Patt, B. E. (2006). Second-Generation, Tri-Modality Pre-Clinical Imaging System. Nuclear Science Symposium Conference Record, 2006. IEEE.

Perez-Andujar, A. and Pibida, L. (2004) Performance of CdTe, HPGe and NaI(Tl) detectors for radioactivity measurements. *Applied Radiation and Isotopes*, **60**, 41-47.

Peterson, T. E. and Furenlid, L. R. (2011) SPECT detectors: the Anger Camera and beyond. *Physics in medicine and biology*, **56**, R145.

Phlips, B. F., Johnson, W. N., Kroeger, R. A., Kurfess, J. D., Phillips, G., Wulf, E. A. and Luke, P. N. (2002) Development of germanium strip detectors for environmental remediation. *Nuclear Science, IEEE Transactions on*, **49**, 597-600.

Qi, J. and Leahy, R. M. (2006) Iterative reconstruction techniques in emission computed tomography. *Physics in medicine and biology*, **51**, R541.

Rizo, P., Grangeat, P. and Guillemaud, R. (1994) Geometric calibration method for multiple-head cone-beam SPECT system. *Nuclear Science, IEEE Transactions on*, **41**, 2748-2757.

Roney, T. J. (1989). Coded-aperture transaxial tomography using modular gamma cameras. Ph. D, University of Arizona

Rusinek, H., Reich, T., Youdin, M., Clagnaz, M. and Kolwicz, R. (1980) An Ultrapure Germanium Detector Array for Quantitating Three-Dimensional Distribution of a Radionuclide: A Study of Phantoms. *J Nucl Med*, **21**, 777-782.

Schramm, N. U., Ebel, G., Engeland, U., Schurrat, T., Behe, M. and Behr, T. M. (2003) High-resolution SPECT using multipinhole collimation. *Nuclear Science, IEEE Transactions on*, **50**, 315-320.

Shepp, L. A. and Vardi, Y. (1982) Maximum Likelihood Reconstruction for Emission Tomography. *Medical Imaging, IEEE Transactions on*, **1**, 113-122.

Shokouhi, S., McDonald, B. S., Durko, H. L., Fritz, M. A., Furenlid, L. R. and Peterson, T. E. (2009) Thick Silicon Double-Sided Strip Detectors for Low-Energy Small-Animal SPECT. *Nuclear Science, IEEE Transactions on*, **56**, 557-564.

Shokouhi, S., Wilson, D. W., Metzler, S. D. and Peterson, T. E. (2010) Evaluation of image reconstruction for mouse brain imaging with synthetic collimation from highly multiplexed SiliSPECT projections. *Physics in medicine and biology*, **55**, 5151.

Taillefer, R. (1999) The role of 99mTc-sestamibi and other conventional radiopharmaceuticals in breast cancer diagnosis. *Seminars in nuclear medicine*, **29**, 16-40.

Tantawy, M., Jiang, R., Wang, F., Takahashi, K., Peterson, T., Zemel, D., Hao, C.-M., Fujita, H., Harris, R., Quarles, C. and Takahashi, T. (2012) Assessment of renal function in mice with unilateral ureteral obstruction using 99mTc-MAG3 dynamic scintigraphy. *BMC Nephrology*, **13**, 168.

van der Have, F., Vastenhouw, B., Ramakers, R. M., Branderhorst, W., Krah, J. O., Ji, C., Staelens, S. G. and Beekman, F. J. (2009) U-SPECT-II: An Ultra-High-Resolution Device for Molecular Small-Animal Imaging. *Journal of nuclear medicine : official publication, Society of Nuclear Medicine*, **50**, 599-605.

Vandenberghe, S., Staelens, S., Byrne, C. L., Soares, E. J., Lemahieu, I. and Glick, S. J. (2006) Reconstruction of 2D PET data with Monte Carlo generated system matrix for generalized natural pixels. *Physics in medicine and biology*, **51**, 3105.

Vanhove, C., Andreyev, A., Defrise, M., Nuyts, J. and Bossuyt, A. (2007) Resolution recovery in pinhole SPECT based on multi-ray projections: a phantom study. *European journal of nuclear medicine and molecular imaging*, **34**, 170-180.

Vanhove, C., Defrise, M., Bossuyt, A. and Lahoutte, T. (2009) Improved quantification in single-pinhole and multiple-pinhole SPECT using micro-CT information. *European journal of nuclear medicine and molecular imaging*, **36**, 1049-1063.

Vetter, K., Burks, M. and Mihailescu, L. (2004) Gamma-ray imaging with position-sensitive HPGe detectors. *Nuclear Instruments and Methods in Physics Research Section A: Accelerators, Spectrometers, Detectors and Associated Equipment*, **525**, 322-327.

Visser, E. P., Harteveld, A. A., Meeuwis, A. P. W., Disselhorst, J. A., Beekman, F. J., Oyen, W. J. G. and Boerman, O. C. (2011) Image quality phantom and parameters for high spatial resolution small-animal SPECT. *Nuclear Instruments and Methods in Physics Research Section A: Accelerators, Spectrometers, Detectors and Associated Equipment*, **654**, 539-545.

Vogel, R. A., Kirch, D., LeFree, M. and Steele, P. (1978) A new method of multiplanar emission tomography using a seven pinhole collimator and an Anger scintillation camera. *Journal of nuclear medicine : official publication, Society of Nuclear Medicine*, **19**, 648-654.

Vunckx, K., Suetens, P. and Nuyts, J. (2008) Effect of Overlapping Projections on Reconstruction Image Quality in Multipinhole SPECT. *Medical Imaging, IEEE Transactions on*, **27**, 972-983.

Walrand, S., Jamar, F., de Jong, M. and Pauwels, S. (2005) Evaluation of Novel Whole-Body High-Resolution Rodent SPECT (Linoview) Based on Direct Acquisition of Linogram Projections. *Journal of Nuclear Medicine*, **46**, 1872-1880.

Webb, A. (2003). Introduction to Biomedical imaging. New Jersey, John wiley & Sons, Inc.

Weber, D. A., Ivanovic, M., Franceschi, D., Strand, S.-E., Erlandsson, K., Franceschi, M., Atkins, H. L., Coderre, J. A., Susskind, H., Button, T. and Ljunggren, K. (1994) Pinhole SPECT: An Approach to In Vivo High Resolution SPECT Imaging in Small Laboratory Animals. *Journal of Nuclear Medicine*, **35**, 342-348.

Weinmann, A. L., Hruska, C. B. and O'Connor, M. K. (2009) Design of optimal collimation for dedicated molecular breast imaging systems. *Medical physics*, **36**, 845-856.

Wilson, D. W., Barrett, H. H. and Clarkson, E. W. (2000) Reconstruction of two- and three-dimensional images from synthetic-collimator data. *IEEE transactions on medical imaging*, **19**, 412-422.

Wilson, D. W., Barrett, H. H. and Furenlid, L. R. (2001). A new design for a SPECT small-animal imager. Nuclear Science Symposium Conference Record, 2001 IEEE.

Wu, M. C., Hasegawa, B. H. and Dae, M. W. (2002) Performance evaluation of a pinhole SPECT system for myocardial perfusion imaging of mice. *Medical physics*, **29**, 2830-2839.

Wulf, E. A., Ampe, J., Johnson, W. N., Kroeger, R. A., Kurfess, J. D. and Phlips, B. E. (2002) Depth measurement in a germanium strip detector. *Nuclear Science, IEEE Transactions on*, **49**, 1876-1880.

Wulf, E. A., Phlips, B. F., Johnson, W. N., Kroeger, R. A., Kurfess, J. D. and Novikova, E. I. (2003) Germanium strip detector Compton telescope using three-dimensional readout. *Nuclear Science, IEEE Transactions on*, **50**, 1182-1189.

Zhiping, M. and Yi-Hwa, L. (2006) Aperture collimation correction and maximum-likelihood image reconstruction for near-field coded aperture imaging of single photon emission computerized tomography. *Medical Imaging, IEEE Transactions on*, **25**, 701-711.